

# Novel Concepts for Enhancing Nonlinear Phenomena in Optical Fibers

by

Aku Antikainen

Submitted in Partial Fulfillment of the

Requirements for the Degree

Doctor of Philosophy

Supervised by Professor Govind Agrawal

Institute of Optics

Hajim School of Engineering and Applied Sciences

University of Rochester

Rochester, New York

2018

*Dedication goes here.*

# Table of Contents

Biographical Sketch	vi
Acknowledgements	vii
Abstract	viii
Contributors and Funding Sources	ix
List of Tables	x
List of Figures	xx
<b>1 Introduction</b>	<b>1</b>
<b>2 The Nature of Light</b>	<b>8</b>
2.1 Maxwell's Equations . . . . .	12
2.2 Quantum Theory of Light . . . . .	15
<b>3 Propagation of Light</b>	<b>18</b>
3.1 Optical Fibers . . . . .	21

---

3.2	Wave Propagation in Step-Index Fiber . . . . .	22
3.3	Single-Mode Operation and Properties of the Fundamental Mode	27
3.4	Dispersion . . . . .	29
3.4.1	Chromatic Dispersion . . . . .	30
3.4.2	Intermodal Dispersion . . . . .	35
3.4.3	Polarization Mode Dispersion . . . . .	37
<b>4</b>	<b>Nonlinear Effects in Fibers</b>	<b>40</b>
4.1	Third-Harmonic Generation . . . . .	41
4.2	Kerr-Effect . . . . .	43
4.3	Self-Phase Modulation and Cross-Phase Modulation . . . . .	46
4.4	Four-Wave Mixing . . . . .	49
4.5	Stimulated Raman Scattering . . . . .	55
4.6	The Nonlinear Propagation Equation . . . . .	58
4.7	Solving the GNLSE Numerically . . . . .	61
<b>5</b>	<b>Solitons and Other Solutions of the GNLSE</b>	<b>66</b>
5.1	Solitons in Fiber Amplifiers . . . . .	74
<b>6</b>	<b>Supercontinuum Generation</b>	<b>91</b>
6.1	Overview . . . . .	91
6.2	Dual-Wavelength Pumping . . . . .	98
<b>7</b>	<b>Dual Pumping in Dispersion-Decreasing Fibers</b>	<b>119</b>
7.1	Higher-Order Dispersive Effects . . . . .	131

---

7.2 The Central Wavelength of the Frequency Comb . . . . . 143

**Bibliography** . . . . . **153**

## Biographical Sketch

The author was born in CITY, STATE. HE/SHE attended XXXX University, and graduated with a Bachelor of ARTS/SCIENCE degree in MAJOR FIELD. Describe Master's degree if from an institution other than the University of Rochester. Describe professional or career path prior to doctoral study if applicable. HE/SHE began doctoral studies in FIELD at the University of Rochester in 200X. HE/SHE was awarded [if applicable: a NAME(s) Fellowship in 200X and 200X] and [if applicable] received the Master of ARTS/SCIENCE degree from the University of Rochester. HE/SHE pursued HIS/HER research in SUBJECT under the direction of ADVISOR NAME.

The following publications were a result of work conducted during doctoral study: [list full bibliographic reference information in the format used elsewhere in the dissertation]

# Acknowledgements

Acknowledgements go here

# Abstract

abstract goes here

## Contributors and Funding Sources

This work was supported by a dissertation committee consisting of Professor Govind Agrawal and Wayne Knox of the Institute of Optics and Professor Qiang Lin of the Department of Electrical Engineering. Some related publications were published together with Dr. Francisco Arteaga Sierra. All other work conducted for the dissertation was completed by the student independently. Graduate study was supported by a Fulbright graduate study grant funded by the Technology Industries of Finland, a Fulbright renewal grant, The Väisälä Foundation graduate study grant from the Finnish Academy of Science for three years in a row, and finally funding from Corning Incorporated.

## List of Tables

## List of Figures

- 3.1 Transverse intensity profiles of some of the supported modes of a fiber. The core radius of the fiber is  $a = 2 \mu\text{m}$ , the refractive index of the core  $n_1 = 1.5$ , and the refractive index of the cladding  $n_2 = 1.45$ . The wavelength is 532 nm, which corresponds to a typical green diode pumped solid state frequency doubled laser pointer. The effective refractive indices of the modes are shown above or below their intensity profiles. . . . . 26
- 3.2 Evolution of the electric field (thick line) and the envelope (thin line) of a Gaussian pulse experiencing dispersion up to second order. The pulse envelope remains Gaussian upon propagation, but second-order dispersion causes the pulse to broaden, decrease its amplitude, and develop a chirp. . . . . 33
- 3.3 The evolution of the temporal intensity profile of an initially unchirped Gaussian pulse under the influence of third-order dispersion. The intensity profile becomes asymmetric and develops an oscillatory tail upon propagation. . . . . 34

3.4	(a) A planar waveguide and a self-consistent ray of light. (b) The copropagation of self-consistent rays leads to an intensity distribution that is constant over the length of the waveguide. (After reference [1].) . . . . .	36
4.1	The change in frequency due to SPM for a Gaussian pulse at a certain propagation distance. The frequency change is shown by the solid line and the intensity profile by the dashed line. .	47
4.2	The MI gain as a function of frequency separation from the pump frequency of 283 THz for two different peak powers. The blue curve has $\beta_2 = -8.56 \text{ ps}^2/\text{km}$ while $\beta_2 = 8.56 \text{ ps}^2/\text{km}$ for the red curve. The nonlinear coefficient is $\gamma = 0.015 \text{ (m} \cdot \text{W)}^{-1}$ and the higher-order dispersion terms are $\beta_4 = -9.29 \cdot 10^{-5} \text{ ps}^4/\text{km}$ and $\beta_6 = -9.79 \cdot 10^{-10} \text{ ps}^6/\text{km}$ for both curves. .	52
4.3	Quantum mechanical description of Raman transitions. (After ref. [2].) . . . . .	56
4.4	The normalized Raman gain profile of fused silica. The maximum gain occurs for a frequency shift of approximately 13.2 THz. . . . .	57

- 
- 5.1 The evolution of a second-order soliton with slight input noise simulated using a) the GNSLE and b) the NLSE. The NLSE predicts incorrect, seemingly periodic behavior. In reality the pulse would break into two solitons as shown in a). The solitons are labeled  $S_1$  and  $S_2$ . . . . . 71
- 5.2 Temporal evolution of an 88 fs pulse over 20 m of active fiber for (a)  $G_0 = 1$ , (b) 2, and (c) 4 dB/m. Bent trajectories show cascaded red-shifted solitons forming at different propagation distances inside the fiber amplifier. After [3]. . . . . 79
- 5.3 Spectral [(a) and (c)] and temporal [(b) and (d)] evolution under the conditions of Fig. 1 with  $G_0 = 3$  dB/m. The temporal FWHM is 88 fs in [(a) and (b)] and 880 fs in [(c) and (d)] . The ZDW of the fiber is marked by a black line, and the dashed lines show the gain band. The input soliton order is 0.7 for both cases. After [3]. . . . . 80
- 5.4 Spectral [(a) and (d)] and temporal [(c) and (f)] evolution when the fiber is active over 2.5 m (top row) and 7.5 m (bottom row). The ZDW of the fiber is marked by a black line, and the vertical dashed lines show the gain band. The soliton order  $N$  of the pulse remnants is shown in parts (b) and (e). After [3]. 83
- 5.5 Number of fundamental solitons ( $n_s$ ) at the output of a 20-m-long amplifier as a function of total gain for two input pulses of different widths launched with  $N = 0.7$ . After [3]. . . . . 85

- 
- 5.6 Spectral range (color coded) as a function of propagation distance and total gain for input pulses with (a)  $T_0 = 50$  and (b) 500 fs ( $N = 0.7$  in both cases). Different nonlinear processes responsible for spectral changes are indicated. After [3]. . . . . 88
- 6.1 Temporal and spectral evolution of a 200 fs, 1.6 kW sech-pulse in a fiber with  $\gamma = 0.015 \text{ (m} \cdot \text{W)}^{-1}$ ,  $\beta_2 = -8.56 \text{ ps}^2/\text{km}$ ,  $\beta_3 = 6.87 \cdot 10^{-2} \text{ ps}^3/\text{km}$ , and  $\beta_4 = -9.29 \cdot 10^{-5} \text{ ps}^4/\text{km}$ . The figures in the left column are on linear scale and the color axis has been cut at 500 W for clarity. The spectral evolution is color coded in a logarithmic scale. The two brightest solitons have been labeled  $S_1$  and  $S_2$  in the temporal trace. The soliton and DW parts of the spectral trace have been labeled by S and DW, respectively. . . . . 94
- 6.2 Temporal and spectral evolution of a 1 ps, 1.6 kW pulse. The left figures are on linear scale and the color axis has been cut at 5 kW for clarity. The spectral evolution is plotted using a logarithmic scale. . . . . 97
- 6.3 Group velocity dispersion  $\beta_2$  as a function of optical frequency. The circle denotes the lower frequency pump at 1060 nm. The zero-dispersion wavelength of the PCF is 1133 nm. After [4]. . 104

- 6.4 Spectral (left) and temporal (right) evolution of a dual-pump signal in the normal dispersion regime over 5 m of PCF. The spectrum scale is logarithmic over a 50-dB range. The dashed horizontal lines show the  $-50$  dB level for the spectra and the zero level for the temporal intensity plotted on a linear scale. Parameter values for the two CW pumps are  $P_0 = 200$  W,  $x = 1$ , and  $\nu_m = 350$  GHz. After [4]. . . . . 106
- 6.5 Same as figure 6.4 but for unequal pump powers such that  $x = 0.1$ . The total pump power is the same in both cases. After [4]. . . . . 108
- 6.6 Comb bandwidth (color encoded) as a function of the ratio of pump powers and propagation distance. The input parameters are  $P_0 = 200$  W and  $\nu_m = 700$  GHz. After [4]. . . . . 110
- 6.7 Comb bandwidth (color encoded) as a function of total pump power and propagation distance. The input parameters are  $x = 1$  and  $\nu_m = 700$  GHz. Spectra that did not qualify as frequency combs have been left out (lower right corner). After [4]. . . . . 113

- 
- 6.8 Evolution of a dual-pump signal over 100 m meters with (black lines) and without (red lines) including the Raman effect. Pump parameters are  $P_0 = 5$  W,  $x = 1$ , and  $\nu_m = 300$  GHz. The scale for spectra is logarithmic ranging from  $-60$  to  $0$  dB. The effect of Raman scattering is negligible in this case. After [4]. . . . . 114
- 6.9 Same as figure 6.8 but with  $P_0 = 200$  W,  $x = 1$ , and  $\nu_m = 700$  GHz. After [4]. . . . . 116
- 7.1 Dispersion parameter  $\beta_2$  at the input end of the fiber. The circle denotes  $\nu_0$ . The zero-dispersion wavelength of the PCF is 985 nm. After [5]. . . . . 122

7.2 Temporal (a) and spectral (b) evolutions of a dual-pump input inside a DDF. (a) shows the square root of the intensity on a linear scale in  $\sqrt{W}$ , and (b) shows the normalized spectral intensity in decibels. The two pumps are separated in frequency by 400 GHz and their total power is 1 W. The dashed black line shows the distance at which  $\beta_2 = 0$  at the pumps' center wavelength. Double arrows mark locations of temporal reflections in (a) together with the corresponding wavelengths in (b). The solid black line in (b) shows the theoretical prediction of the temporal reflection model discussed in the text. The dashed line shows the zero-dispersion wavelength. After [5]. . . . . 124

7.3 Temporal (a) and spectral (b) evolutions of a dual-pump input under conditions identical to those in Fig. 7.2 except that the dispersion is kept constant along the PCF length. After [5]. . . 127

7.4 Temporal (a) and spectral (b) evolutions under conditions identical to those in Fig. 7.3 except that the value of  $\beta_2$  at the pump-center wavelength was changed to  $-2.684 \text{ ps}^2/\text{km}$ . After [5]. . . . . 129

- 7.5 The temporal (middle) and spectral (bottom) evolution of a dual-pump signal over 100 meters of a DDF with  $\beta_2$  increasing from  $-10 \text{ ps}^2/\text{km}$  to  $0 \text{ ps}^2/\text{km}$ . The gray intensity scales are logarithmic. The top two traces show the duration (thick blue) and peak power (thin red) of the forming pulses as a function of distance. The vertical black dashed lines indicate the distance at which the soliton width has been reduced to three optical cycles. After [6]. . . . . 147
- 7.6 The evolution of a 800 GHz dual-pump signal in a fiber in which  $\beta_2$  grows from  $-10 \text{ ps}^2/\text{km}$  to  $5 \text{ ps}^2/\text{km}$  along its 150 m length. Third-order dispersion is  $\beta_3 = -0.03 \text{ ps}^2/\text{km}$ . After [6]. 148
- 7.7 The evolution of a 800 GHz dual-pump signal in a fiber in which  $\beta_2$  grows from  $-10 \text{ ps}^2/\text{km}$  to  $10 \text{ ps}^2/\text{km}$  along its 200 m length. Third-order dispersion is  $\beta_3 = 0.03 \text{ ps}^3/\text{km}$ . Unlike in Figs. 7.5 and 7.6, the temporal frame of reference is now with respect to the solitons, as their trajectories would look heavily curved in the pump frame of reference. After [6]. . . . . 149

- 7.8 The mean duration (FWHM, color coded) of the forming solitons after a) 80 m, b) 120 m, c) 160 m, and d) 200 m of propagation as a function of  $\beta_3$  and the final value of  $\beta_2$ . The initial value of  $\beta_2$  at the input end of 200-meter-long fiber is  $-10 \text{ ps}^2/\text{km}$ . The striped areas in the upper left corners are regions where the pulses have lost their solitonic nature by virtue of having transferred energy to the normal dispersion regime. After [6]. . . . . 150
- 7.9 Comparison of pulse trains generated with the same dual-pump input in two different fibers. Fiber A is 100 m long and its GVD increases linearly from  $-10 \text{ ps}^2/\text{km}$  to 0 over this length with  $\beta_3 = 0.05 \text{ ps}^3/\text{km}$ . Fiber B is 97 m long but its GVD increases from  $-10$  to  $-2.725 \text{ ps}^2/\text{km}$  with  $\beta_3 = -0.05 \text{ ps}^3/\text{km}$ . The total input power is 2 W and initial pump separation is 800 GHz. The two traces on the right show the pulse around  $T = 0$  showing how closely their shapes match. After [6]. . . . . 151
- 7.10 Spectra of the two pulse trains shown in Fig. 7.9 at the output of fibers A and B. After [6]. . . . . 151

- 7.11 The central wavelengths  $\lambda_{\text{soliton}}$  of the forming solitons for the parameters used in Fig. 7.8 after a) 80 m, b) 120 m, c) 160 m, and d) 200 m of propagation. The striped regions indicate that the pulses have lost their solitonic nature and have dispersed. The upper colorbar is for the top row and the lower one for the bottom row; note the different scales. After [6]. . . . . 152

## Chapter 1

# Introduction

All natural everyday optical phenomena are essentially linear. The color of the sky, rainbows, and reflections from bodies of water can all be explained in terms of linear systems where the output depends linearly on the input [7]. This means that the propagation, reflection, refraction, diffraction, and scattering of light are not dependent on the intensity of the light. The reason for this is that light in our daily lives - including sunlight - is too weak to show signs of nonlinear behavior. The optical materials themselves, glasses, air, water, metals, and even vacuum, are all inherently nonlinear [8]. The observation of optical nonlinearities requires such intense light that they could not be studied experimentally before the advent of the laser [9].

A defining characteristic of a linear time-invariant system  $H$  is that given inputs  $f(t)$  and  $g(t)$  and scalar numbers (or, in general, tensors)  $a$  and  $b$ , the output obeys  $H[af(t) + bg(t)] = aH[f(t)] + bH[g(t)]$ . In layman terms this means that scaling the input scales the output accordingly and that any summation can be performed either at the input end or at the output end. An

important consequence of this is that given a sinusoidal input to the system, the output will be a sinusoid at the same frequency as the input but with possibly different amplitude and phase. A key signature of a nonlinear system is then the generation of new frequency components. As a simple example of a system that behaves linearly for small amplitudes but nonlinearly for large ones, consider the string of a guitar. Displace the string by pulling it, release it, and it will start to oscillate around the equilibrium point making a sound. Displace by twice as much and the oscillation amplitude is now doubled. The sound is now louder but its frequency is still the same. Pull the string hard enough and it will break and make a completely different sound. The frequencies you hear are now suddenly very different.

The guitar thought experiment is an example of extreme nonlinear behavior but demonstrates how the frequency of the output will change as the behavior of the system deviates from linear. Similar things can happen with light when the light is intense enough. The response of any material to light is mostly determined by how the electrons in the material react to the external electric field. If the field is strong enough, the displacement of the electrons with respect to their nuclei will be a nonlinear function of electric field strength and new frequency components can be generated. In one of the simplest manifestations of this effect light can double its frequency. A common application of such frequency doubling is the green laser pointer where the green light is generated by frequency doubling infrared light circulating in the cavity.

Frequency doubling of light requires that a part of the response of the material to the external electric field is proportional to the square of the electric field. This naturally means that the material has to be non-centrosymmetric and only specific crystals are suitable for observing such second order optical nonlinearity also known as the Pockels effect [8]. However, most typical materials are centrosymmetric, and the lowest order optical nonlinearities are the third order effects. These include the Kerr effect where the material response depends on the third power of the electric field and the Raman effect that manifests as a delayed third order nonlinearity where the current material polarization depends on the previous values of the cube of the electric field.

The square of a sinusoid contains a term that oscillates twice as fast as the original one, which is the mathematical origin of frequency doubling. Namely, the relevant trigonometric identity is  $\sin^2(\omega t) = [1 - \cos(2\omega t)]/2$ , which also shows that a second order nonlinearity leads to the creation of a static electric field as well as the second harmonic. The cube of a sinusoid, on the other hand, contains terms oscillating at three times the original frequency, corresponding to third harmonic generation, as well as terms oscillating at the original frequency. It is the terms oscillating at the original frequency that make the third order nonlinearity arguably more interesting than that second order one, as it allows light to modify its own refractive index. This leads to rich nonlinear dynamics allowing for phenomena such as continuous spectral broadening and red shift of the whole spectrum of a

pulse.

One of the extreme manifestations of many third order nonlinear optical processes acting together is the supercontinuum, a wide spectrum generated through the nonlinear broadening of the input spectrum. The discovery of supercontinuum is credited to Alfano and Shapiro, who observed remarkable spectral broadening in bulk glass and explained their findings in terms of nonlinear optical processes in 1970 [10, 11]. It is noteworthy that Alfano and Shapiro neither focused on the spectral broadening in their studies nor coined the term supercontinuum. Similar extreme spectral broadening was also observed in rare atomic gases by the same group [12] and later in silica fibers by Lin and Stolen [13]. Since then, optical fibers of various kinds have been the main platform for supercontinuum generation due to their ability to keep light confined in a small area for long distances.

While the generation of a broad range of new frequencies through optical nonlinearities is a remarkable discovery and significant from the fundamental science point of view, broadband light sources have been around for a long time. Even the star at the heart of our Solar System provides broadband radiation, so the broad spectrum is literally nothing new under the Sun. However, no other broadband light source besides SC has the properties of very high brightness, spectral stability, and most importantly spatial and temporal coherence. Furthermore, SC are highly tunable since they can be generated in a plethora of different materials and using all kinds of lasers. Because of the unique characteristics of SC, it also has a tremendous amount

of applications. One of the first applications of supercontinuum was absorption and excitation spectroscopy, which was in turn used to study picosecond and femtosecond processes in biology, chemistry, and solid-state physics [14]. Notable examples of the processes that were studied include photosynthesis, dynamical steps of chemical reactions, and optical phonons, respectively. Supercontinuum can also be used in optical communications in pulse compression and *wavelength-division multiplexing* (WDM) [15, 16].

1996 saw the advent of the *photonic crystal fiber* (PCF) that revolutionized supercontinuum generation because it offered the possibility to tune important fiber parameters [17]. The first report on SC generation in PCF was given by Ranka et. al [18] and since then SC generation in PCF has been studied extensively [19]. The introduction of the PCF allowed for even more applications, and supercontinuum has subsequently found its way to high-precision frequency metrology [20] and ultrahigh-resolution optical coherence tomography [21], for example.

The effects of *self-phase modulation* (SPM), *four-wave mixing* (FWM) and *Stimulated Raman scattering* (SRS) were well understood at the end of the 1970's [22, 23, 24, 25, 26, 27, 28] and it was realized that the broad and flat continuum could not be explained by these phenomena alone [29]. The missing piece of the puzzle was soliton self-frequency shift (SSFS) [30]. Although solitons had been predicted in 1973 [31] and observed experimentally in 1980 [32], no satisfactory explanation for the spectral broadening was offered until the experimental observation of SSFS in 1985. SSFS plays

a crucial role in expanding the SC spectrum towards longer wavelengths, and controlling SSFS therefore offers a means to control the wavelength of solitons as well as the low frequency part of the spectra of supercontinua.

Various nonlinear effects during supercontinuum generation generally affect different parts of the forming spectrum in different ways. For example, SSFS can be solely responsible for extending the spectrum to longer wavelengths and at the same time have virtually nothing to do with its blue side. A SC spectrum therefore tends to be an amalgam of spectra belonging to various kinds of radiation such as dispersive waves and continuously red shifting solitons. The spectrum is thus generally noisy and lacks specific structure. However, under certain conditions it is possible to induce a form of order into the spectrum. When the signal is periodic in the time domain, the spectrum will be in the form of discrete, spectrally equidistant spikes. Such structured broad spectra are known as frequency combs and they have many uses.

By 1992 the dynamics of supercontinuum and frequency comb generation were understood to such an extent that an accurate mathematical model could be developed and numerical simulations be used to study them [33]. The model is known as the Generalized Nonlinear Schrödinger Equation (GNLSE) and since its introduction it has been tested thoroughly [19]. The aim of this study is to use numerical solutions to the GNLSE to find ways to enhance and control optical nonlinearities in fibers. The focus is on manipulating soliton formation, supercontinuum generation, and frequency comb generation. The means to enhance nonlinearities include designing and

---

exploring fibers with specific characteristics as well as seeding the nonlinear effects through unconventional input fields.

## Chapter 2

# The Nature of Light

Based on an idea that dates back to at least the ancient Greeks, Sir Isaac Newton eventually considered light to consist of small discrete particles he called *corpuscles* [34]. According to Newton, corpuscles traveled in straight lines with a finite velocity and corpuscles representing different colors of light had different sizes. Newton was, however, aware of the diffraction phenomenon, which had been studied and named by the Italian priest Francesco Maria Grimaldi in 1665, and in his earlier days he avoided speculations and stayed ambivalent about the nature of light. Since light passing through an aperture forms a cone, the propagation of light could not be satisfactorily explained with the corpuscular theory alone, which led Newton to incorporate elements from the wave treatment of light by concluding that light corpuscles excited vibrations in an imaginary matter, *aether* [7]. Being unable to explain the observed rectilinear propagation of light using wave theory only, Newton became a supporter of the corpuscular theory in his later days.

Because of Newton's prestige, the corpuscular theory superseded the pre-

vious idea put forward by René Descartes [35], Robert Hooke [36], and Christiaan Huygens [37], all of whom explained light via pressure or vibrations in aether without resorting to speculations about corpuscles. Although Huygens had succeeded in, for example, describing the birefringence property of an Icelandic calcite crystal using the wave treatment of light, it wasn't until the beginning 19th century that the mechanical corpuscle treatment of light was fully abandoned.

The experiment that seemed to settle the matter about the wave nature of light was Young's double slit experiment in 1801 [38]. The interference pattern observed in Young's experiment can only be explained if light is understood to be wavelike. The simplicity of the experiment and the impact of the results makes one wonder why the experiment was not conducted earlier in order to find out whether light had wavelike properties. One of the reasons why the physics community had to wait until the 19th century is that the experiment requires coherent light. Incoherent sunlight can easily be made spatially coherent by letting it pass through a small aperture, as was the case in the original experiment [7], but without knowing the requirement of coherence a priori, the necessity of the pinhole is far from obvious.

Around 1814 Augustin Jean Fresnel began a revival of the wave theory in France, unaware of Young's work and experiments. Fresnel incorporated Huygens' wave description and the interference principle to calculate various diffraction patterns arising from obstacles and apertures. Fresnel was also able to explain, using wave formalism, the rectilinear propagation of light -

an easily observed property of light that had been one of the main reasons Newton had become an adherent of the corpuscular theory. [7]

Huygens had discovered polarization during his research on optical properties of calcite crystals. At first polarization was thought to be inherent to crystalline media, but more than a century later Étienne Louis Malus discovered that polarization was also present upon reflection of light. This led Fresnel and Dominique François Arago to conduct experiments to study the effects of polarization on interference, but they were unable to explain their results. This was because at that time light waves were thought to be longitudinal like sound waves which were known to be longitudinal. After all, the interference observed in Young's experiment bore remarkable similarity to beats that are heard when two sound waves of slightly different frequencies interfere. Several years later Young was able to explain the findings by suggesting that the aethereal vibrations might be transverse with polarization being a manifestation of the direction of the vibrations. [7]

Although the first known terrestrial measurements regarding the speed of light were performed by Armand Hippolyte Louis Fizeau in 1849 [7], the question about the finiteness of the speed of light had been answered almost two centuries earlier. In the 17th century the Dane Ole Christensen Rømer observed the motion of Jupiter's nearest moon, Io, and in 1676 correctly concluded that in order to explain his observations, the speed of light must be finite. Based on Rømer's observations, Huygens and Newton individually estimated the diameter of Earth's orbit and calculated the speed of light to

be  $2.3 \cdot 10^8$  m/s and  $2.4 \cdot 10^8$  m/s, respectively [39]. Fizeau's measurements yielded the value  $3.153 \cdot 10^8$  m/s for the speed of light. Although the results differed a bit, the order of magnitude was the same astronomical  $10^8$  m/s in all of them. The speed of light might as well have been infinite, and the finiteness of it was not necessarily important until the discoveries and predictions of the Scottish physicist James Clerk Maxwell.

One of the first scientists to bring optics, circuit analysis, and studies of electricity and magnetism together was Michael Faraday. Faraday noticed that the polarization of a light beam could be altered by a strong magnetic field applied to the medium in which the beam propagated [7]. Faraday's experiments were a crucial step towards deeper understanding about the connection between optics and electromagnetism. Leveraging Faraday's discoveries and collecting other known results on electricity and magnetism as well as producing some of his own, the physicist James Clerk Maxwell arrived in a set of four famous equations that today bear his name. Using these four equations Maxwell further derived two particularly important equations: one for the electric field strength and one for the magnetic flux density. Both of the equations had the mathematical form of a wave equation. These equations had propagating solutions that correspond to propagating waves consisting of oscillating magnetic and electric fields. The equations thus allowed for some sort of electromagnetic waves that may or may not exist in real life. Should such waves exist, their velocity of propagation could trivially be seen from the equations. This velocity matched the speed of light as determined

experimentally by Fizeau, which encouraged Maxwell to conclude that light is electromagnetic radiation.

## 2.1 Maxwell's Equations

In the nineteenth century Maxwell collected and published a set of universal<sup>1</sup> equations based on electromagnetic theory and circuit analysis. These equations can be expressed using four vector equations:

$$\nabla \cdot \mathbf{D} = \rho_{\text{free}}, \quad (2.1)$$

$$\nabla \cdot \mathbf{B} = 0, \quad (2.2)$$

$$\nabla \times \mathbf{E} = -\frac{\partial \mathbf{B}}{\partial t}, \quad (2.3)$$

$$\nabla \times \mathbf{H} = \mathbf{J}_f + \frac{\partial \mathbf{D}}{\partial t}, \quad (2.4)$$

where  $\mathbf{E}$  and  $\mathbf{H}$  are the electric and magnetic field strengths, respectively, and  $\mathbf{D}$  and  $\mathbf{B}$  are the corresponding electric and magnetic flux densities,  $\rho_{\text{free}}$  is the free charge density and  $\mathbf{J}_f$  the free current density. Furthermore, the flux densities  $\mathbf{D}$  and  $\mathbf{B}$  are related to the field strengths  $\mathbf{E}$  and  $\mathbf{H}$  through

---

<sup>1</sup>Maxwell's equations fail to hold for some quantum mechanical situations such as vacuum polarization with extremely strong fields [40].

the material relations

$$\mathbf{D} = \varepsilon \mathbf{E}, \quad (2.5)$$

$$\mathbf{B} = \mu \mathbf{H}, \quad (2.6)$$

where  $\varepsilon$  is the permittivity and  $\mu$  is the permeability of the medium. These equations are also sometimes written as

$$\mathbf{D} = \varepsilon_0 \mathbf{E} + \mathbf{P}, \quad (2.7)$$

$$\mathbf{B} = \mu_0 \mathbf{H} + \mathbf{M}, \quad (2.8)$$

where  $\varepsilon_0$  is the vacuum permittivity,  $\mu_0$  is the vacuum permeability,  $\mathbf{P}$  is the induced polarization and  $\mathbf{M}$  the induced magnetization. These forms of the material equations are more general in the sense that the material responses are not necessarily assumed to be instantaneous or linear. The general form of the polarization  $\mathbf{P}$  is

$$\mathbf{P} = \mathbf{P}_L + \mathbf{P}_{NL} = \varepsilon_0 \chi^{(1)} * \mathbf{E} + \varepsilon_0 \sum_{n=2}^{\infty} \chi^{(n)} * \mathbf{E}^n, \quad (2.9)$$

where  $\mathbf{P}_L$  is the linear polarization,  $\mathbf{P}_{NL}$  is the nonlinear polarization,  $\chi^{(n)}$  is the  $n^{\text{th}}$  order susceptibility, an  $(n+1)^{\text{th}}$  order tensor, and  $*$  denotes convolution [8]. Note that with the exception of the constant  $\varepsilon_0$ , all the variables in equation 2.9 are functions of  $t$  and  $\mathbf{r}$  but the temporal and spatial dependencies have been dropped to shorten the notation. The  $n^{\text{th}}$  order convolution

$\chi^{(n)} * \mathbf{E}^n$  is a nested integral over  $n$  dummy variables such that for example the third-order polarization is

$$\varepsilon_0 \chi^{(3)} * \mathbf{E}^3 = \varepsilon_0 \iiint_{\mathbb{R}^3} \chi^{(3)}(t-t_1, t-t_2, t-t_3) \mathbf{E}(\mathbf{r}, t_1) \mathbf{E}(\mathbf{r}, t_2) \mathbf{E}(\mathbf{r}, t_3) dt_1 dt_2 dt_3. \quad (2.10)$$

Maxwell's equations are sometimes expressed in their integral form depending on the application [41]. The four Maxwell's equations can be reduced to two by using the concepts of differential form and exterior derivative and treating the electric field as a 1-form and the magnetic field as a 2-form [42]. Quaternion formalism, which was, to some degree, also used by Maxwell himself, allows one express all of the four equations with a single equation without loss of information or generality [43].

Equation 2.1, is called Gauss's law for electric fields. Since the divergence operator measures the magnitude of a vector field's sources (or sinks), equation 2.1 describes how free electric charges act as the sources of an electric field. Equation 2.2 is Gauss's law for magnetic fields and it tells that for every magnetic north pole there is a compensating south pole, which makes the divergence of the magnetic flux density vanish. No magnetic monopoles exist. Equation 2.3 is Faraday's induction law, which Faraday derived by observing that a time-varying magnetic flux passing through a closed conducting loop induces an electric current in the loop. However, since the creation of an electric field does not require a conducting loop, Faraday's law does not make any reference to one, and a changing magnetic flux density always has an asso-

ciated electric field. Equation 2.4 is the Ampère-Maxwell law that describes how time-varying electric fields and electric currents give rise to magnetic fields. Maxwell's contribution to this was the derivative term known as the displacement current, which accounts for the special cases where Ampère's law fails to hold. [7, 41]

## 2.2 Quantum Theory of Light

Around year 1900 Jules Henri Poincaré and Albert Einstein were among the prominent physicists who rejected aether. Poincaré had noticed that one could only observe relative displacements and no experiment was able to determine motion with respect to aether. Einstein did not believe that an "absolutely stationary space" was even necessary for anything and he postulated that light always propagates in empty space with a definite velocity  $c$ , which can be derived from the assumption that Maxwell's equations hold in every inertial coordinate system. This led Einstein to develop the theory of special relativity which showed that a deeper understanding of optics and the behavior of light can profoundly affect the way we look at every branch of physics. Assuming that Maxwell's equations are valid in every inertial coordinate system and concluding that mass is a form of energy was a significant paradigm shift. [7, 41]

In October 1900 Max Planck introduced the foundations of what is nowadays known as quantum mechanics, quantum physics or quantum theory [7].

Planck had developed the theory in order to avoid the so called *ultraviolet catastrophe* by making a thoroughly radical assumption that electromagnetic radiation was always emitted and absorbed in small packets, or *quanta*, of energy [44]. At that time there was little reason to make such an assumption, but accepting the quantum hypothesis allowed one to correctly predict the observed spectra of black body radiation. Einstein further proposed that not only was light emitted and absorbed in quanta, but radiation itself consisted of quanta [44]. Quantum theory became an integral part of optics, as it allowed Einstein to explain the photoelectric effect that Hertz had discovered in 1887. Further developments and reformulations in quantum theory were made in the 1920's by Sommerfeld [45], Heisenberg [46], Bohr [47], De Broglie [48], Born [49], Dirac [50], Schrödinger [51], Pauli [52], and others. By the end of the decade, quantum mechanics had become a well-verified theory [7].

Quanta of electromagnetic radiation are called *photons*, and one of the key features of quantum theory of light is that each photon has an associated energy equal to

$$E_{\text{photon}} = h_{\text{P}} f, \quad (2.11)$$

where  $f$  is the frequency of the photon and  $h_{\text{P}} \approx 6.626 \cdot 10^{-34} \text{ m}^2\text{kg/s}$  is the famous proportionality constant known as *Planck's constant*. Equation 2.11 is also one of the manifestations of *wave-particle duality* since the left hand side is the energy of a photon, which is thought of as a particle, but the right hand side tells that the energy of the particle depends on frequency, which

in turn is clearly a property of vibration, oscillation, or a wave.

Because Planck's constant is so tiny, the number of photons in most practical situations is huge. Even an ordinary 1 mW red laser pointer produces quadrillions of photons every second. Therefore, the classical electromagnetic formulation can be used to model light propagation accurately, and quantum effects, such as shot noise, can also be incorporated into the classical model.

## Chapter 3

# Propagation of Light

Every beam of electromagnetic radiation consists of a discrete number of photons and each photon has an associated frequency. According to equation 2.11, photons with different frequencies have different energies and interact differently with the atoms of the medium in which they propagate. The variations in the microscopic dynamics of interactions lead to macroscopic effects such as *chromatic dispersion* or simply dispersion, which means that the velocity of light in a medium depends on its frequency. In order to study how an arbitrary electromagnetic pulse propagates through a medium, it is necessary to know the frequency content of the pulse. It is therefore beneficial to rewrite Maxwell's equations in the frequency domain.

Consider a sourceless dielectric ( $\rho_{\text{free}} = 0$ ) and assume that there are no free currents ( $\mathbf{J}_f = \mathbf{0}$ ). Also assume, for simplicity, that the susceptibilities<sup>1</sup>  $\chi$  and  $\chi_m$  can be treated as scalars either because of isotropy or because the

---

<sup>1</sup>Susceptibilities are related to the permittivity and permeability by  $\epsilon = (1 + \chi)\epsilon_0$  and  $\mu = (1 + \chi_m)\mu_0$ .

state of polarization is maintained, which are very good approximations for a plethora of materials and purposes [7, 53]. The dielectric is also assumed to be nonmagnetic ( $\chi_m = 0$  and  $\mathbf{M} = \mathbf{0}$ ). Nonlinear optical effects typically require intensities so high that only a powerful laser is capable of producing them [8], but in order to keep the derivation more general, it will not be assumed that the material is linear. Instead,  $\chi$  is allowed to depend on field strength.

Polarization  $\mathbf{P}$  is now given by  $\mathbf{P} = \varepsilon_0\chi^{(1)} * \mathbf{E} + \mathbf{P}_{\text{NL}}$ , where  $\mathbf{P}_{\text{NL}}$  is the nonlinear part of the polarization. The material equations 2.7 and 2.8 can now be written as

$$\mathbf{D} = \varepsilon_0\mathbf{E} + \varepsilon_0\chi^{(1)} * \mathbf{E} + \mathbf{P}_{\text{NL}}, \quad (3.1)$$

$$\mathbf{B} = \mu_0\mathbf{H}, \quad (3.2)$$

for the medium in question. Now taking the curl of equation 2.3, justifiably interchanging the curl and the time derivative on the right hand side and furthermore plugging in equation 3.2 yields

$$\nabla \times \nabla \times \mathbf{E} = -\mu_0 \frac{\partial}{\partial t} (\nabla \times \mathbf{H}). \quad (3.3)$$

Now using equations 2.4 and 3.1 while keeping in mind that  $\mathbf{J}_f = \mathbf{0}$  gives

$$\nabla \times \nabla \times \mathbf{E} = -\mu_0 \varepsilon_0 \frac{\partial^2}{\partial t^2} (\mathbf{E} + \chi^{(1)} * \mathbf{E}) - \mu_0 \frac{\partial^2}{\partial t^2} \mathbf{P}_{\text{NL}} \quad (3.4)$$

$$= -\frac{1}{c^2} \frac{\partial^2}{\partial t^2} (\mathbf{E} + \chi^{(1)} * \mathbf{E}) - \mu_0 \frac{\partial^2}{\partial t^2} \mathbf{P}_{\text{NL}}. \quad (3.5)$$

By making use of the vector calculus identity  $\nabla \times \nabla \times \mathbf{E} = \nabla (\nabla \cdot \mathbf{E}) - \nabla^2 \mathbf{E}$  equation 3.5 can be written as

$$\nabla (\nabla \cdot \mathbf{E}) - \nabla^2 \mathbf{E} = -\frac{1}{c^2} \frac{\partial^2}{\partial t^2} (\mathbf{E} + \chi^{(1)} * \mathbf{E}) - \mu_0 \frac{\partial^2}{\partial t^2} \mathbf{P}_{\text{NL}}. \quad (3.6)$$

The first term of the left hand side of equation 3.6 can be shown to be zero for some cases, such as step-index fibers, and negligible in a myriad of other cases of interest, such as when  $\chi^{(1)}$  is approximately constant over one wavelength [8, 54]. By making use of this approximation that  $\nabla (\nabla \cdot \mathbf{E}) \approx \mathbf{0}$ , equation 3.6 can be written as

$$-\nabla^2 \mathbf{E} = -\frac{1}{c^2} \frac{\partial^2}{\partial t^2} (\mathbf{E} + \chi^{(1)} * \mathbf{E}) - \mu_0 \frac{\partial^2}{\partial t^2} \mathbf{P}_{\text{NL}}. \quad (3.7)$$

Taking the Fourier transform of equation 3.7 gives

$$-\nabla^2 \tilde{\mathbf{E}} = \frac{\omega^2}{c^2} (1 + \tilde{\chi}^{(1)}) \tilde{\mathbf{E}} + \mu_0 \omega^2 \tilde{\mathbf{P}}_{\text{NL}} \quad (3.8)$$

$$= \frac{\omega^2}{c^2} (1 + \tilde{\chi}^{(1)}) \tilde{\mathbf{E}} + \frac{1}{\varepsilon_0} \frac{\omega^2}{c^2} \tilde{\mathbf{P}}_{\text{NL}}. \quad (3.9)$$

$\omega^2/c^2$  is simply the vacuum wave number  $k_0$ , and  $1 + \tilde{\chi}^{(1)}$  is the square of the

frequency-dependent *refractive index*:  $1 + \tilde{\chi}^{(1)} = n^2(\omega)$ . The wave number in the medium is  $k(\omega) = n(\omega)k_0$ . Thus,

$$-\nabla^2 \tilde{\mathbf{E}} = k^2(\omega) \tilde{\mathbf{E}} + \frac{k_0^2}{\epsilon_0} \tilde{\mathbf{P}}_{\text{NL}}. \quad (3.10)$$

Regardless of the assumptions and the simplifications, equation 3.10 is very general. Losses are included in the index of refraction, and the nonlinear polarization term can account for many different effects, such as Kerr and Pockels effects and Raman scattering. Assuming that  $n(\omega)$  is piecewise constant in space and that no nonlinear effects are present, the equation simplifies to the ordinary *Helmholtz equation*:

$$\nabla^2 \tilde{\mathbf{E}} + k^2(\omega) \tilde{\mathbf{E}} = 0. \quad (3.11)$$

### 3.1 Optical Fibers

By careful adjustment of the spatial dependence of the refractive index  $n(\omega)$ , one can hope to tailor the solutions of equation 3.10, and optical fibers do just this. From a mathematical point of view, it is convenient to describe a fiber simply as a medium, the refractive index of which has a certain spatial dependence on  $x, y$  (and  $\omega$ ). Usually fibers have cylindrical symmetry such that  $n(\omega)$  is a function of  $\rho = \sqrt{x^2 + y^2}$  only. The  $(x, y)$ -dependence of the refractive index is physically achieved by using different materials for different layers of the fiber. The most typical cylindrically symmetric fiber is a thin

rod of material with a refractive index  $n_1$  surrounded by material with a lower refractive index  $n_2$ . The surrounding material could be air, which would result in a very simple fiber consisting of nothing but a rod of glass, for example. Nothing restricts us to solid materials, and the fundamental phenomena behind optical fibers can be (and have been) demonstrated using a stream of water. However, it will be shown that for many applications it is beneficial to make  $n_2$  only slightly lower than  $n_1$ , which in practice means surrounding the fiber *core* with a *cladding* layer. Usually the core and cladding are made of the same material, but the core has been doped with an additional substance in order to make its index of refraction higher [54].

## 3.2 Wave Propagation in Step-Index Fiber

The step-index fiber is probably the simplest case, but understanding how electromagnetic waves propagate in such fibers gives practical insight into propagation in other types of fibers, too. Consider a step-index fiber concentric with the  $z$ -axis. The fiber is described by a refractive index profile

$$n(\rho) = \begin{cases} n_1, & \rho \leq a \\ n_2, & \rho > a \end{cases}, \quad (3.12)$$

where  $\rho = \sqrt{x^2 + y^2}$  and  $a$  is the fiber core radius. Note that we are assuming an infinite cladding layer, but we will see that this is of no concern. Because of the cylindrical symmetry, we will express equation 3.11 in cylin-

dricial coordinates  $\rho$ ,  $\phi$  and  $z$  such that  $x = \rho \cos \phi$  and  $y = \rho \sin \phi$ . The Helmholtz equation 3.11 then reads

$$\frac{\partial^2 \tilde{\mathbf{E}}}{\partial \rho^2} + \frac{1}{\rho} \frac{\partial \tilde{\mathbf{E}}}{\partial \rho} + \frac{1}{\rho^2} \frac{\partial^2 \tilde{\mathbf{E}}}{\partial \phi^2} + \frac{\partial^2 \tilde{\mathbf{E}}}{\partial z^2} + k^2(\omega) \tilde{\mathbf{E}} = 0. \quad (3.13)$$

Now  $k^2(\omega) = k_0^2 n_1^2$  inside the fiber core and  $k^2(\omega) = k_0^2 n_2^2$  outside the core, where the  $\omega$ -dependence of  $n_1$  and  $n_2$  has been left out to shorten the notation. A similar equation can be derived for the magnetic field strength  $\tilde{\mathbf{H}}$ , and as  $\tilde{\mathbf{E}}$  and  $\tilde{\mathbf{H}}$  must also satisfy Maxwell's equations, only two components of the six  $\tilde{E}_\rho$ ,  $\tilde{E}_\phi$ ,  $\tilde{E}_z$ ,  $\tilde{H}_\rho$ ,  $\tilde{H}_\phi$ ,  $\tilde{H}_z$  are independent [55]. Typically  $\tilde{E}_z$  and  $\tilde{H}_z$  are chosen and they can be seen to satisfy equation 3.13.

The Helmholtz equation can be shown to be separable in cylindrical coordinates for a constant  $k$  using Stäckel determinants [56]. We can thus solve the equation in the core and in the cladding by separation of variables and then require the tangential components of the electric and magnetic fields be continuous at the core-cladding interface. The general form of such a separable solution can be shown to be

$$\tilde{E}_z(\omega, \rho, \phi, z) = A(\omega) F(\omega, \rho) \exp(\pm im\phi) \exp(i\beta z), \quad (3.14)$$

where  $A(\omega)$  is the amplitude of the frequency component oscillating at  $\omega$ ,  $\beta$  is the propagation constant that takes the role of the wave number  $k$ ,  $m$  is

an integer and  $F(\omega, \rho)$  is a solution of

$$\frac{d^2 F}{d\rho^2} + \frac{1}{\rho} \frac{dF}{d\rho} + \left( k^2 - \beta^2 - \frac{m^2}{\rho^2} \right) F = 0, \quad (3.15)$$

where  $k = k_0 n_1$  for  $\rho \leq a$  and  $k = k_0 n_2$  for  $\rho > a$ . Note that  $k$  and  $\beta$  depend on  $\omega$ . Equation 3.15 is Bessel's differential equation, and the physically feasible (i.e. no singularities, finite energy, differentiable) solutions are given by

$$F(\omega, \rho) = \begin{cases} J_m(\kappa\rho), & \rho \leq a \\ K_m(\gamma\rho), & \rho > a \end{cases}, \quad (3.16)$$

where  $\kappa = \sqrt{n_1^2 k_0^2 - \beta^2}$  and  $\gamma = \sqrt{\beta^2 - n_2^2 k_0^2}$ , and  $J_m$  and  $K_m$  are the Bessel function and the modified Bessel function of order  $m$ , respectively. Because  $K_m$  is an exponentially decaying function, the cladding does not have to be infinite in practice but thick enough so that  $K_m(\gamma\rho)$  becomes negligible at the fiber boundary.  $\tilde{H}_z$  can be obtained in a similar manner [55]. The boundary condition that the tangential components of  $\tilde{\mathbf{E}}$  and  $\tilde{\mathbf{H}}$  are continuous means that  $\tilde{E}_z$ ,  $\tilde{H}_z$ ,  $\tilde{E}_\phi$ , and  $\tilde{H}_\phi$  are to be continuous at  $\rho = a$ , which translates to the following eigenvalue equation [55]:

$$\left[ \frac{J'_m(\kappa a)}{\kappa J_m(\kappa a)} + \frac{K'_m(\gamma a)}{\gamma K_m(\gamma a)} \right] \left[ \frac{J'_m(\kappa a)}{\kappa J_m(\kappa a)} + \frac{n_2^2 K'_m(\gamma a)}{n_1^2 \gamma K_m(\gamma a)} \right] = \left( \frac{m\beta k_0 (n_1^2 - n_2^2)}{a n_1 \kappa^2 \gamma^2} \right)^2. \quad (3.17)$$

In general, equation 3.17 has multiple solutions for  $\beta$  for each integer value of  $m$ . The solutions are usually denoted by  $\beta_{mn}$ , and each  $\beta_{mn}$  corresponds

to a specific *mode* supported by the fiber, and the corresponding modal field distribution can be obtained from equation 3.14 [55]. Note, however, that imaginary electric fields are physically infeasible, and one has to take the real part of the complex distribution to get the physical electric field distribution.

There are two different types of modes, denoted by  $HE_{mn}$  and  $EH_{mn}$ , corresponding to whether the longitudinal magnetic field or electric field component is dominant [55]. As a special case we mention the TM and TE modes, where the longitudinal magnetic or electric field component is identically zero, respectively. Even though the mode naming convention refers to the longitudinal field components, these components are generally negligible compared to the transverse ones in many cases of practical interest. Weakly guiding optical fibers are one such case. Neglecting the longitudinal components simplifies the mathematical treatment of modes considerably and leads to degeneracy between various modes. For weakly guiding fibers the degenerate modes can be combined to yield a basis where all the modes are fully linearly polarized. Figure 3.1 shows the color-coded intensity distribution for eight different linearly polarized modes.

With the exception of the fully rotationally symmetric TM and TE modes, each mode has two orthogonal polarizations. Ideally, the two orthogonal polarizations would propagate at the same velocity but in practice fibers can never be fully rotationally symmetric and the degeneracy between the two polarizations is broken. This is called *polarization mode dispersion* (PMD) and will be discussed in more detail later [55].

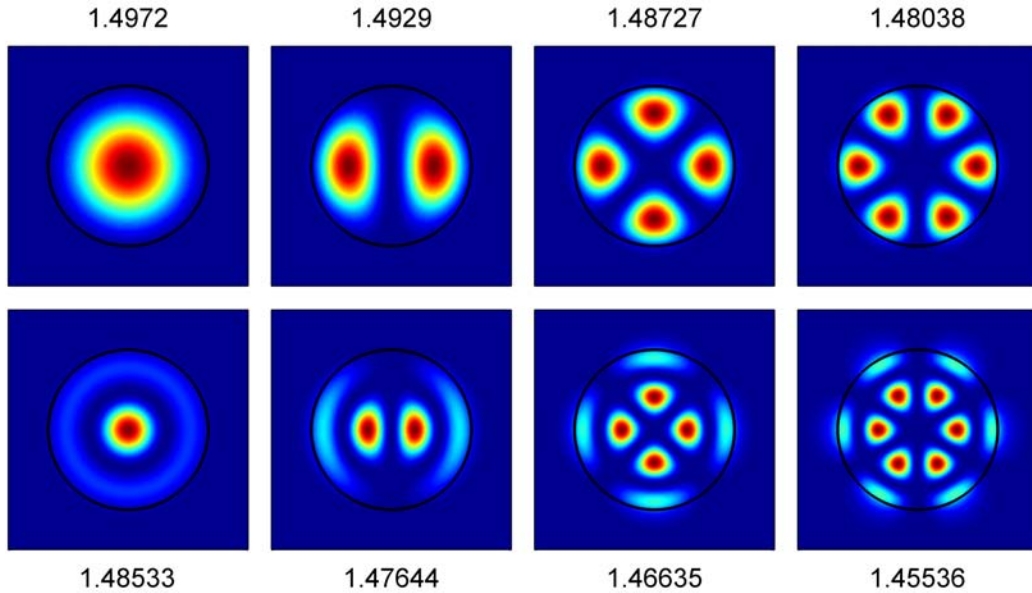


Figure 3.1: Transverse intensity profiles of some of the supported modes of a fiber. The core radius of the fiber is  $a = 2 \mu\text{m}$ , the refractive index of the core  $n_1 = 1.5$ , and the refractive index of the cladding  $n_2 = 1.45$ . The wavelength is 532 nm, which corresponds to a typical green diode pumped solid state frequency doubled laser pointer. The effective refractive indices of the modes are shown above or below their intensity profiles.

The  $z$ -dependence of the electric field of the mode corresponding to  $\beta_{mn}$  can be seen from equation 3.14. The dependence is simply  $\exp(i\beta_{mn}z)$ , which describes a wave propagating in the  $z$ -direction. The time-dependence of a frequency component at  $\omega$  is  $\exp(-i\omega t)$ , so the speed of this component is  $\omega/\beta_{mn}$ . Recalling that the index of refraction is  $c$  divided by the speed of light in the medium we can define the *modal index* or *effective refractive index* as  $\bar{n}_{mn} = \beta_{mn}c/\omega = \beta_{mn}/k_0$ , where  $k_0$  is the vacuum wave number. The modal index is smaller for larger  $m$  and  $n$  and remains between the core and cladding indices  $n_1$  and  $n_2$ , which can be seen in figure 3.1. The physical

explanation is that for large  $m$  and  $n$ , a larger portion of the intensity is confined in the cladding where light propagates faster. This is especially visible in figure 3.1 for the rightmost mode in the lower row.

Because the modal index is different for each mode, different modes propagate at different velocities. This is called *intermodal dispersion*. Needless to say, like all kinds of dispersion, also intermodal dispersion limits the performance of optical communication systems in the general case. Consider for example the two leftmost modes in figure 3.1, the modal indices of which are approximately 1.497200 and 1.485327. Assume we have a narrow initial pulse, the energy of which is divided between the modes. After 10 km of propagation in the fiber, the pulse has been split in two (or more) pulses that are separated by approximately 390 nanoseconds, which means a bit rate limitation of 2.6 Mbps due to intermodal dispersion alone. While 2.6 Mbps might be better than a semaphore line, it is nowhere near what can be achieved using a single mode fiber, and it is thus usually beneficial to have the fiber support the  $\text{HE}_{11}$  mode only.  $\text{HE}_{11}$  is referred to as the *fundamental mode*.

### 3.3 Single-Mode Operation and Properties of the Fundamental Mode

The number of supported modes is determined by the number of solutions to the eigenvalue equation 3.17, so if the equation can be set to have only

one solution, the fiber will only support one mode. It is useful to define a normalized frequency or the  $V$ -parameter as

$$V = \frac{2\pi}{\lambda_0} a \sqrt{n_1^2 - n_2^2}, \quad (3.18)$$

where  $\lambda_0$  is the wavelength in vacuum. The magnitude of  $V$  determines the supported modes, and the cutoff condition in terms of  $V$  can be derived for every mode [53]. Since we are only interested in single-mode operation, it suffices to state the *single-mode condition*:  $V = V_c$ , where  $V_c \approx 2.405$  is the first zero of the Bessel function  $J_0$  [i.e. the smallest positive solution of  $J_0(V_c) = 0$ ]. Even though single-mode operation could be guaranteed by making  $V$  small by tuning the refractive indices or making the core diameter small, the  $V$ -parameters of single-mode fibers are usually in the range 2.0-2.4 [54]. This is because fibers with a small  $V$ -parameter have higher bending losses, which is also intuitively clear: it is harder for the light to stay in the core in the presence of perturbations if the core diameter is small or the refractive index of the cladding is close to that of the core.

The transverse intensity profile of the fundamental mode was derived in section 3.2 and is given by

$$F(\rho) = \begin{cases} J_0(\kappa\rho), & \rho \leq a \\ K_0(\gamma\rho), & \rho > a \end{cases}, \quad (3.19)$$

where  $\kappa = \sqrt{n_1^2 k_0^2 - \beta^2}$ ,  $\gamma = \sqrt{\beta^2 - n_2^2 k_0^2}$ , and  $\rho = \sqrt{x^2 + y^2}$  is the radial

distance from the fiber center. Although the intensity distribution could be solved analytically, piecewise defined functions involving Bessel functions can be inconvenient to deal with, and it is customary to use a Gaussian approximation:

$$F(\rho) \approx \exp\left(-\frac{\rho^2}{w^2}\right), \quad (3.20)$$

where the width parameter  $w$  is determined by fitting the Gaussian function to the exact solution. For  $V$ -parameter values between 2 and 3, the width parameter is approximately equal to the core radius  $a$  and the ratio  $w/a$  increases with decreasing  $V$  [55]. Thus, for smaller values of  $V$ , a significant portion of the light propagates in the cladding.

### 3.4 Dispersion

The frequency-dependence of the refractive index, which leads to chromatic dispersion, is not the only source of dispersion. Other properties of light or the medium can affect the speed of light as well. As mentioned before, light intensity can also affect the speed of light, and in the context of water waves this would be called *amplitude dispersion*. In optics, however, the intensity-dependence of the refractive index is typically treated in the context of nonlinearities, separate from linear dispersive effects. The next section will be devoted to nonlinear optical effects and in this section we briefly discuss different types of linear dispersion.

### 3.4.1 Chromatic Dispersion

The physical meaning of the refractive index  $n(\omega)$  is that the velocity of the frequency component at  $\omega$  is  $v = c/n(\omega)$ . In other words, the refractive index is the ratio of the vacuum speed of light and the speed of light in the medium. The frequency-dependence of the refractive index is thus responsible for the aforementioned chromatic dispersion in bulk media.

The situation is somewhat different in optical fibers because the propagation speed of a certain frequency component depends not only on the corresponding bulk refractive index but also on waveguide geometry. The bulk effect is then referred to as *material dispersion* and the dependence on waveguide geometry is known as *waveguide dispersion*. Waveguide dispersion arises because the transverse modal distribution given in equation 3.16 depends on the wavelength and some frequencies are more concentrated in the fiber core that has a higher refractive index. Frequency components that penetrate deeper into the cladding layer experience an overall lower refractive index and thus propagate faster. Both material and waveguide dispersion contribute to the chromatic dispersion in fibers, and both of them are incorporated into the mathematical model via the frequency-dependence of the propagation constant  $\beta(\omega)$ .

The exact functional form of  $\beta(\omega)$  is usually neither known nor needed across the whole electromagnetic spectrum, and a Taylor approximation in the vicinity of a frequency of interest  $\omega_0$  (usually the central frequency of an

input pulse) can be used:

$$\beta(\omega) \approx \sum_{n=0}^N \frac{\beta_n}{n!} (\omega - \omega_0)^n \quad (3.21)$$

As is known from basic Fourier analysis, a short pulse must have a broad spectrum, and a narrow spectrum means a long pulse or a continuous wave. A long pulse might also have a broad spectrum if the pulse is chirped, and the amount of terms needed in the Taylor approximation for  $\beta(\omega)$  depends on how broad the spectrum is and how the dispersion behaves across the spectrum. Because of chromatic dispersion, the velocities of different spectral components of a pulse can differ significantly. This can cause pulses to broaden and become chirped, and chromatic dispersion is of utmost importance in nearly every fiber optical system simply because of its effect on light pulses.

The Taylor expansion is convenient mathematically but also offers some insight to the behavior of light in the waveguide, as some of the Taylor series coefficients in expansion 3.21 have a clear physical meaning. The first derivative is the inverse of the *group velocity*:  $v_g = \beta_1^{-1} = (\partial\beta/\partial\omega)^{-1}$ , and the physical meaning of the group velocity is that the envelope of a wave packet propagates at the group velocity. The second derivative  $\beta_2$  is responsible for *group-velocity dispersion* (GVD), which leads to pulse broadening, and  $\beta_2$  is called the GVD parameter. The temporal broadening of a pulse is governed by  $\Delta T = L\beta_2\Delta\omega$ , where  $L$  is the length of the fiber and  $\Delta\omega$  is the spectral

width of the pulse [54]. Second-order dispersion also causes pulses to become chirped. The sign of  $\beta_2$  has a tremendous impact on pulse propagation, and the case  $\beta_2 < 0$ , which is known as *anomalous dispersion*, is usually the most interesting one in fiber optics because it allows for more versatile phenomena [54, 19, 55, 57]. The situation  $\beta_2 > 0$  is referred to as *normal dispersion*, and it would cause the high-frequency components lag behind the low-frequency ones causing positive chirp on the pulse, as shown in figure 3.2 that shows the analytically solved propagation of a Gaussian pulse in the presence of GVD and the absence of higher-order dispersion. Figure 3.2 also shows how the pulse envelope remains Gaussian in the absence of higher-order dispersion although the pulse broadens, decreases its amplitude, and develops the already mentioned positive chirp. Note that third-order dispersion would both make the exact solution mathematically more tedious and distort the Gaussian envelope shape asymmetrically (see figure 3.3) [54]. Between the regions of normal and anomalous dispersion lies the wavelength for which  $\beta_2 = 0$ . This wavelength is termed the *zero-dispersion wavelength (ZDW)*, and there might be more than one such wavelengths [58] or a range of wavelengths for which  $\beta_2 \approx 0$  [59]. Because the magnitude of pulse broadening is governed by  $\beta_2$  via a linear relation, pulses with a central wavelength near the ZDW experience the least broadening. Pure silica has a ZDW of  $1.276 \mu\text{m}$ , and the ZDW of silica fibers usually varies in the range  $1.28 - 1.31 \mu\text{m}$  due to doping and the effect of waveguide dispersion. Thus, pulses with a central wavelength around  $1.3 \mu\text{m}$  usually experience the least broadening in silica fibers, and

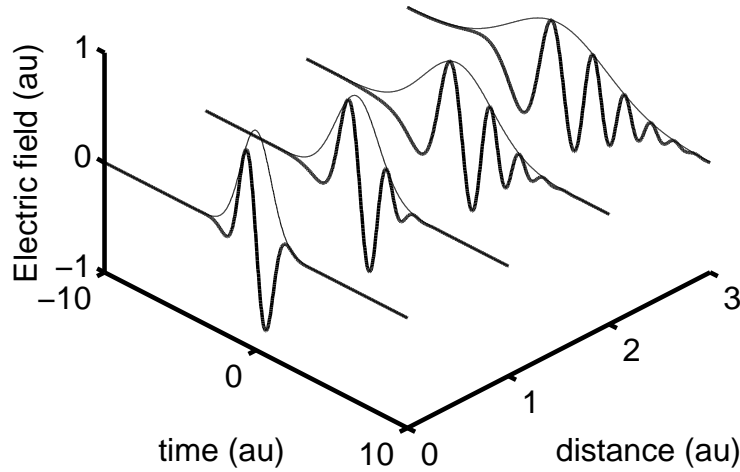


Figure 3.2: Evolution of the electric field (thick line) and the envelope (thin line) of a Gaussian pulse experiencing dispersion up to second order. The pulse envelope remains Gaussian upon propagation, but second-order dispersion causes the pulse to broaden, decrease its amplitude, and develop a chirp.

it would therefore be beneficial to operate optical communication systems in the vicinity of  $1.3 \mu\text{m}$ . However, losses are quite high at that wavelength, and high losses would necessitate the use of higher pulse energies, which is, of course, undesirable from a practical point of view. The losses can be made smaller by for example reducing the amount of  $\text{H}_2\text{O}$  molecules caught inside the fiber during the manufacturing process [54]. Even the purest of silica fibers are not completely lossless simply because the silica molecules can absorb photons, and instead of trying to reduce the losses around  $1.3 \mu\text{m}$  physicists have come up with a more cunning technique of *dispersion shifting* [60, 61, 62]. Dispersion shifting means changing waveguide and material dispersion through modifying waveguide geometry and/or the refractive index

profile by doping the core and the cladding in such a way that the ZDW falls in a desired wavelength range. The ZDW can be made to coincide with the wavelength that experiences the lowest losses ( $1.55 \mu\text{m}$ ). These kind of fibers are very suitable for optical communication applications because of low losses and low GVD.  $\beta_2$  can also be made small over a wide range of wavelengths, and fibers like this are known as *dispersion flattened fibers* [54]. Because of this property, dispersion flattened fibers are suitable for multichannel optical communication applications, where pulses of different central frequencies copropagate.

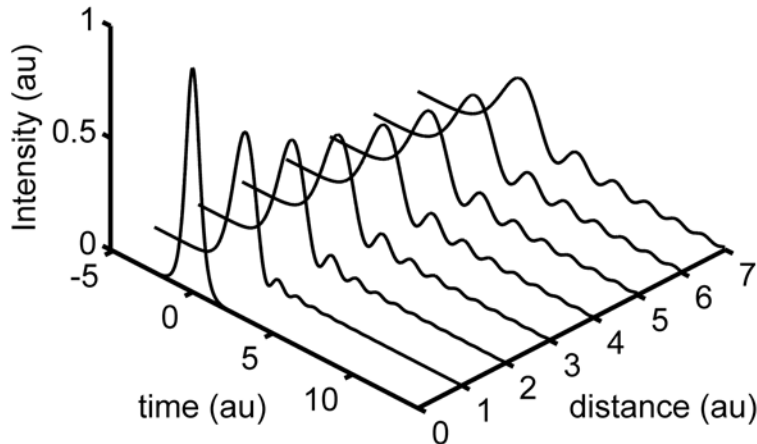


Figure 3.3: The evolution of the temporal intensity profile of an initially unchirped Gaussian pulse under the influence of third-order dispersion. The intensity profile becomes asymmetric and develops an oscillatory tail upon propagation.

When the central wavelength of the pulse in question is close to the ZDW, it becomes necessary to include third-order dispersion (TOD)  $\beta_3$  in the Taylor series 3.21. Similarly, the second-order Taylor approximation around  $\omega_0$  is

only valid in a certain range near  $\omega_0$ , and if the pulse spectrum is wider than this range, more terms have to be included in the Taylor series. The effect of third-order dispersion on pulses is to make the pulse envelope asymmetric and cause oscillatory behavior in one of the edges depending on the sign of  $\beta_3$ . In telecom applications the oscillatory behavior occurs usually in the trailing edge for unchirped symmetric pulses as shown in figure 3.3. The broadening (RMS-width) of a Gaussian pulse can still be solved analytically when third-order dispersion is included in the model [55].

The effects of dispersion of orders higher than three are far less intuitive, but the higher-order terms have to be included in the model because the spectrum becomes, by definition, very broad during supercontinuum generation. While the inclusion of dispersion only up to the second or third order simplifies analytical treatments and is sufficient for studies regarding the propagation of spectrally narrow single pulses, the lack of higher-order dispersion terms can yield unphysical results when the pulse spectrum becomes broad.

### 3.4.2 Intermodal Dispersion

The solutions  $\beta_{mn}$  of the eigenvalue equation 3.17 depend on the values of  $m$  and  $n$ , which means that the propagation constant is different for different modes of the fiber and different modes thus propagate at different speeds. Although the situation in planar waveguides is a bit different than in fibers, the geometric perspective of wave propagation in planar waveguides

offers an insightful explanation of intermodal dispersion. The simplest planar waveguide consists of two parallel mirrors, and light bounces back and forth between the mirrors. The reflection upon the mirrors corresponds to the total internal reflection present in step-index fibers. Solving Maxwell's equation for the planar waveguide yields the modes of the waveguide. One can then show that in the geometric interpretation, where light travels as rays in straight lines, the modes correspond to rays that fulfill the so-called *self-consistency condition* which means that the wavefront must reproduce itself after two reflections as shown in figure 3.4 [1].

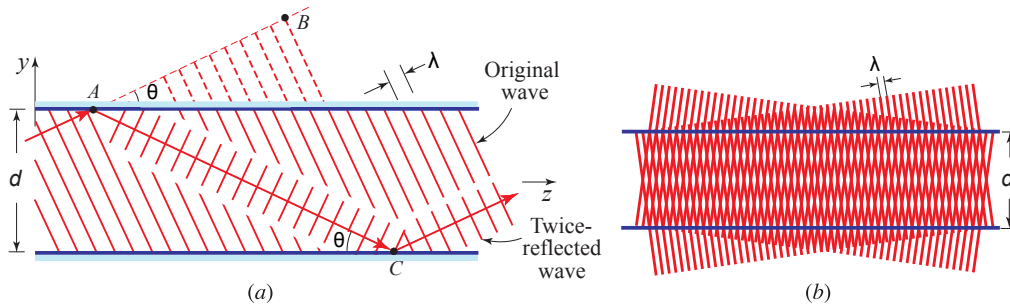


Figure 3.4: (a) A planar waveguide and a self-consistent ray of light. (b) The copropagation of self-consistent rays leads to an intensity distribution that is constant over the length of the waveguide. (After reference [1].)

There are multiple values of the propagation angle  $\theta$  that lead to the fulfillment of the self-consistency condition, and it is evident that the larger the propagation angle, the slower the ray propagates in the  $z$ -direction. Thus, in the geometrical picture, some modes travel longer distances than others and therefore appear to travel slower. The situation is a bit different in optical fibers, but the principle is similar.

### 3.4.3 Polarization Mode Dispersion

All fibers support two (ideally) degenerate modes polarized in orthogonal directions [55]. However, the propagation constants for these two modes are in general different because of birefringence, which means that the polarization components propagate at different speeds. The axis along which light has to be polarized in order to experience the lowest refractive index is called the *fast axis* because light polarized along that axis travels faster. The axis of the highest refractive index is called the *slow axis*. Unless the light is polarized along the fast or the slow axis, the state of polarization will change with propagation distance from linear to elliptical and back to linear in a periodic manner assuming the principal axes do not change their orientation [63]. This behavior is similar to the operational principle of wave plates [7]. However, because of the manufacturing process, the birefringence and the axes actually change randomly along the fiber [54]. This is due to random variations in the core shape, size, stress, and possible doping.

Even for fibers with randomly varying birefringence, two principal axes exist, and light polarized along one of these axes will exit the fiber with its state of polarization maintained [55]. Usually, however, one does not know or care about the state of polarization, and the effect of PMD is simply to broaden the pulses. Modeling such random PMD is easy by dividing the fiber into small segments such that the orientation of the fast axis and possibly the magnitude of birefringence in each segment are randomly selected. Thus, in each segment one polarization component lags behind the other component

by a certain time delay. This situation can easily be seen to be equivalent to the one-dimensional random walk, and the RMS-distance of such a random walk is known to obey the square-root law: when enough steps are taken, the expected positive distance from the initial location after  $N$  steps is proportional to  $\sqrt{N}$ . One might thus expect the PMD-induced pulse broadening in a fiber of length  $L$  to be proportional to  $\sqrt{L}$ , if the fiber is long enough. This turns out to be the case, as shown by the more detailed treatment by Foschini and Poole [64]. The fiber length  $L$  has to satisfy  $L > l_c$ , where  $l_c$  is the correlation length over which two polarization components remain correlated (typically of the order of 100 meters) [55]. The typical fiber lengths used in SC generation tend to be much smaller than 100 meters, and it is customary to neglect the effects of birefringence and use the scalar propagation equation because it has been shown to agree with experiments [19], but some authors [65, 66] insist on using coupled equations to describe pulse propagation. PMD is more important in other optical applications, such as communication systems, as PMD-induced pulse broadening can become a limiting factor for long-haul high-speed optical communication systems operating near the ZDW [67]. Modern communication systems utilize digital signal processing to compensate for PMD [68]. Interestingly enough, it has been shown [69] that accurate long-range measurements of PMD in fibers can be performed by using supercontinuum.

Some applications are sensitive to the polarization of the light, and it is sometimes desirable that the fiber does not alter the state of polarization of

the light [55]. *Polarization-maintaining fibers* can be made by intentionally inducing a large amount of birefringence by either making the fiber core non-circular on purpose or by inserting stress-inducing elements (typically two borosilicate rods) on the opposite sides of the fiber core [70, 71]. The large magnitude of the intentionally induced birefringence masks smaller random variations, and light polarized along the fast or the slow axis will maintain its state of polarization. For highly birefringent fibers the polarization effects become important also in terms of SC generation, and this has been studied in microstructured fibers [72, 73]. In one of these studies Lehtonen et. al [72] pointed out that the different dispersion characteristics of the two eigenpolarizations make it possible to generate two orthogonally polarized supercontinua with different properties, and all the possible combinations of these allow for more supercontinuum tunability.

## Chapter 4

# Nonlinear Effects in Fibers

In general, the response of a material to an external electric field is nonlinear and the nonlinear polarization

$$\mathbf{P}_{\text{NL}}(\mathbf{r}, t) = \varepsilon_0 \sum_{n=2}^{\infty} \chi^{(n)}(\mathbf{r}, t) * \mathbf{E}^n(\mathbf{r}, t) \quad (4.1)$$

consists of all terms of higher-order. For centrosymmetric materials, such as silica, all even order susceptibilities can be shown to be zero. Although fifth-order susceptibilities as high as  $1.9 \cdot 10^{-12} \text{ (m/V)}^4$  have been reported for gases of cold atoms [74], the fifth-order effects usually require intensities high enough to ionize the material, in which case the model obviously does not even work anymore. For reasonably low optical intensities in silica fibers all but the third-order contributions can be neglected. Alternatively, a possible way to take higher-order nonlinearities into account is to make the third-order susceptibility intensity-dependent appropriately [55]. In this thesis, susceptibilities of order higher than three will not be considered. The

nonlinear polarization then reduces to

$$\mathbf{P}_{\text{NL}}(\mathbf{r}, t) = \varepsilon_0 \iiint_{\mathbb{R}^3} \chi^{(3)}(t - t_1, t - t_2, t - t_3) \mathbf{E}(\mathbf{r}, t_1) \mathbf{E}(\mathbf{r}, t_2) \mathbf{E}(\mathbf{r}, t_3) dt_1 dt_2 dt_3. \quad (4.2)$$

The tensorial nature of the third-order susceptibility allows for phenomena such as nonlinear birefringence, but we can justifiably treat  $\chi^{(3)}$  as a scalar for most purposes. The third-order response in optical fibers is mostly due to the nearly instantaneous electronic response and partially due to the delayed molecular response. The electronic response times are of the order 0.1 fs, a time scale similar to the period of revolution for an electron in a Bohr orbit [54], though much longer response times have been demonstrated in certain special cases [75]. The molecular response, the Raman effect, happens on a timescale from 60 to 70 femtoseconds [55].

Although the third-order susceptibility is the only higher-order susceptibility of interest in the case of silica fibers, not all third-order phenomena are of interest when considering nonlinear propagation of light in silica fibers. This section discusses different third-order effects.

## 4.1 Third-Harmonic Generation

Third-harmonic generation (THG) or frequency tripling is a process where part of the energy of light at frequency  $\omega$  is converted into light at  $3\omega$ . Here, THG refers solely to the  $\chi^{(3)}$ -process, although the third-harmonic can also

be generated through a cascaded second-order process (namely, frequency doubling followed by sum-frequency generation). THG was first observed experimentally in 1962 using calcite crystals [76].

Chromatic dispersion causes the third-harmonic field at  $3\omega$  and the fundamental field at  $\omega$  to propagate at different speeds in the medium. Because the third-harmonic is generated throughout the medium, it is intuitively easy to understand that the third-harmonic electric fields generated in different parts of the medium are out-of-phase and cancel out due to this *phase-mismatch*. A rigorous treatment of this phenomenon requires a more thorough quantum-electrodynamical approach [8], but it suffices to state that because of the phase-mismatch, THG is not an efficient process unless specific care is taken to ensure that the fundamental field and the third-harmonic propagate at the same speed.

Phase-matching can be achieved because other types of dispersion can, in some circumstances, cancel chromatic dispersion. The most typical scheme exploits PMD, but the use of modal dispersion in harmonic generation has also been reported for example in microstructured fibers [77]. PMD-based phase-matching relies on birefringence and the tensorial nature of the nonlinear susceptibility. In other words, light polarized along the ordinary or the extraordinary axis can create higher-order harmonics that are polarized along the other axis, and birefringence and careful adjustment of the polarization angle make it possible to achieve such a situation that the higher-order field and the fundamental field propagate at the same speed.

## 4.2 Kerr-Effect

Kerr-effect is the name given to the phenomenon in which the refractive index of light depends on the square of the electric field, the intensity. Although the observation of the Kerr-effect in optical fibers requires the use of intense laser fields, the Kerr-effect was discovered as early as 1875 by the Scottish physicist John Kerr. This is due to the fact that the electric field used in the early experiments was a static one: a static electric field changes the refractive index of a crystal in which light propagates. In nonlinear fiber optics, the change in the refractive index is caused by the electric field of the light itself, but the static “DC Kerr-effect” is still exploited in numerous optical applications, such as Kerr shutters [54].

The mathematical derivation of the phenomenon stems from the fact that the cube of a sinusoidal function of angular frequency  $\omega$  includes a term oscillating at the same frequency  $\omega$ . Raman scattering and the Kerr-effect will lead to the following simpler form of equation 4.2 [78]:

$$\mathbf{P}_{\text{NL}} = \varepsilon_0 \chi^{(3)} \mathbf{E}(\mathbf{r}, t) \int_0^{\infty} R(t_1) |\mathbf{E}(\mathbf{r}, t - t_1)|^2 dt_1, \quad (4.3)$$

where  $R(t)$  is the normalized nonlinear response function and it has been assumed that  $\mathbf{P}_{\text{NL}}$  and  $\mathbf{E}$  point in the same direction. The lower limit of the convolution can be set to 0 instead of  $-\infty$  because of the requirement of causality:  $R(t) = 0$  for  $t < 0$ . The response function  $R(t)$  includes both

the instantaneous electronic response and the delayed molecular response. The delayed molecular response leads to Raman scattering, and the instantaneous part of the response function models the Kerr-effect. Let us assume, for the time being, that the material only has the instantaneous Kerr response and no delayed nonlinearities (the Raman effects can be included later on). In this approximation the response function becomes a delta function:  $R(t) = \delta(t)$ . Assume that the electric field is polarized along the  $x$ -axis and centered around the carrier frequency  $\omega_0$ :  $\mathbf{E}(\mathbf{r}, t) = \hat{\mathbf{x}}E(\mathbf{r}, t) \cos(\omega_0 t + \varphi)$ . The nonlinear polarization of such a field is then

$$\mathbf{P}_{\text{NL}} = \hat{\mathbf{x}}\varepsilon_0\chi^{(3)}E^3(\mathbf{r}, t) \left[ \frac{3}{4} \cos(\omega_0 t + \varphi) + \frac{1}{4} \cos(3\omega_0 t + 3\varphi) \right]. \quad (4.4)$$

The term oscillating at  $3\omega_0$  is responsible for THG, which is ineffective in fibers and hence the term can therefore be dropped. The total polarization, including the linear and nonlinear contributions, is thus

$$\begin{aligned} \mathbf{P}_{\text{lin}} + \mathbf{P}_{\text{NL}} &= \hat{\mathbf{x}}\varepsilon_0\chi^{(1)}E(\mathbf{r}, t) \cos(\omega_0 t + \varphi) + \hat{\mathbf{x}}\varepsilon_0\frac{3}{4}\chi^{(3)}E^3(\mathbf{r}, t) \cos(\omega_0 t + \varphi) \\ &= \hat{\mathbf{x}}\varepsilon_0 \left[ \chi^{(1)} + \frac{3}{4}\chi^{(3)}E^2(\mathbf{r}, t) \right] E(\mathbf{r}, t) \cos(\omega_0 t + \varphi). \end{aligned} \quad (4.5)$$

The bracketed expression in Eq. 4.5 can be interpreted as an effective susceptibility  $\chi_{\text{eff}}$  consisting of the usual linear contribution from  $\chi^{(1)}$  as well as a field-dependent nonlinear contribution from  $\chi^{(3)}$ . Having an effective

susceptibility then allows us to define an effective refractive index through

$$n_{\text{eff}} = \sqrt{1 + \chi_{\text{eff}}} = \sqrt{1 + \chi^{(1)} + \frac{3}{4}\chi^{(3)}E^2(\mathbf{r}, t)}. \quad (4.6)$$

The nonlinear contribution to the effective index is very small compared to the linear one for any feasible optical powers below the damage threshold of silica and other common materials:  $1 + \chi^{(1)} \gg \frac{3}{4}\chi^{(3)}E^2(\mathbf{r}, t)$ . This allows us to approximate the expression inside the square root as:

$$n_{\text{eff}} = \sqrt{1 + \chi^{(1)}} \sqrt{1 + \frac{3}{4} \frac{\chi^{(3)}E^2(\mathbf{r}, t)}{1 + \chi^{(1)}}} \quad (4.7)$$

$$\approx \sqrt{1 + \chi^{(1)}} \left( 1 + \frac{3}{8} \frac{\chi^{(3)}E^2(\mathbf{r}, t)}{1 + \chi^{(1)}} \right) \quad (4.8)$$

$$= n_1 + \frac{3\chi^{(3)}E^2(\mathbf{r}, t)}{8n_1}, \quad (4.9)$$

where  $n_1 = \sqrt{1 + \chi^{(1)}}$  is the linear refractive index. Now noting that the intensity (averaged over one optical cycle) is  $I = \frac{1}{2}\varepsilon_0 n_1 c E^2$  allows us to write the effective refractive index as

$$n_{\text{eff}} = n_1 + \underbrace{\frac{3\chi^{(3)}}{4n_1^2\varepsilon_0 c}}_{\stackrel{\text{def}}{=} n_2} I = n_1 + n_2 I. \quad (4.10)$$

where  $n_2$  is the *nonlinear refractive index*. This form for the effective refractive index clearly shows the intensity-dependence. The nonlinear index  $n_2 > 0$  for silica, meaning that intense light experiences a larger effective

refractive index [79].

### 4.3 Self-Phase Modulation and Cross-Phase Modulation

The dependence of monochromatic light on propagation distance  $z$  and time  $t$  can be mathematically written as  $\exp[i(kz - \omega t)] = \exp[i(nk_0z - \omega t)]$  using complex fields. The complex phase is thus  $\phi = nk_0z - \omega t$ . When  $n$  depends on the intensity, the phase of the light will consequently be affected by the light itself. This is referred to as self-phase modulation (SPM). The instantaneous (angular) frequency is  $-d\phi/dt$ , and in the case of linear optics this would naturally reduce to  $\omega$ . When  $n$  depends on the intensity as  $n = n_1 + n_2I$ , the instantaneous frequency is

$$-\frac{d\phi}{dt} = \omega - k_0z \frac{d(n_1 + n_2I)}{dt} = \omega - k_0n_2z \frac{dI}{dt}. \quad (4.11)$$

Because  $n_2 > 0$ , the instantaneous frequency is lower at the leading edge of a pulse (where  $dI/dt > 0$ ) and higher at the trailing edge, as shown by figure 4.1. SPM therefore causes chirp in pulses. Note that the chirp is qualitatively similar to that caused by normal dispersion and the exact opposite of that caused by anomalous dispersion. Indeed, it turns out that the chirp caused by the Kerr-effect can precisely cancel the anomalous dispersion induced chirp for some cases [31, 32]. The nature of the Kerr-effect makes no distinction whether the intensity-dependence of the refractive index experienced by light

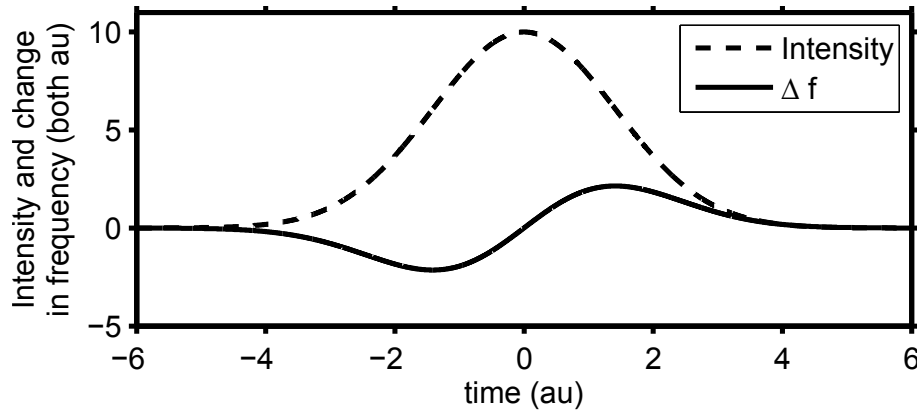


Figure 4.1: The change in frequency due to SPM for a Gaussian pulse at a certain propagation distance. The frequency change is shown by the solid line and the intensity profile by the dashed line.

at  $\omega_1$  is caused by light at the same frequency, and it is possible for light at another frequency  $\omega_2$  to affect the phase of light at  $\omega_1$ . This phenomenon is known as *cross-phase modulation* (XPM), as is also the situation where light polarized along a certain axis affects the phase of light polarized along another axis [55]. The distinction between SPM and XPM is not necessarily straightforward. A light pulse consist of multiple frequency components, and the effect of the pulse on its own phase is simply referred to as SPM. When neglecting polarization effects and deriving the nonlinear propagation equation, the difference between SPM and XPM is more evident in the frequency domain. In the time domain, SPM and XPM cause the propagation constant to become intensity-dependent.

Dispersion-induced chirp is simply due to the different propagation velocities of the frequency components, and the spectrum remains unchanged

because no energy is transferred from one frequency to another. SPM and XPM, however, are accompanied by the generation of new frequency components. This is referred to as SPM- or XPM-induced spectral broadening, and it is a dominating spectral broadening mechanism in the case of short-pulse SC generation [80]. The SPM-broadened spectrum of an initially Gaussian or sech-shaped pulse develops a multipeak structure with the number of peaks depending on the initial peak power and the propagation distance [55]. Under ideal conditions an initially symmetric spectrum would remain symmetric throughout the fiber, but in reality other nonlinear phenomena, such as Raman scattering, together with dispersion and pulse asymmetry will cause one side of the spectrum to grow more intense than the other.

Although SPM induces spectral broadening on unchirped pulses, it can make the spectrum of a chirped pulse narrower. A negatively chirped pulse has higher frequencies in the leading edge and lower frequencies in the trailing edge. SPM can then counteract the initial chirp and shift the frequencies of the edges closer to the central frequency, which then results in a narrower spectrum and the pulse becoming closer to a transform-limited one. A similar scheme can be used to compress unchirped pulses in time. A transform-limited pulse cannot be compressed without broadening its spectrum, and the SPM- or XPM-induced spectral broadening offers a way compress pulses in the anomalous dispersion regime. In that regime, the blue-shifted components generated in the trailing edge and the red-shifted components at the leading edge will both move towards the pulse center because of anomalous

dispersion, and the pulse will thus become shorter. Anomalous dispersion is not necessary if the dispersive effects can be compensated for at a later stage by using a prism compressor or a grating pair, for example. This technique was used as early as 1982 to generate 30 fs pulses [81], and subsequent experiments showed remarkable improvements in the following years [82].

## 4.4 Four-Wave Mixing

FWM (alternatively four-photon mixing) is another phenomenon related to the Kerr-effect. It describes the interaction of four photons at frequencies  $\omega_1$ ,  $\omega_2$ ,  $\omega_3$ , and  $\omega_4$ . Here FWM is understood to refer solely to processes where the photons at frequencies  $\omega_1$  and  $\omega_2$  are annihilated and photons at  $\omega_3$  and  $\omega_4$  are created, although some authors [55] categorize for example THG as a FWM process in which the three photons at  $\omega_1 = \omega_2 = \omega_3$  are annihilated and a photon at  $\omega_4 = 3\omega_1$  is created.

The energy of a photon is  $\hbar\omega$ , where  $\hbar = h_{\text{P}}/(2\pi)$ , and conservation of energy requires that the combined energy of the annihilated photons equals the energy of the photons created, so  $\omega_1 + \omega_2 = \omega_3 + \omega_4$ . On the other hand, the requirement of momentum conservation translates to an equation for the propagation constants:  $\beta(\omega_1) + \beta(\omega_2) = \beta(\omega_3) + \beta(\omega_4)$ , where  $\beta(\omega_i)$  is the propagation constant at frequency  $\omega_i$ . The momentum conservation condition  $\Delta k = \beta(\omega_3) + \beta(\omega_4) - \beta(\omega_1) - \beta(\omega_2) = 0$  is the phase-matching condition for the FWM process, and it is not exactly similar to the con-

ervation of momentum in classical mechanics since FWM also occurs when  $\Delta k \neq 0$  assuming the fiber length  $L$  satisfies  $L < L_c = 2\pi/\Delta k$ , where  $L_c$  is the so-called the coherence length. FWM is ineffective for longer fibers if the phase-mismatch is not compensated for.

The phase-matching condition is indeed very restrictive if there are four different frequencies involved because the frequency-dependence of the propagation constant is usually nontrivial, and this is the reason FWM involving four different frequencies is, for the most part, ineffective in optical fibers. The process becomes less complicated for *degenerate four-wave mixing* (DFWM), which refers to the situation  $\omega_1 = \omega_2$ . The phase-matching condition for DFWM is then  $\Delta k = \beta(\omega_3) + \beta(\omega_4) - 2\beta(\omega_1)$ , which can be easily satisfied either through SPM or by virtue of  $\lambda_1$ , the wavelength corresponding to  $\omega_1$ , being close to the ZDW [54]. Assume (without loss of generality) that  $\omega_4 > \omega_3$  and denote  $\Omega = \omega_4 - \omega_1 = \omega_1 - \omega_3$ . When the effects of SPM and XPM are taken into account and single-mode operation is assumed, the phase-mismatch is given by [19, 55]

$$\Delta k = 2\gamma P_0 + 2 \sum_{m=1}^{\infty} \frac{\beta_{2m}}{(2m)!} \Omega^{2m}, \quad (4.12)$$

where  $\gamma$  is the nonlinear coefficient,  $P_0$  is the pump peak power,  $\Omega$  is the angular frequency separation from the pump, and  $\beta_{2m}$  are the even order dispersion coefficients evaluated at the pump frequency. If  $\beta_2 < 0$ , or  $\beta_4 < 0$ , chances are the phase-matching condition will be at least approximately

satisfied for two frequency sidebands, and FWM provides the sidebands with an amplitude gain of  $g = \sqrt{(\gamma P_0)^2 - (\Delta k/2)^2}$ . Every frequency component in the sidebands will initially grow exponentially so that the initial sideband amplitude  $A_0^s$  will have grown to  $A_0^s \exp(gz)$  after a propagation distance of  $z$ . Note that this is the case only in the undepleted pump approximation, because as the pump loses some of its energy to the sidebands, its power decreases affecting the gain and the location of the sidebands. Also note that the gain exist only for  $g \in \mathbb{R}$ . The sideband of the lower frequency is called the *Stokes wave* and that of the higher frequency is called the *anti-Stokes wave*. [19, 55]

The phase-mismatch in equation 4.12 is power-dependent because of SPM, and hence FWM can be phase-matched because of the effect of SPM. When a CW at frequency  $\omega_0$  is amplitude-modulated with a sinusoidal signal at a modulation frequency  $\omega_m$ , the spectrum has, in addition to the CW peak at  $\omega_0$ , two smaller peaks at  $\omega_0 - \omega_m$  and  $\omega_0 + \omega_m$  (just take the Fourier-transform of  $[A + a \sin(\omega_m t)] \exp(-i\omega_0 t)$  to see this). The smaller peaks in the spectrum are thus symmetrically located around  $\omega_0$  with frequency separations of  $\pm\omega_m$ . If the phase-mismatch of equation 4.12 is approximately zero for  $\Omega = \pm\omega_m$ , the gain  $g$  will be real and positive at  $\Omega = \pm\omega_m$ , and the frequency components at  $\omega_0 - \omega_m$  and  $\omega_0 + \omega_m$  will be amplified upon propagation. In the temporal domain this means that the modulation contrast increases. A sinusoidal modulation of a suitable frequency will therefore initially be exponentially amplified, which is the reason why such SPM-phase-matched FWM

is called *modulation instability* (MI) [55].

Equation 4.12 together with the gain profile provides the mathematical explanation why MI amplifies narrow sidebands far away from the pump frequency in the normal GVD regime and broad sidebands close to the pump frequency in the anomalous GVD regime, as shown by figure 4.2. In the

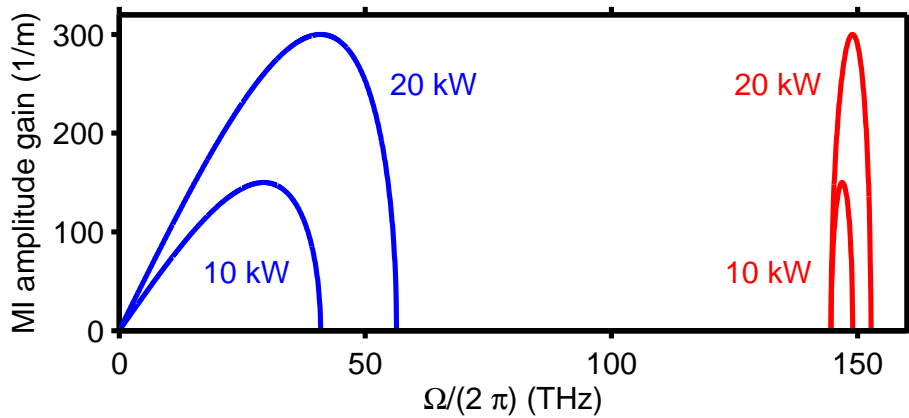


Figure 4.2: The MI gain as a function of frequency separation from the pump frequency of 283 THz for two different peak powers. The blue curve has  $\beta_2 = -8.56 \text{ ps}^2/\text{km}$  while  $\beta_2 = 8.56 \text{ ps}^2/\text{km}$  for the red curve. The nonlinear coefficient is  $\gamma = 0.015 \text{ (m} \cdot \text{W)}^{-1}$  and the higher-order dispersion terms are  $\beta_4 = -9.29 \cdot 10^{-5} \text{ ps}^4/\text{km}$  and  $\beta_6 = -9.79 \cdot 10^{-10} \text{ ps}^6/\text{km}$  for both curves.

normal dispersion regime  $\beta_2 > 0$ , and both  $2\gamma P_0$  and  $\beta_2 \Omega^2$  are positive, so the phase-matching condition cannot be satisfied for small frequency detunings.  $\Omega$  has to be large enough so that the higher-order terms, such as  $\Omega^4$  and  $\Omega^6$  start to dominate the sum and can cancel the positive terms of equation 4.12. Thus, the gain sidebands will be further away from the pump frequency. When  $\Omega$  is large and terms like  $\Omega^4$  dominate the sum, small variations in a

large  $\Omega$  lead to large changes in those dominating high-order terms, and the phase-matched frequency band will thus be narrow. The normal GVD case is shown in figure 4.2 by the red curves, and both the narrowness and the large frequency separation can be seen. Although spectrally flat supercontinua can be generated through cascaded Raman scattering by using long pump pulses in the normal dispersion regime [83, 84], anomalous pumping is more often preferred because of the (usually) desirable effect of broadband MI [85].

For small frequency detunings the dominating contribution to the sum in equation 4.12 comes from the second-order term involving  $\beta_2$ . The GVD parameter  $\beta_2$  is negative for anomalous dispersion, and in that case the sum can cancel the positive  $2\gamma P_0$  term leading to phase-matching for small detunings  $\Omega$ . When the dominating contribution to the sum comes from the second-order term, the value of the sum depends mostly on  $\Omega^2$ , so slight changes in the small  $\Omega$  will not change the sum considerably, which is why the gain sidebands are broad. The anomalous GVD case is shown by the blue curves of figure 4.2. When  $\Omega$  is small, the higher-order terms can be neglected, and one can readily see that the gain peaks at  $\Omega = \sqrt{2\gamma P_0/|\beta_2|}$  and has a peak value of  $g_{\max} = 2\gamma P_0$ , as shown by figure 4.2.

The preceding treatment assumed that the pump beam and the modulating signals are polarized along the same axis. When this is not the case, coupled equations have to be used in the mathematical treatment. Although the case of different polarizations is not considered here, it is worth mentioning that MI similar to the anomalous GVD regime can be observed for

a pump frequency at the normal GVD regime, if the modulating beam is orthogonally polarized with respect to the pump beam. Such MI is referred to as *vector modulation instability* [54].

When no initial modulation is present, noise takes the role of the perturbation. In this case of spontaneous MI, the entire MI gain band of frequencies will be amplified. The ability of FWM to amplify noise is sometimes beneficial and sometimes undesirable. FWM can also amplify existing signals instead of noise, which is why FWM is obviously harmful in WDM systems because it might deplete signals at some channels and disturb other channels. However, the power of FWM can also be harnessed for multiple applications such as parametric oscillators, channel demultiplexing, wavelength conversion, optical sampling, and high-speed optical switching [86]. The unwanted effect of FWM on WDM systems can be drastically reduced by the clever technique of dispersion management, where the fiber consists of different segments such that each segment has a high GVD to cause high phase-mismatch, but the GVD over the whole fiber averages to zero so that the detrimental effects of GVD become minimal [54]. Usually the GVD parameter is made to flip its sign from one segment to another. Another way to reduce the effects of FWM is to use unequal channel spacings so that the energy conservation condition  $\omega_1 + \omega_2 = \omega_3 + \omega_4$  is not easily satisfied [87].

The role of FWM and MI in SC generation become very clear in the long-pulse regime. MI causes the long pump pulse to break into a train of narrower pulses because of the amplified modulation. The forming pulses can

then collide with each other, exchange energy, broaden the spectrum further, and, most evidently, significantly affect the temporal characteristics of the signal. Some of the pulses adjust themselves to become solitons, which are nonlinear pulses of certain shape. Solitons will be discussed in more detail later on.

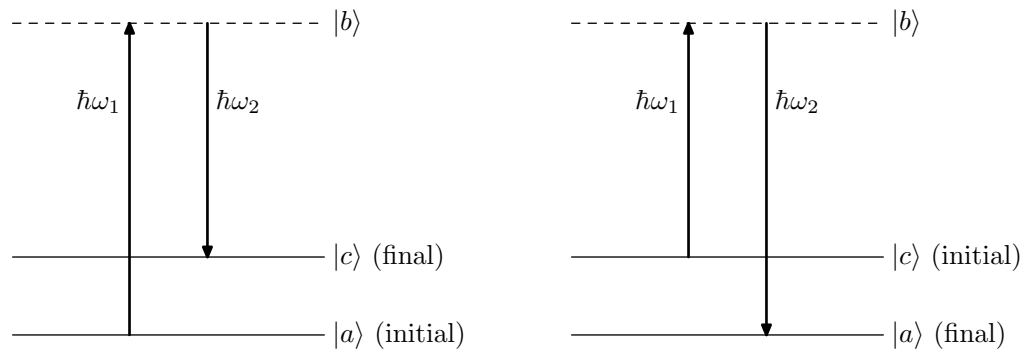
## 4.5 Stimulated Raman Scattering

The delayed nature of molecular and atomic response to external electric fields gives rise to the already mentioned effect known as Raman scattering after its discoverer [88]. The quantum mechanical description of the phenomenon is that it describes the interaction between a photon and an optical phonon, a quantum of lattice vibration. Note that photons can just as well interact with acoustic phonons, a phenomenon known as *Brillouin scattering*, but this will not be considered here because of its negligible effect for broad band signals and because Brillouin scattered light actually travels backwards in fibers [55].

In Raman scattering, a photon scatters inelastically from a molecule and transfers some of its energy to it causing the molecule to rise to a higher vibrational state. The photon thus loses some of its energy and its frequency must therefore decrease by an amount corresponding to the energy transferred to the molecule. The resulting electromagnetic wave of lower frequency is called the Stokes wave like in FWM. It is also possible for the molecule to release

some of its vibrational energy to a photon, which would result in an increase in the frequency of the photon. The resulting wave is the anti-Stokes wave. This kind of Raman scattering, however, is seldom observed because it requires the simultaneous presence of a photon and a phonon of suitable energies whereas the generation of a Stokes wave only requires a photon in a medium.

Figure 4.3 shows the energy states in the quantum mechanical treatment of Raman scattering. The Raman scattering process is treated quantum



The Stokes Raman transition.

The Anti-Stokes Raman transition.

Figure 4.3: Quantum mechanical description of Raman transitions. (After ref. [2].)

mechanically by assuming that the initial photon is absorbed, the molecule rises to a state of higher energy and then immediately transfers back to another lower energy state by emitting a photon. The anti-Stokes wave is generated similarly with the exception that the final energy state of the molecule is actually lower than the initial one, as shown in figure 4.3.

Raman scattering can occur spontaneously, but the case of most interest

in fiber optics is the so called *stimulated Raman scattering* (SRS) in which the presence of a Stokes wave seeds Raman scattering and the pump wave keeps amplifying the Stokes wave [89]. The frequencies which are amplified in the presence of a pump wave of a certain wavelength depend on the vibrational modes of the material in which the light propagates. The normalized Raman gain profile for fused silica is shown in figure 4.4, but there can be slight deviations from this in fibers due to doping and impurities. The actual unnormalized magnitude of Raman gain depends inversely on the wavelength of the pump beam. The effect of SRS is included in the mathematical model

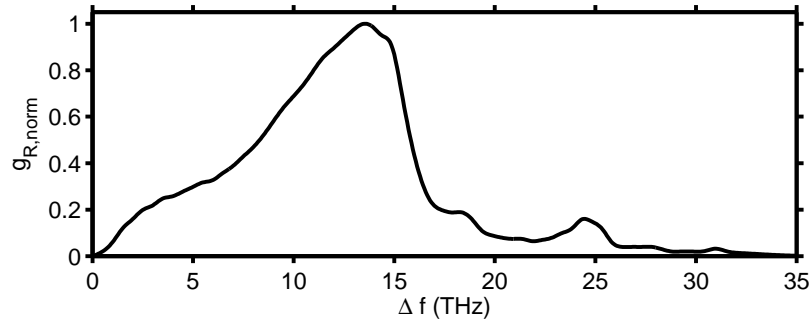


Figure 4.4: The normalized Raman gain profile of fused silica. The maximum gain occurs for a frequency shift of approximately 13.2 THz.

by the Raman response function  $h_R(t)$ , which is the delayed part of the response function  $R(t)$  mentioned in section 4.2. The function describes the time domain behavior of molecular vibrations, and the Raman gain is directly proportional to the imaginary part of the Fourier transform of  $h_R(t)$ , the real part being related to the so called parametric gain, which is then related to FWM [85].

The effect of Raman gain in SC generation is clear: it transfers energy from higher frequencies to lower frequencies. This can happen for example if two pulses with a suitable wavelength separation overlap in time and the pulse with the shorter wavelength transfers some of its energy to the other pulse. Short pulses may have a spectrum broader than the Raman gain bandwidth, and in that case the pulse transfers some of its own energy to lower frequencies upon propagation. This leads to red-shift of the pulse, and in the case of solitons this kind of intrapulse Raman scattering is known as soliton self-frequency shift [30]. The frequency shift per unit distance is inversely proportional to the fourth power of the duration of the soliton, which means that the red-shift can become very rapid for short solitons [55].

## 4.6 The Nonlinear Propagation Equation

The derivation of the propagation equation is mathematically somewhat cumbersome, and a good presentation of this is given in [55], but it is helpful to state the main assumptions and simplifications made during the derivation of the propagation equation. First, polarization effects are neglected and the electric field and the induced polarization are assumed to be parallel. Second, Brillouin scattering is neglected. Third, single-mode propagation is assumed. Note that this is not a numerical approximation since the fibers can be made to support one mode only. Fourth, only relevant third-order nonlinear effects are taken into account. THG is neglected because

of phase-mismatch, second-order effects are neglected because of centrosymmetry, and higher-order effects are neglected because of their minuscule contribution. Fifth, the nonlinearity is taken into account by using first-order perturbation theory, which means that the nonlinearity only affects the effective propagation constant  $\beta$  but not the modal field distribution  $F(x, y)$ . The effect of the nonlinearity on the effective refractive index is thus justifiably assumed small. Sixth, the frequency-dependence of the nonlinearity is taken into account through a linear approximation. Seventh, the electric field in the frequency domain centered around the frequency  $\omega_0$  is of the form  $\tilde{E}(\mathbf{r}, \omega - \omega_0) = \tilde{A}(z, \omega - \omega_0)F(x, y) \exp(i\beta_0 z)$ , where  $\tilde{A}$  is a slowly-varying function of  $z$  such that we can approximate

$$\frac{\partial^2 \tilde{E}}{\partial z^2} = F(x, y) \exp(i\beta_0 z) \left( \frac{\partial^2 \tilde{A}}{\partial z^2} + 2i\beta_0 \frac{\partial \tilde{A}}{\partial z} - \beta_0^2 \tilde{A} \right) \quad (4.13)$$

$$\approx F(x, y) \exp(i\beta_0 z) \left( 2i\beta_0 \frac{\partial \tilde{A}}{\partial z} - \beta_0^2 \tilde{A} \right). \quad (4.14)$$

This approximation is called the *slowly-evolving-wave approximation* (SEWA) and dictates that the envelope  $A$  is not to change considerably over a propagation distance of one wavelength [90]. Note that this approximation is not the same as the slowly-varying-envelope approximation and does not impose limitations on how many optical cycles must lie under the envelope  $A$ . The SEWA is still valid for pulses down to the single cycle regime [90].

Under the aforementioned assumptions and using the retarded time co-

ordinate  $T = t - \beta_1 z$ , equation 3.10 can be shown to lead to the following equation for the amplitude  $A(z, T)$ :

$$\begin{aligned} \frac{\partial A}{\partial z} + \frac{\alpha}{2} A - \sum_{k \geq 2} \frac{i^{k+1}}{k!} \beta_k \frac{\partial^k A}{\partial T^k} \\ = i\gamma \left( 1 + i\tau_{\text{shock}} \frac{\partial}{\partial T} \right) \left[ A \int_{-\infty}^{\infty} R(T') |A(z, T - T')|^2 dT' \right]. \end{aligned} \quad (4.15)$$

The left hand side models the dispersive effects ( $\beta_k$ ) and possible losses ( $\alpha$ ). Note that the losses in Eq. (4.15) are assumed constant across the whole spectrum, but frequency-dependent losses could be introduced by allowing the dispersion parameters ( $\beta_k$ ) to be complex numbers. The right hand side of Eq. 4.15 contains the effects of optical nonlinearities.  $\gamma$  is the nonlinear parameter and  $R(T)$  is the response function that includes both the instantaneous electronic contribution and the delayed molecular response. It is customary to use either a time-domain response function or the experimentally determined Raman profile [91] to model the Raman nonlinearity. The spectral Raman profile is essentially the Fourier transform of the time-domain Raman response function, a transfer function. We note that the linear Raman approximation cannot be used to accurately model the propagation of broadband optical pulses [92], and the full experimental Raman profile [91] is used in this study. The frequency-dependence of the nonlinearity is taken

into account with  $\tau_{\text{shock}}$ . The nonlinear parameter  $\gamma$  is given by

$$\gamma = \frac{\omega_0 n_2(\omega_0)}{c A_{\text{eff}}(\omega_0)}, \quad (4.16)$$

where  $A_{\text{eff}}$  is the effective mode area defined as

$$A_{\text{eff}} = \frac{\left( \int \int_{-\infty}^{\infty} |F(x, y)|^2 dx dy \right)^2}{\int \int_{-\infty}^{\infty} |F(x, y)|^4 dx dy}. \quad (4.17)$$

If the modal distribution is approximated by a Gaussian function as in equation 3.20, the effective mode area is simply  $A_{\text{eff}} = \pi w^2$ .

Equation 4.15 is the aforementioned GNLSE, and it has been shown to accurately model nonlinear broadband pulse propagation in optical fibers down to the single-cycle regime. [19, 90]. The scalar equation is valid if fiber birefringence can be neglected or if one assumes that the electric field is polarized along one of the principal axes of the fiber. Unless special care is taken, fibers are birefringent in practice both because of the material used and because of random variations in the fiber core shape. However, in this study polarization effects can be neglected simply by virtue of the short length of the fibers considered here [55].

## 4.7 Solving the GNLSE Numerically

The GNLSE admits no general analytical solutions for arbitrary input fields, and numerical methods to solve the equation have to be used instead. Equa-

tion 4.15 can be solved numerically by various finite difference and Runge-Kutta methods, but to this day the *split-step Fourier method* (SSFM) remains as one of the most sophisticated ones [55]. The Runge-Kutta procedure can also be implemented in this method for improved accuracy, but usually reducing the step size does the same in terms of increased accuracy and computational time.

The starting point for the SSFS is to write the GNLSE in the following operator form:

$$\frac{\partial A}{\partial z} = \left( \hat{D} + \hat{N} \right) A, \quad (4.18)$$

where

$$\hat{D} = -\frac{\alpha}{2} + \sum_{k \geq 2} \frac{i^{k+1}}{k!} \beta_k \frac{\partial^k}{\partial T^k} \quad (4.19)$$

is a differential operator accounting for losses and dispersion, and  $\hat{N}$  is a nonlinear operator accounting for fiber nonlinearities and the effect of which on  $A$  is defined by [55, 19]

$$\hat{N}A = i\gamma \left( 1 + i\tau_{\text{shock}} \frac{\partial}{\partial T} \right) \left[ A \int_{-\infty}^{\infty} R(T') |A(z, T - T')|^2 dT' \right]. \quad (4.20)$$

Note that the operator  $\hat{N}$  is  $z$ - and  $A$ -dependent while  $\hat{D}$  is not.

The SSFM is practically a finite difference method with respect to the spatial variable  $z$ , and one is eventually interested in calculating the value  $A(z + h, T)$  when  $A(z, T)$  is known. The formal exact solution of equation

4.18 for  $A(z + h, T)$  is given by

$$A(z + h, T) = \exp \left[ \int_z^{z+h} \left\{ \hat{D} + \hat{N}(z') \right\} dz' \right] A(z, T). \quad (4.21)$$

The integral of  $\hat{D}$  is trivially  $h\hat{D}$ , but the integral of  $\hat{N}$  is more tricky because of its dependence on  $z$  and unknown values of  $A$  between the interval  $[z, z+h]$ . The obvious way to deal with this is to make the step size  $h$  small enough such that  $A$  is approximately constant in the interval  $[z, z+h]$  and the integral can thus be approximated by the known value  $h\hat{N}(z)$ . A more sophisticated approach first exploits this approximation to calculate  $A(z + h, T)$  and then uses this approximate value and the trapezoidal rule to approximate the value of the integral. The iteration can then be continued to obtain better approximations for  $A(z + h, T)$ . Using the iterative trapezoidal procedure can reduce the computational time, but for simplicity it is not used in this treatment, and we simply approximate

$$A(z + h, T) \approx \exp \left[ h \left( \hat{D} + \hat{N} \right) \right] A(z, T). \quad (4.22)$$

For computational purposes, a further approximation of the exponential  $\exp \left[ h \left( \hat{D} + \hat{N} \right) \right]$  is needed. It relies on the Baker-Hausdorff formula for two non-commutating operators  $\hat{a}$  and  $\hat{b}$  [93]:

$$\exp(\hat{a}) \exp(\hat{b}) = \exp \left( \hat{a} + \hat{b} + \frac{1}{2}[\hat{a}, \hat{b}] + \frac{1}{12}[\hat{a} - \hat{b}, [\hat{a}, \hat{b}]] + \dots \right), \quad (4.23)$$

where  $[\hat{a}, \hat{b}] = \hat{a}\hat{b} - \hat{b}\hat{a}$  is the commutator. Now using  $\hat{a} = h\hat{D}$  and  $\hat{b} = h\hat{N}$  we see that the dominating error term in the approximation

$$\exp \left[ h \left( \hat{D} + \hat{N} \right) \right] \approx \exp \left( h\hat{D} \right) \exp \left( h\hat{N} \right) \quad (4.24)$$

arises from the commutator  $[h\hat{D}, h\hat{N}]$  and is thus proportional to  $h^2$ . By applying the B-H formula twice one can verify (after some algebra) that an even better approximation is given by

$$\exp \left[ h \left( \hat{D} + \hat{N} \right) \right] \approx \exp \left( \frac{h}{2} \hat{D} \right) \exp \left( h\hat{N} \right) \exp \left( \frac{h}{2} \hat{D} \right), \quad (4.25)$$

because then the dominant error term is proportional to  $h^3$ . The SSFM using equation 4.25 is sometimes called the symmetrized SSFM due to the symmetrical nature of the right hand side of the equation. The difference between the ordinary SSFM and the symmetrized one is that in the ordinary version nonlinear effects are taken into account between fiber segments of length  $h$  and in the symmetrized version the same is done in the middle of each segment [55].

Equation 4.20 gives  $\hat{N}A$ , but for computational purposes  $\hat{N}$  can be solved by simply dividing  $\hat{N}A$  by  $A$ . The convolution and the time-derivative in the resulting expression are easiest to calculate in the frequency domain and everything else is suitably done in the time domain. The operator  $\exp \left( \frac{h}{2} \hat{D} \right)$  is also trivial to calculate in the frequency domain where it is a mere complex number. The Matlab implementation of the symmetrized SSFM is then

---

relatively fast due to Matlab's excellent suitability for matrix and vector operations and its highly optimized fast Fourier transform (FFT) algorithm [94].

## Chapter 5

# Solitons and Other Solutions of the GNLSE

The GNLSE can only be solved analytically in some special cases, such as when it can be reduced to the ordinary nonlinear Schrödinger equation (NLSE) [57]. The NLSE is the GNLSE in the absence of losses, delayed nonlinearities (Raman effects), optical shock effects, and third- and higher-order dispersion:

$$\frac{\partial A}{\partial z} + i\frac{\beta_2}{2}\frac{\partial^2 A}{\partial T^2} = i\gamma|A|^2A. \quad (5.1)$$

It is evident that E. (5.1) is considerably simpler than Eq. (4.15). The NLSE, though here written for the envelope of the electric field propagating in a waveguide, also shows up in various different contexts besides nonlinear optics, such as Bose-Einstein condensates, water waves, and plasmas. Naturally the physical meaning of the equation's parameters are different depending on the context, but the mathematical form is the same. Because this equation describes a variety of physical processes, a great deal of effort has been put into developing methods to obtain analytical solutions to it. The

inverse scattering transform is among the most well known methods [95], but exact solutions can also be obtained for example by using Hirota's method [96], the truncated Painlevé expansion method [97], the tanh-method [98], and the more recent generally projective Riccati equation method, which is capable of constructing a multitude of families of solutions [99]. Although the NLSE does not always accurately describe broadband pulse propagation, its analytical solutions do exist in nature.

Arguably the most important analytical solution to the NLSE is the fundamental soliton. Without going into details of how to solve Eq. (5.1) from scratch, the soliton solution can be constructed by assuming a field envelope of the form  $A(z, T) = A_0 \operatorname{sech}(T/T_0) e^{i(bz+\varphi)}$  with real parameters and where  $A_0$  is positive (without loss of generality, as there is a phase factor of  $e^{i\varphi}$ ). Using this ansatz in Eq. 5.1 and multiplying each side by  $-iA_0^{-1} e^{-i(bz+\varphi)}$  yields

$$b \operatorname{sech} \left( \frac{T}{T_0} \right) + \frac{\beta_2}{2T_0^2} \left[ \operatorname{sech} \left( \frac{T}{T_0} \right) - 2 \operatorname{sech}^3 \left( \frac{T}{T_0} \right) \right] = \gamma A_0^2 \operatorname{sech} \left( \frac{T}{T_0} \right). \quad (5.2)$$

From Eq. 5.2 we can see that the parameters in the ansatz need to satisfy  $b = -\beta_2/(2T_0^2)$  and  $\gamma A_0^2 T_0^2 = -\beta_2$  in order for the ansatz to be a solution to Eq. (5.1). Two things can readily be inferred: the nonlinearity ( $\gamma$ ) and GVD ( $\beta_2 < 0$ ) need to have opposite signs for solitons to exist, and there is a relation between the amplitude  $A_0$  and the soliton duration  $T_0$ . The fundamental soliton therefore has only one free parameter, which can be

taken to be either the amplitude or the duration. Since seconds tend to be an easier concept to grasp than watts of optical power, it is generally the duration that is specified when discussing solitons [54, 57].

Solitons can be thought of as pulses for which SPM exactly cancels the effects of anomalous dispersion, and it is therefore easy to understand why they need to have a specific shape and why the peak power is connected to its duration. Temporally short solitons have a broad spectrum, and dispersion then has an easier time stretching and chirping the pulse in the time domain. To compensate for the more drastic dispersive effects, the nonlinearity-induced SPM needs to be stronger, which then requires the pulse to have a higher peak power. There are thus several requirements for solitons: the GVD parameter  $\beta_2$  needs to be constant across the spectrum, the nonlinearity  $\gamma$  must have the opposite sign compared to  $\beta_2$ , the soliton needs to have a specific functional form, and the peak power needs to have a certain value determined by the soliton's duration.

Because of all the different requirements for solitons, it is remarkable that they even exist in nature. What is even more remarkable, is that they are, in fact, very robust against all kinds of perturbations. If any of the relevant parameters  $\gamma$ ,  $\beta_2$ ,  $A_0$ , or  $T_0$  changes for whatever reason during the soliton's propagation, it can re-adjust its amplitude  $A_0$  and  $T_0$  such that the soliton condition  $\gamma A_0^2 T_0^2 = -\beta_2$  continues to be satisfied. A detailed argument for this was given by Menyuk [100], but for the sake of convincing the reader we will consider a simple example of a soliton suddenly losing some of its energy

in a fiber. First we note that the energy of a soliton (in our normalization) is given by  $2A_0^2T_0 = 2P_0T_0$ , where  $P_0 = A_0^2$  is the peak power. If the power  $P_0$  of a soliton abruptly decreases, the nonlinear effects will not be able to compensate for the dispersion anymore and  $|\gamma P_0 T_0^2| < |-\beta_2|$ . Dispersion then stretches the pulse and its peak power decreases further. The energy stays constant if there are no more losses present, but the pulse continues to stretch in time. Through stretching in time, the pulse can increase the product  $P_0 T_0^2$  while keeping the product  $P_0 T_0$ , or energy, constant. At some later stage the soliton condition  $\gamma P_0 T_0^2 = -\beta_2$  can then be fulfilled again. The pulse then has a chance to stabilize into a soliton of longer duration.

For most optical materials the nonlinear parameter  $\gamma > 0$ , which means that solitons require anomalous dispersion:  $\beta_2 < 0$ . The soliton condition can then be written as

$$N = \sqrt{\frac{\gamma P_0 T_0^2}{|\beta_2|}} = 1. \quad (5.3)$$

This unitless quantity  $N$  is closely related to the other analytical solutions of the NLSE, and as was seen above, the fundamental soliton has  $N = 1$ . Doubling the soliton order by suitably increasing the soliton's duration and/or peak power and using this as an input to the system described by the NLSE leads to a pulse that periodically (with respect to the distance  $z$ ) regains its original shape. The temporal and spectral profile of such a second-order soliton both oscillate with  $z$ . A third-order soliton with  $N = 3$  experiences similar periodic behavior with a different period and different

temporal and spectral profiles.

Whereas the fundamental soliton is robust against perturbations, higher-order solitons are highly unstable in the presence of Raman-scattering and optical shock effects, and even the inclusion of third-order dispersion can, depending on its magnitude, cause an  $N^{\text{th}}$  order soliton to break into  $N$  fundamental solitons [55]. This is called *soliton fission* and highlights the meaning of the soliton order  $N$ . Because of the instabilities, no higher-order solitons can be observed in optical fibers over long distances unless their propagation is described by the NLSE with only second-order dispersion and Kerr-effect present. Even in that case, solitons of sufficiently high orders tend to undergo soliton fission and break down to their constituents due to noisy input conditions. Figure 5.1 shows the evolution of a second-order soliton in the anomalously dispersive fiber of Fig. 4.2 modeled using (a) the GNLSE and (b) NLSE. The NLSE would predict incorrect behavior of the system and the respective figure shows the ideal periodic evolution of a second-order soliton.

In certain cases (i.e. for long pulses that are not too intense) the GNLSE can be reduced to the simpler NLSE equation while retaining the ability to accurately model the physics of pulse propagation [55]. Indeed, solitons of second and third orders were observed in the same experiment that was at the same time the first demonstration of the fundamental soliton in an optical fiber [32]. Thus, even if higher-order solitons are unstable, they are

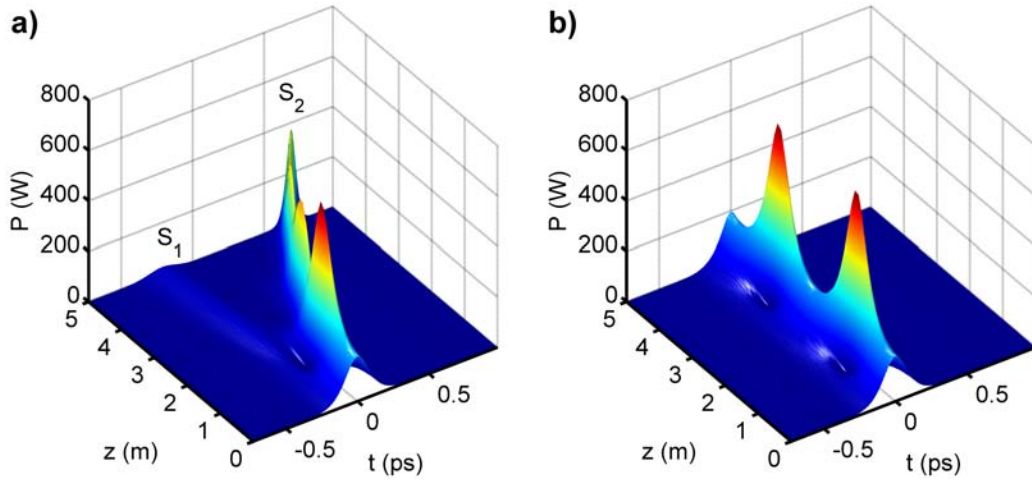


Figure 5.1: The evolution of a second-order soliton with slight input noise simulated using a) the GNSLE and b) the NLSE. The NLSE predicts incorrect, seemingly periodic behavior. In reality the pulse would break into two solitons as shown in a). The solitons are labeled  $S_1$  and  $S_2$ .

not mere mathematical curiosities but real phenomena that can occur in optical fibers. Fundamental and higher-order solitons are also not the only analytical solutions to the NLSE. The solutions discussed above all have the property of being sech-shaped at certain points during their evolution and evolving periodically with respect to propagation distance [101]. There are also solutions that are periodic in time but not in space [102], solutions that are periodic in both [57], and solutions that are periodic in neither time nor space [103]. These other types of more exotic analytical solutions of the NLSE have also been observed experimentally in optical fibers, among them dark solitons [104], Akhmediev breathers [105], the Peregrine soliton [106], and the Kuznetsov-Ma soliton [107]. Fiber optics is not the only platform where the NLSE is used to model a phenomenon, and soliton solutions can also be

demonstrated in other systems. In fact, the first documented experimental observation of a fundamental soliton was for a water wave in a Scottish canal in 1834 [108], and since then the Peregrine soliton as well as others have also been demonstrated in a water tank [109].

Although fundamental solitons are generally robust, they can and do change their parameters in the presence of perturbations. The different terms in the GNLSE [Eq. (4.15)] modify various aspects of solitons compared to the ideal solutions of the simpler NLSE [Eq. (5.1)]. Among the simplest perturbations is linear loss:  $\alpha > 0$  in Eq. (4.15). Loss causes the soliton to continuously readjust as it is losing energy, and such dissipative solitons have been extensively studied in various contexts. Another perturbation with somewhat intuitive consequences is third- and higher-order dispersion. Third-order and other odd-order dispersion terms distort the soliton shape asymmetrically [110] while the even-order dispersive terms contribute a symmetric change in their shape. Depending on their sign and relative magnitude, higher-order dispersive terms can also introduce a spectral region of normal dispersion where  $\beta_2 > 0$  and solitons cannot exist. This can lead to the emission of dispersive waves [111]. Dispersive wave emission is also called dispersive radiation, soliton radiation, and optical Cherenkov radiation, and it means the process in which a pulse emits a blue-shifted dispersive wave in the normal dispersion regime while adjusting itself to become a soliton.

Losses and dispersive effects are the linear effects that can affect the evolution dynamics of the soliton. The nonlinear effects also have interesting

consequences in the context of solitons. The Raman effect, as described by the delayed part of the response function  $R(T)$  in Eq. (4.15), leads to energy transfer from short wavelengths to longer ones. For solitons this means that the short-wavelength side (blue side) of its spectrum is losing energy while the long-wavelength side (red side) is gaining it upon propagation. The Raman effect therefore manifests as an effective red shift of the whole spectrum. This is the soliton self-frequency shift phenomenon [30]. The rate of the SSFS is proportional to  $1/T_0^4$  where  $T_0$  is the duration of the soliton, which means that SSFS becomes very efficient for short pulses and plays little role for very long pulses.

The optical shock effects are described by the time scale  $\tau_{\text{shock}} \approx 1/\omega_0$  in Eq. (4.15). Essentially they describe the frequency-dependence of the non-linear parameter  $\gamma$ . The main physical origin of this frequency-dependence is the dependency of the effective mode area on the wavelength. Assume, for simplicity, that the response function  $R(T)$  in the convolution integral of Eq. (4.15) only consists of the instantaneous delta function part related to the Kerr effect, and neglect everything except for the shock term in Eq. (4.15)

:

$$\frac{\partial A(z, T)}{\partial z} = -\gamma\tau_{\text{shock}} \frac{\partial}{\partial T} [A(z, T)|A(z, T)|^2] \quad (5.4)$$

It can easily be seen that (for  $\gamma\tau_{\text{shock}} > 0$ ) the shock term contributes an increase to  $|A|$  upon propagation in the parts where  $|A|$  decreases with respect to time. This means that the shock term causes the amplitude of a pulse

to increase in its trailing edge and decrease in its leading edge. This would eventually lead to the formation of an envelope that has an abrupt drop in amplitude with respect to time in its trailing edge, an optical shock wave [54].

## 5.1 Solitons in Fiber Amplifiers

None of the phenomena described above that affect soliton evolution dynamics have the ability to significantly enhance the nonlinear effects. Group velocity dispersion plays a role in determining the relation between a soliton's peak power and its duration and higher-order dispersion induces slight changes to the soliton spectrum and in the time domain. Optical shock effects distort the spectrum of an ideal soliton with some contribution to spectral broadening, whereas Raman scattering shifts the whole soliton spectrum continuously to longer wavelengths. While the red shift can be drastic, it generally does not broaden the spectrum. The effect of losses is to gradually decrease the total energy of the soliton, and if the soliton is able to keep up with this, its duration has to increase for it to remain a soliton. An increase in duration translates to a narrower spectrum for unchirped pulses such as solitons.

The fact that linear losses increase the duration and decrease the spectral extent of solitons begs the question: what would happen if the loss parameter  $\alpha$  were to flip its sign? An obvious answer would be that the solitons

must decrease in duration and grow in amplitude, which would naturally enhance nonlinearities. Negative loss naturally corresponds to gain, and gain can be realized in fibers through doping them with rare-earth metals and pumping them with suitable wavelengths [55]. The rare-earth metal required depends on the wavelength band of operation, with erbium being by far the most common due to its ability to provide gain around the 1.55  $\mu\text{m}$  telecom window [112, 113]. Solitons experiencing gain were first studied for their potential applications in communication systems. Dispersion and nonlinearities would cancel each other out in a soliton communication link, which means that fiber losses would then become the limiting factor for long-haul systems. Therefore, the solitons would need to be periodically amplified.

In the presence of gain, the soliton has to adjust to its increasing energy, which can change the dynamics more drastically than loss, especially if the gain is high. The early research on solitons in fiber amplifiers focused solely on potential applications in optical communication systems and most of the computational studies neglected possibly significant effects, such as Raman scattering and optical shock effects [114, 115, 116, 117, 118, 119]. However, Raman could be expected to play a major role in shaping the evolution dynamics of solitons in fiber amplifiers. This is because solitons that gain energy must decrease their duration and increase their peak power to remain solitons, and as their duration decreases, the Raman induced SSFS becomes more and more efficient. Following [3], this section consists of a thorough study on what happens to a soliton in an erbium-doped fiber am-

plifier (EDFA) using the full GNLSE including Raman gain and optical shock effects.

We consider a single EDFA and study the evolution of femtosecond pulses in it. The launched pulses have less energy than that required to form a soliton of the same duration. The amplifier then first amplifies the pulse into a soliton and even further, and multiple cascaded fundamental solitons are created at different distances within the amplifier. Each of them separates from the main input pulse because of SSFS that moves them outside the gain bandwidth of the amplifier. Multiple fundamental solitons can also form in passive fibers through modulation instability (long pulses) or soliton fission (short pulses), and both of these processes lead to simultaneous generation of solitons of different powers and durations [19]. The fiber amplifier allows for the generation of multiple cascaded solitons of nearly the same widths and peak powers, without requiring modulation instability or soliton fission.

To study the evolution of short optical pulses inside an EDFA, we rewrite the GNLSE of Eq. (4.15) in the frequency domain to account for the frequency-dependent amplifier gain. Equation (4.15) then takes the following form in the frequency domain:

$$\begin{aligned} \frac{\partial \tilde{A}}{\partial z} - i[\beta(\omega) - \beta(\omega_0) - \beta_1(\omega - \omega_0)]\tilde{A} \\ = \frac{g(\omega)}{2}\tilde{A} + i\gamma(\omega)\mathcal{F}\left\{A\int_{-\infty}^{+\infty}R(T')|A(z, T - T')|^2dT'\right\}(\omega), \end{aligned} \quad (5.5)$$

where  $\mathcal{F}$  is the Fourier transform operator,  $\tilde{A}(z, \omega) = \mathcal{F}\{A(z, t)\}$  is the

Fourier transform of the complex pulse envelope  $A(z, t)$ ,  $\beta(\omega)$  is the propagation constant of the optical mode,  $\beta_1 = d\beta/d\omega$  calculated at the carrier frequency  $\omega_0$  of the pulse, and  $T = t - \beta_1 z$  is the time measured in a frame moving with the input pulse group velocity. The nonlinear effects are included through the parameter  $\gamma(\omega)$  and a response function  $R(t) = (1 - f_R)\delta(t) + f_R h_R(t)$  that includes the Kerr nonlinearity through the Dirac delta function and Raman nonlinearity through the commonly used form of the Raman response function  $h_R(T)$  for silica with  $f_R = 0.18$  [54]. The frequency-dependent amplifier gain  $G(z, \omega) = e^{g(\omega)z}$  is taken to be nearly flat over the amplifier bandwidth  $\Omega$  and is included using a super-Gaussian profile:

$$G(\omega) = (G_0 - 1) \exp \left[ - \left( \frac{\omega - \omega_0}{\Omega/2} \right)^4 \right] + 1, \quad (5.6)$$

where  $G_0$  is the maximum gain of the amplifier. Losses have been neglected here since they are compensated for by the gain, but they could trivially be lumped together with the gain parameter.

Eq. (5.5) is solved numerically with the split-step Fourier method for a 20-m-long EDFA with its zero-dispersion wavelength at 1490 nm. Its gain spectrum is centered at 1550 nm ( $\lambda_0 = 2\pi c/\omega_0 = 1550$  nm) and it has a 40-nm gain bandwidth [ $\Omega/(2\pi) = 5$  THz], all typical values for EDFAs used in telecommunications. The dispersion parameters around the center frequency  $\omega_0$  are  $\beta_2 = -5.68$  ps<sup>2</sup>/km and  $\beta_3 = 0.13$  ps<sup>3</sup>/km at 1550 nm. The nonlinear parameter has the form  $\gamma(\omega) = \gamma_0 \omega/\omega_0$ , where  $\gamma_0 = \gamma(\omega_0) = 2$  W<sup>-1</sup>/km.

Note that  $\gamma$  is not constant across the whole spectrum and therefore has the optical shock effects incorporated into it. The amplitude of the input pulse has the form  $A(0, T) = \sqrt{P_0} \operatorname{sech}(T/T_0)$  with  $T_0 = 50$  fs (full width at half maximum 88 fs). Its peak power  $P_0$  is chosen such that the input soliton order is  $N = T_0 \sqrt{\gamma_0 P_0 / |\beta_2|} = 0.7$ , resulting in a peak power of 500 W. The peak gain  $G_0$  of the EDFA is specified in units of dB/m and is varied between 0 and 4 dB/m.

Figure 5.2 shows the temporal evolution of the 88 fs pulse over 20 m for  $G_0 = 1, 2,$  and 4 dB/m (normalized to the initial pulse amplitude). For  $G_0 = 1$  dB/m, the central part of the input pulse forms a fundamental soliton ( $N = 1$ ) after 3 m of propagation, and its spectrum begins to red-shift because of the SSFS [54], resulting in bending of the soliton trajectory owing to a reduction in its speed relative to the input pulse. The SSFS is efficient for the soliton because its width is a fraction of the input pulse width. Amplification of this soliton stops after its spectrum moves out of the amplifier bandwidth, but the pulse remnants at the original temporal location continue to be amplified as seen in Fig. 5.2(a). We even see the formation of a second soliton at a distance of about 15 m. Indeed, for a higher gain of  $G_0 = 2$  dB/m in Fig. 5.2(b) we observe multiple cascaded solitons form at different distances, and their trajectories bend toward the right because of SSFS. Each soliton also sheds some energy in the form of a dispersive wave (DW), as seen in Fig. 5.2(b). The situation becomes much more complex in Fig. 5.2(c) where the amplifier gain is increased to 4 dB/m.

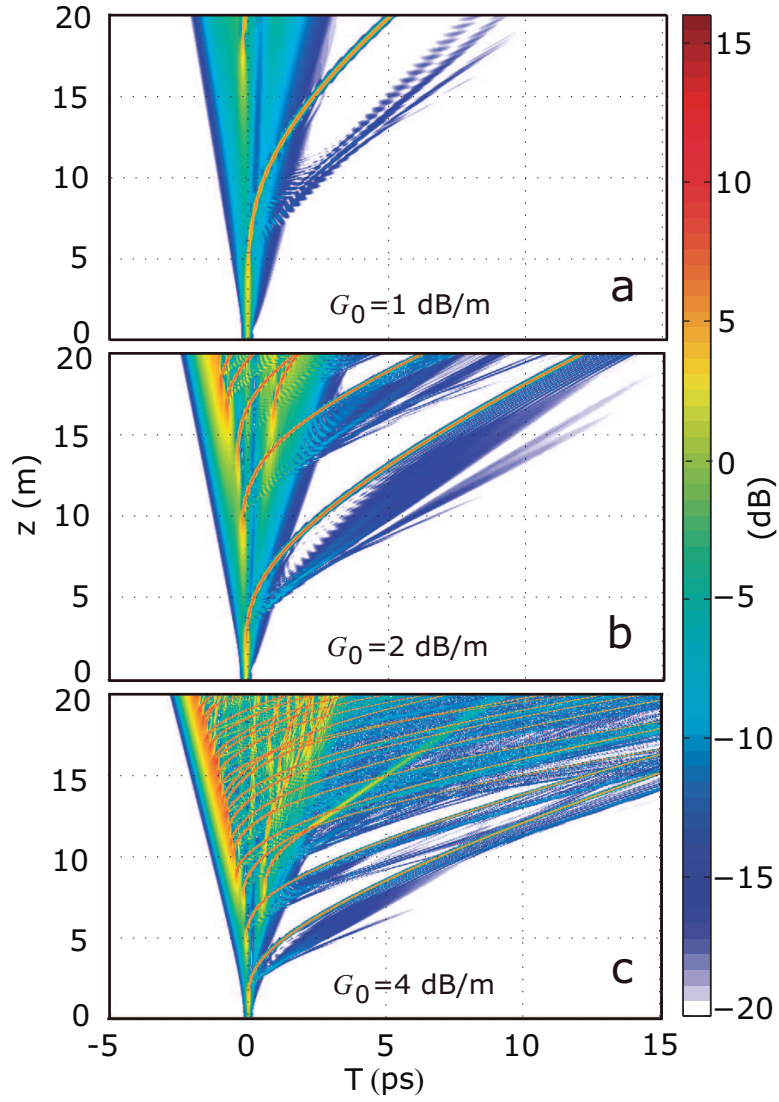


Figure 5.2: Temporal evolution of an 88 fs pulse over 20 m of active fiber for (a)  $G_0 = 1$ , (b) 2, and (c) 4 dB/m. Bent trajectories show cascaded red-shifted solitons forming at different propagation distances inside the fiber amplifier. After [3].

A large number of cascaded solitons emerge, together with their DWs that travel at different speeds and occasionally collide with the solitons.

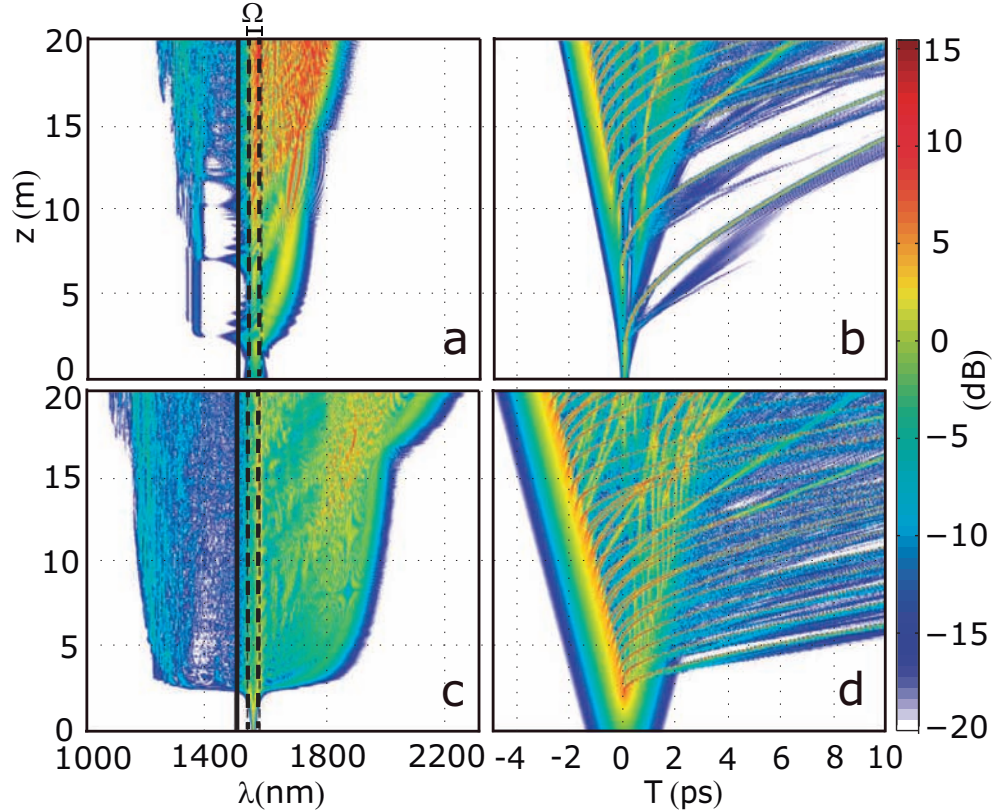


Figure 5.3: Spectral [(a) and (c)] and temporal [(b) and (d)] evolution under the conditions of Fig. 1 with  $G_0 = 3$  dB/m. The temporal FWHM is 88 fs in [(a) and (b)] and 880 fs in [(c) and (d)]. The ZDW of the fiber is marked by a black line, and the dashed lines show the gain band. The input soliton order is 0.7 for both cases. After [3].

One may wonder how the pulse spectrum evolves inside a fiber amplifier and how the input pulse duration affects the evolution. Figure 5.3 shows the spectral and temporal evolutions for two different input pulse durations for an amplifier with a gain of 3 dB/m. Figures 5.3(a) and 5.3(b) clearly show

the red-shifted spectral bands of the first two solitons formed at distances of approximately 2 and 6 m. Beyond that several solitons emerge in rapid succession so that their spectra overlap. At the amplifier output, a kind of SC is formed with two broad bands on each side of the input spectrum. The band on the red side belongs to multiple fundamental solitons, and the one on the blue side to the corresponding DWs. It is noteworthy that, unlike in conventional SC generation, the spectral broadening here is not based on soliton fission because the pulse energy never reaches the level that can support even a second-order soliton. Instead, the spectral broadening is solely due to SSFS, DW generation, soliton collisions, and interactions between DWs and solitons.

In the extreme, soliton interactions can lead to the generation of abnormally red-shifted rogue solitons [120, 121, 122]. Figs. 5.3(c) and 5.3(d) show signs of such a rogue wave being generated after 15 m of propagation. The rogue wave subsequently passes through a train of trailing edge solitons obeying optical Newton's cradle dynamics and gaining more energy from the weaker solitons [123]. The scattering of the previously generated DWs off the moving refractive index barriers associated with the intense rogue solitons then causes the DWs to blue-shift further, as seen after 17 m of propagation. Soliton-DW interactions can also affect the soliton trajectories and therefore mediate soliton collisions [124]. However, such collisions are less common here than in conventional SC generation, which might be beneficial in terms of coherence and control over the evolution dynamics.

The active fiber succeeds in inhibiting soliton collisions because all the leading edge solitons emerge from nearly identical surroundings but at different points in space and time. Because of SSFS, the solitons' group velocities are such that they help preserve the existing temporal gaps between them. Second, the solitons become surrounded by DWs on both sides, and the effect of one DW on the trajectory of a soliton will be at least partially negated by that of another DW on the other side of the soliton. These effects can be seen in Figs. 5.2 and 5.3 where we have numerous solitons with nearly parallel trajectories in a sea of DWs, and soliton collisions occur mostly between leading edge and trailing edge solitons.

It is clear from Figs. 5.2 and 5.3 that a single optical pulse propagating inside an optical amplifier can produce a cascade of ultrashort fundamental solitons, whose wavelengths are different at the amplifier output because each soliton forms at a different distance before experiencing the SSFS through intrapulse Raman scattering. The dynamics of these solitons exhibit rich behavior because of the simultaneous presence of a DW associated with each soliton and the possibility of collisions between two solitons or between a soliton and a DW. The number of solitons created can be controlled by varying the rate of amplification and the length over which pulse amplification occurs.

As an example, we study the case in which the optical gain exists only over the first few meters, i.e., an active section is followed by a passive fiber section. Figure 5.4 shows the temporal and spectral evolutions in two cases with  $G_0 = 3$  dB/m. The gain is turned off after 2.5 m in the top row but after

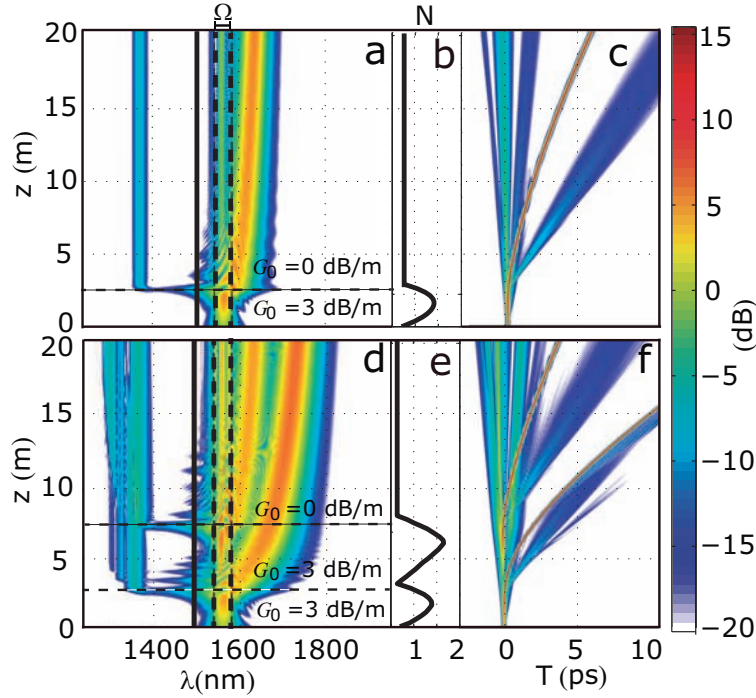


Figure 5.4: Spectral [(a) and (d)] and temporal [(c) and (f)] evolution when the fiber is active over 2.5 m (top row) and 7.5 m (bottom row). The ZDW of the fiber is marked by a black line, and the vertical dashed lines show the gain band. The soliton order  $N$  of the pulse remnants is shown in parts (b) and (e). After [3].

7 m in the bottom row. As seen in the figure, only a single soliton forms in the low-gain case. The soliton decelerates even in the passive section and moves slower compared to the pulse remnants because of the SSFS [57]. A DW also appears because of energy transfer from the soliton at a phase-matched frequency during the process of spectral shifting [see parts (a) and (c)]. Since both the DW and the soliton spectra are distinct from the spectrum of input pulse, we can approximately calculate the soliton order by fitting a hyperbolic

secant to the pulse remnants. The results are shown in Fig. 5.4(b), where we see that  $N$  exceeds 1 in the active section but drops to well below 1 in the passive section. In contrast, if the gain is kept on for a longer distance (parts d to f), the remnants continue to be amplified causing a second fundamental soliton to be generated at about 7.5 m, as seen in Figs. 5.4(d) and 5.4(f). The corresponding soliton order of the pulse remnants is shown in Fig. 5.4(e).

It should be clear by now that the number of fundamental solitons at the amplifier output depends heavily on the total gain  $G_0$  of the amplifier. Figure 5.5 shows the number of solitons formed at the end of a 20-meter-long fiber amplifier (no passive section) as a function of  $G_0$  for two different widths of the input pulse. The solitons were counted manually from the evolution traces such as the ones shown in Fig. 5.2. In order for a pulse to be counted as a soliton, it was required that the soliton had started to separate itself from its surroundings and that its spectrum had begun to red-shift. Hence, we interpret Fig. 5.2(a) as showing only one soliton, as the formation of the other soliton amidst the pump remnants is not quite complete yet. Figure 5.2(b) shows six solitons, all of which are clearly red-shifting and moving slower with respect to the background.

As expected, Fig. 5.5 shows that the number of solitons at the amplifier output increases with the total gain. For low gains ( $G_0 < 22$  dB), a low-energy input pulse forms a soliton within few meters as  $N$  approaches 1 and then retains its soliton nature by reshaping itself to become shorter to account for the lack of initial energy. This phenomenon of adiabatic soliton

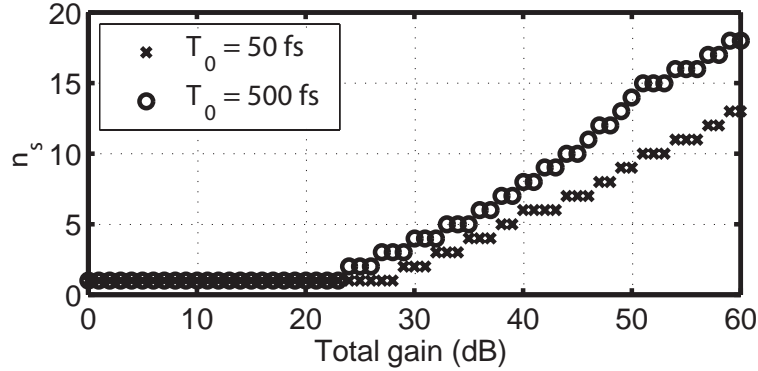


Figure 5.5: Number of fundamental solitons ( $n_s$ ) at the output of a 20-m-long amplifier as a function of total gain for two input pulses of different widths launched with  $N = 0.7$ . After [3].

compression is well known [114, 119]. It should be stressed that energy for the soliton comes mostly from the central region of the input pulse. After a certain gain threshold that depends on the input pulse duration, the gain is large enough to amplify and reshape the pulse remnants (mostly pulse wings) into another soliton, after the first soliton has moved away because of its slowing down through the SSFS. This process repeats, and  $G_0$  is increased even more solitons are formed. The leading portion of the input pulse accounts for the formation of most solitons (see Figs. 5.2 and 5.3). This is because the SSFS-induced deceleration causes each soliton to lag behind and overlap with the trailing portion. As the solitons slow down, they deplete the trailing edge through nonlinear interactions that transfer energy to the solitons. As a result, remaining pulse energy becomes heavily concentrated near the leading edge [see Figs. 5.3(b) and 5.3(d)].

Figure 5.5 shows that the number of solitons  $n_s$  at the amplifier output

also depends on the width of input pulses. For short pulses ( $T_0 = 50$  fs),  $n_s$  increases almost linearly with  $\ln(G_0)$ , or exponentially with  $G_0$ . This dependence becomes superlinear (or super-exponential) for wider pulses with  $T_0 = 500$  fs. One can understand this feature as follows. For wider pulses the energy is more spread in time. Therefore, it takes a longer distance for a soliton formed near the leading edge of the pulse to reach its trailing edge. If the gain is large enough, the trailing edge of the input pulse can have enough time to create a soliton before it is consumed by the decelerating soliton. By the time the soliton from the leading edge reaches the newly formed trailing-edge soliton, their frequency separation is too large for the two solitons to collide and interact nonlinearly. As a result, both solitons survive and separate from the input pulse. The solitons formed in the trailing region of the long input pulse are responsible for the superlinear behavior seen in Fig. 5.5. The solitons forming in the trailing edge start red-shifting and lagging behind, and during this process they gain energy from the non-solitonic trailing edge pulse remnants through the Raman effect. The trailing edge solitons have a group velocity closer to the pulse remnants and therefore nonlinear interactions between these solitons and the trailing edge pulse remnants take place over longer propagation distances, making the energy transfer to the solitons more efficient. As the trailing edge pulse remnants lose energy to the solitons, there is less energy left to form more solitons through gain, and the growth of the number of solitons with increasing total fiber gain saturates back to linear when the total gain is greater than 50 dB, as can be seen in

Fig. 5.5. The larger number of trailing edge solitons for longer pulses is also evident in the differences between the short pulse temporal evolution shown in Fig. 5.3(b) and the long pulse evolution shown in 5.3(d). Few trailing edge solitons can be seen in Fig. 5.3(b), whereas they are plentiful in 5.3(d) and many of them survive the collisions between leading edge solitons, as can be seen between the 5 m and 15 m marks in Fig. 5.3(d).

The total gain also affects the spectral extent of the output. To study the effect of gain on the output spectrum, we define the spectral range  $S_r$  as the difference between the largest and smallest frequencies for which the spectral power is 50 dB below the maximum value. Note that this definition allows for gaps in the spectrum and should not be thought of as the bandwidth of the output spectrum. Figure 5.6 shows how  $S_r$  at different distances of the active fiber depends on the total gain  $G_0$  for the same two different pulse durations used in Fig. 5.5.

One can identify several different regions in Fig. 5.6. The spectral range is below 20 THz in the blue region where the pulse evolves to form a fundamental soliton that slowly red-shifts through the SSFS. The transition to the teal/green region of Fig. 5.6(a) indicates the emission of a blue-shifted DW that increases  $S_r$  to nearly 50 THz (or 400 nm). For example for 60 dB total gain the DW is emitted around 2.5 m, as seen in Fig. 5.3(a). Hence there is an abrupt change in the spectral range around 2.5 m. When the gain is sufficient, the first soliton continues to be amplified before it leaves the gain window all the way up to the point where it needs to readjust by

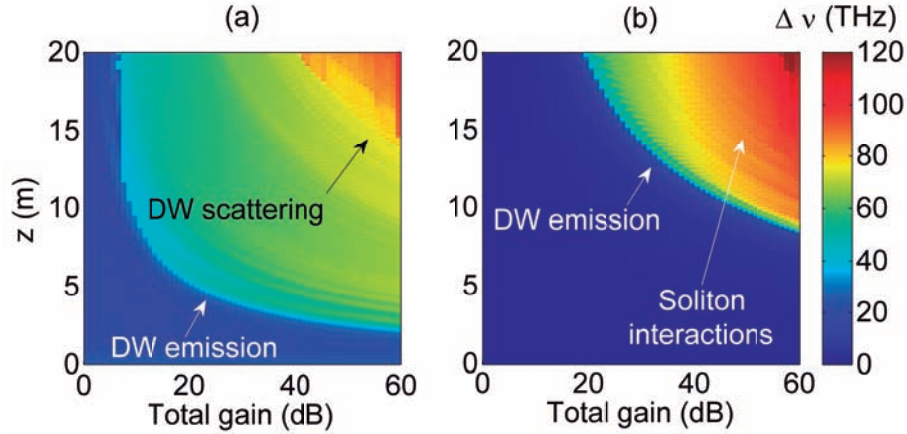


Figure 5.6: Spectral range (color coded) as a function of propagation distance and total gain for input pulses with (a)  $T_0 = 50$  and (b) 500 fs ( $N = 0.7$  in both cases). Different nonlinear processes responsible for spectral changes are indicated. After [3].

shedding off a DW. Further propagation gradually extends  $S_r$  because the SSFS increases the frequency separation between the DW and the soliton. Indeed,  $S_r$  is close to 70 THz in the yellow region in Fig. 5.6.

For the short-pulse case shown in part (a) a second smaller abrupt change occurs when the gain is high enough (red region for  $G_0 > 40$  dB). The physical reason for this change is related to reflection of a DW from the moving index boundary created by a decelerating soliton formed later. As is well known, such temporal reflections cause the DW to blue-shift further [125, 126] and eventually extend the spectral range to beyond 100 THz. This is also visible in Figs. 5.3(a) and 5.3(b) where a blue-shifted new DW component appears after 15 m. The same physical processes occur in the case of longer pulses shown in Fig. 5.6(b) with some differences. First, the increase in the spectral

extent is more gradual after the first DW generation. It can be attributed to interactions between two or more solitons and between a soliton and a DW, as can be seen in Figs. 5.3(c) and 5.3(d). Second, extension to the red side can also happen through the formation of an abnormally red-shifted soliton (an example of an optical rogue wave) because of in-phase collisions of solitons [120, 121, 122].

To conclude this section, the propagation of short optical pulses (width  $< 1$  ps) inside fiber amplifiers was investigated. The input pulses had less energy than what is required to form a soliton of equal duration. It was shown that the amplification leads to a cascade of independent fundamental solitons that appear at the amplifier output as temporally separated solitons of different wavelengths. The cascading process has its origin in the SSFS that red-shifts the spectrum of solitons while also slowing them down. The associated spectral broadening was attributed to soliton interactions and DW generation. The leading portion of the input pulse was shown to be responsible for the generation of the vast majority of solitons for ultrashort pulses but the trailing part was also found to generate solitons for wider input pulses. It was also found that the number of solitons at the fiber output depends not only on the total gain but also on the width of the input pulse. Even though the EDFA here had a 40-nm gain bandwidth, the results are more general and should apply to all fiber amplifiers, as long as the dispersion is anomalous within the gain bandwidth. The results are interesting from a fundamental perspective but they also point to a potential application. Tem-

porally separated pulses of different wavelengths are often required in practice for applications in areas such as optical coherence tomography (OCT) [127], spectroscopy [128], and multi-spectral imaging [129]. The results show that a fiber amplifier can be used to produce such pulses. Moreover, relative delays and wavelengths of different pulses are controllable through the length and gain of the amplifier and the width and peak power of the input pulse.

## Chapter 6

# Supercontinuum Generation

### 6.1 Overview

The broad spectra observed in the previous section in the context of solitons in fiber amplifiers are an example of a supercontinuum: a broad spectrum sculpted from a narrower input spectrum through optical nonlinearities. The discovery of supercontinuum is credited to Alfano and Shapiro [10, 11, 12] who observed spectral broadening spanning the visible range from 400 nm to 700 nm in a crystal. They explained their findings in terms of the third-order nonlinear optical processes of self-phase modulation and four-wave mixing. For the first few years since its discovery, only bulk materials were used to generate supercontinua and the application for it was Raman absorption spectroscopy [14].

Due to diffraction in bulk media, supercontinuum generation generally happens over a small spatial region at the focus of an intense laser beam. Waveguides allow for both tighter confinement of light as well as longer in-

teraction distances, and would therefore be ideal candidates for a SC platform. The first experiments of a waveguide based SC were done by Lin and Stolen in 1976 [13] who observed SC generation in an optical fiber pumped in the normal dispersion regime. The spectral broadening in waveguides was attributed to Raman scattering, SPM, XPM, and FWM [130, 131, 132]. Subsequent studies with pump wavelengths at 1310 nm and 1550 nm were able to recognize the major role of soliton propagation, SSFS [30], and the breakup of pulses through soliton fission [133, 134, 135, 136, 137, 138].

After the first demonstrations of supercontinuum generation around the 1550 nm range, it attracted considerable attention due to its potential applications in telecommunications and specifically in wavelength division multiplexing [15, 139, 140]. These studies were crucial in establishing a link between the input pulse wavelength and the dispersion profile of the fiber. After the invention of the photonic crystal fiber [17], an extreme example of the effects of fiber dispersion on SC dynamics was provided by Ranka *et al.* through an experimental demonstration of SC generation in this novel fiber [18].

Photonic crystal fibers allow for very widely tunable dispersion properties as well as high confinement of light due to their small cores and high refractive index contrast between the core area and the cladding, making them ideal for supercontinuum generation. Since the first demonstration, supercontinuum generation in photonic crystal fibers has been studied extensively [19]. Supercontinuum generation in fibers can be roughly divided into two

regimes: the long pulse regime and the short pulse regime, where the long pulse regime is understood to cover CW SC generation [85]. In the anomalous dispersion regime the corresponding evolution dynamics are initially dominated by soliton fission for short pulses and MI for longer pulses. The effect of MI is to break a longer pulse into a train of pulses that evolve into solitons. Soliton dynamics play an important role in both regimes because the generated fundamental solitons experience subsequent changes in their spectra and contribute significantly to the spectral broadening and other relevant SC characteristics

The short-pulse regime covers the situations where the input pulse duration is of the order of tens to hundreds of femtoseconds [19]. The actual distinction between the short- and long-pulse regimes depends also on fiber and laser parameters. When the input pulse spectrum lies mostly in the normal dispersion regime, the initial spectral broadening in the short-pulse regime is caused by SPM. In the anomalous dispersion regime the initial pulse roughly corresponds to a higher-order soliton, and were it only for GVD and SPM, a higher-order soliton would evolve in a periodic manner [57]. However, the perturbations in the form of shock effects, higher-order dispersion, and Raman scattering will cause the  $N^{\text{th}}$  order soliton to undergo soliton fission and break into  $N$  or fewer fundamental solitons (see figure 6.1). In practice, the amount of fundamental solitons created will only be equal to  $N$  if  $N$  is sufficiently small. Otherwise some of the energy of the initial pulse will be transferred to dispersive waves. The more energy the dispersive waves get,

the less there is left for solitons, and consequently fewer fundamental solitons will be formed.

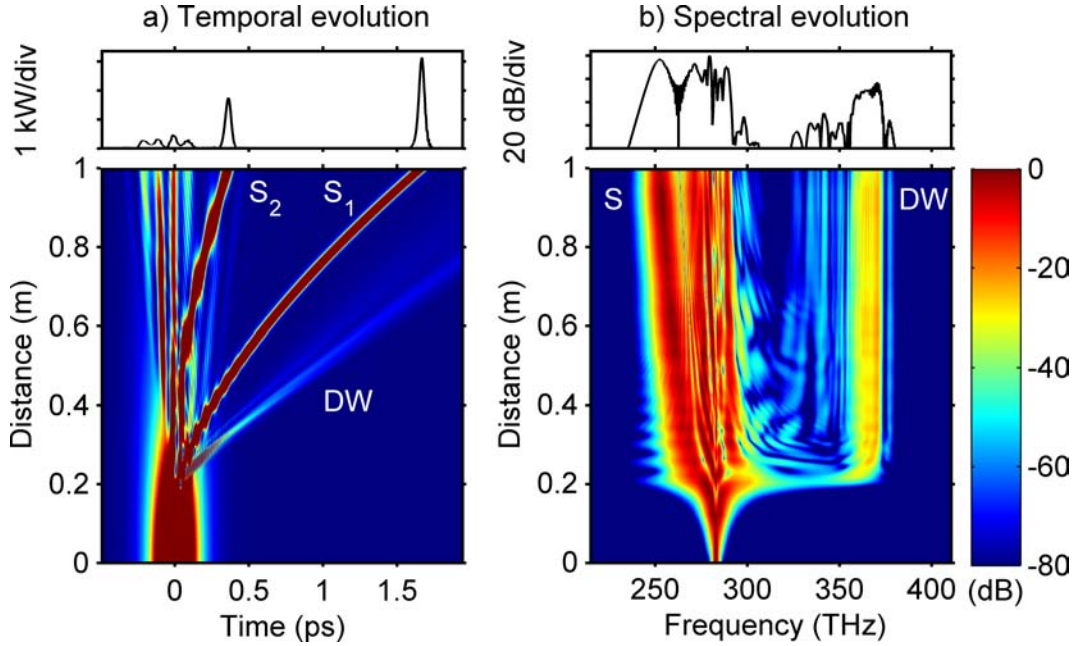


Figure 6.1: Temporal and spectral evolution of a 200 fs, 1.6 kW sech-pulse in a fiber with  $\gamma = 0.015 \text{ (m}\cdot\text{W)}^{-1}$ ,  $\beta_2 = -8.56 \text{ ps}^2/\text{km}$ ,  $\beta_3 = 6.87 \cdot 10^{-2} \text{ ps}^3/\text{km}$ , and  $\beta_4 = -9.29 \cdot 10^{-5} \text{ ps}^4/\text{km}$ . The figures in the left column are on linear scale and the color axis has been cut at 500 W for clarity. The spectral evolution is color coded in a logarithmic scale. The two brightest solitons have been labeled  $S_1$  and  $S_2$  in the temporal trace. The soliton and DW parts of the spectral trace have been labeled by S and DW, respectively.

Figure 6.1 shows the temporal and spectral evolution of a 200 fs sech-pulse of 1.6 kW peak power. The soliton order is approximately 6.0077. Note that most of the energy has been transferred to the two brightest solitons  $S_1$  and  $S_2$  after 70 centimeters of propagation. Four smaller peaks are clearly visible, but their solitonic nature is not as obvious. Besides soliton fission, also other

relevant phenomena can be seen in figure 6.1.

One of the most notable features is that the two most powerful solitons, especially the most intense one labeled  $S_1$ , have curved trajectories in the time domain. This means that upon propagation, the solitons start decelerating lagging more and more behind. It is caused by the combined effects of anomalous dispersion mentioned in section 3.4.1 and intrapulse Raman scattering in the form of SSFS mentioned in section 4.5. The brighter solitons have longer wavelengths than other remains of the initial pulse, which is why anomalous dispersion causes them to lag behind in the first place. SSFS causes the solitons to red-shift more, which in turn causes the solitons to decelerate. Hence the curved trajectory. Because solitons of higher peak power must have shorter durations and the rate of the SSFS is inversely proportional to the fourth power of the duration, higher peak power means more red-shift and more lag. The red-shift of the most intense soliton can also be seen in the spectral trace of figure 6.1.

Another feature that can be seen in both spectral and temporal traces is the emission of dispersive waves. The DW generated right after 20 cm of propagation is clearly visible, and the spectral trace shows it around 365 THz. It can be seen that the DW lags behind the most intense soliton although it should, according to the chromatic dispersion profile, move faster than the soliton. This is known as *soliton trapping*, and it can also occur for pairs of solitons, as was the case in the first experimental observation of the phenomenon [141]. The explanation is that the intense soliton causes

the DW to experience a higher refractive index due to XPM (see section 4.3), and it cannot move past the soliton. Because the DW and the soliton overlap temporally and propagate at similar velocities, they can interact and exchange energy with each other. Indeed, it has been shown [142, 143] that XPM and FWM can cause the DW to blue-shift and that the soliton experiences red-shift that is greater than what can be explained by the SSFS alone [125]. This cross-talk between a soliton and a DW can contribute significantly to the spectral broadening, and the usage of tapered fibers can enhance it even further [144].

The long-pulse regime refers to SC generation using pico- and nanosecond input pulses and CW lasers. Both in the anomalous and the normal dispersion regimes the initially dominating nonlinear process is FWM (see section 4.4). The pump beam provides amplification for those sidebands that satisfy the phase-matching condition to a certain degree.

Figure 6.2 shows the evolution of a SC generated using a picosecond input pulse, the central frequency of which lies in the anomalous GVD regime. The peak power is the same as in the short pulse case shown in figure 6.1, so the picosecond pulse has five times more energy than the 200 fs pulse. Yet the spectral broadening starts at a later stage (around 45 cm) and builds up slower than in the short pulse case. The spectrum at the fiber output is also flatter and broader.

The effect of MI can be clearly seen in both the temporal and spectral traces of figure 6.2. The first-order sidebands become visible after 40 cm

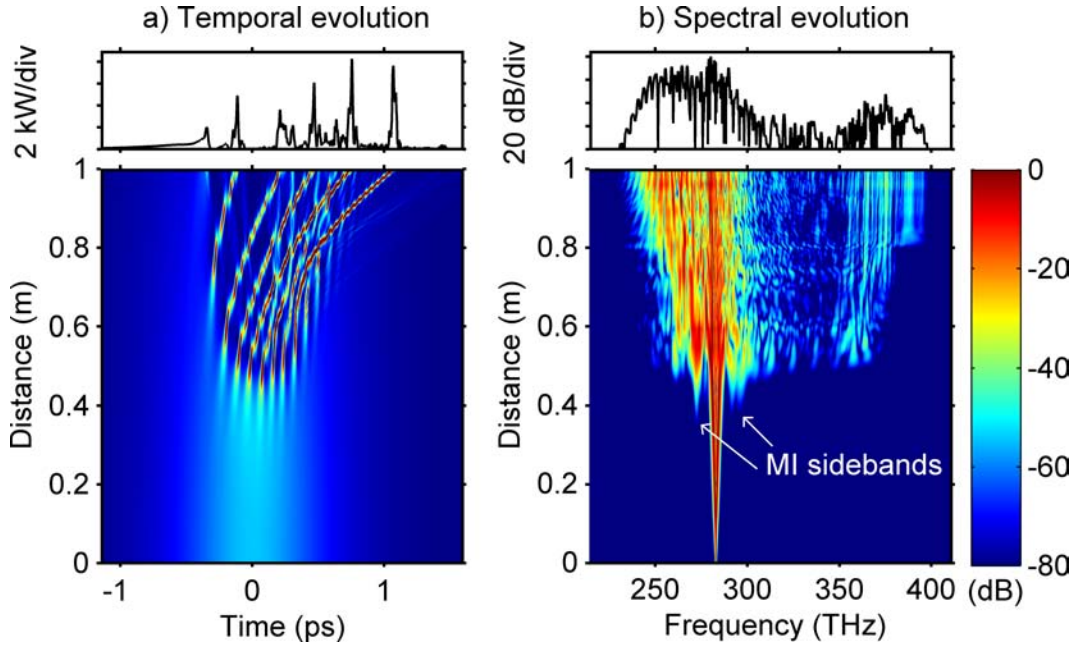


Figure 6.2: Temporal and spectral evolution of a 1 ps, 1.6 kW pulse. The left figures are on linear scale and the color axis has been cut at 5 kW for clarity. The spectral evolution is plotted using a logarithmic scale.

of propagation and the higher-order sidebands after 50 centimeters. The time domain manifestation of these sidebands can be seen as the sinusoidal modulation of the pulse. The modulation depends with the formation of additional sidebands and a train of pulses is formed. The pulses then start experiencing intrapulse Raman scattering and can form solitons, the curved trajectories of which can be seen in the temporal trace. After 60 centimeters of propagation, soliton dynamics start to play an increasingly important role in the evolution.

Because the initially dominating process for long-pulse regime SC generation is MI and the sidebands grow from noise, long-pulse regime SC could

be expected to be highly sensitive to the initial noise. The output spectra, such as the one in Fig. 6.2 would look very different, had the input noise been something else. The input noise in that simulation was nothing but quantum shot noise, which is the fundamental noise limit or the lowest possible noise possible - even in the ideal case. This noise cannot be controlled, which means that the output spectra would fluctuate considerably from one realization to another, simulated or done in the laboratory. The soliton fission process, on the other hand, is a lot more robust to input perturbation, as it is not induced by noise like MI. A vast range of important applications of supercontinuum require both high shot-to-shot stability and a wide spectrum. Due to the different nonlinear phenomena responsible for the spectral broadening, supercontinua generated with short pulses have superior stability properties, whereas longer pulses generally lead to wider and flatter spectra since it is easier to achieve higher energies with them. This leads to a tradeoff between stability and wide spectra.

## 6.2 Dual-Wavelength Pumping

It has been demonstrated [145] that there exists an optimal CW pump coherence to generate the widest SC spectra, meaning that total temporal coherence is undesirable in terms of spectral width. Incoherence translates to random variations in the amplitude and phase of the CW, creating peaks and valleys in the intensity. These peaks and valleys are clearly desirable,

but incoherence by definition means uncontrollable variations that propagate to the output in an unpredictable manner. To get the best of both worlds in terms of spectral width and stability in SC generation, it would seem beneficial if these peaks and valleys could be induced in a controllable manner, if a long pulse could be divided into shorter sub-pulses at will. Such a bundle of shorter pulses would surely have properties of a short pulse but also possibly retain some of the desirable properties of long pulses. A feasible means to achieve something like this would be to amplitude-modulate a long pulse at a desired modulation frequency. In the spectral domain such modulation would show as two sidebands on both sides of the main pulse or CW spectrum. As discussed in section 4.4, a long pulse or a CW in the anomalous dispersion regime can provide gain for sidebands leading to MI, the main mechanism responsible for SC generation in the long pulse regime. However, in the case of an amplitude-modulated signal, the MI process would be seeded as there would already be optical power within the gain bands. MI would then amplify a signal instead of noise, leading to more controlled SC generation. Such MI induced by amplitude modulation was suggested by Hasegawa in the 1980's and used to create a train of solitons [146].

As of 2018, the fastest amplitude modulators are based on hybrid plasmonics and cannot reach modulation frequencies beyond 100 GHz [147]. Furthermore, modulation depth becomes severely compromised above 50 GHz. The state-of-the-art modulators are even worse for other frequency ranges such as the 2  $\mu\text{m}$  range [148] that has been proposed as a promising candi-

date for next generation communication systems. A more versatile way to create modulated signals is to simply use dual-wavelength pumping, or dual pumping for short. Two CWs of different frequencies interfere destructively at certain points in time and constructively inbetween, leading to a beating intensity pattern. The relative amplitude and polarization of the two interfering CW beams determines the modulation depth, with equal amplitudes and same polarization leading to the largest modulation depth. Dual pumping in the anomalous dispersion regime has been studied both experimentally and theoretically [149, 150] and wide SC spectra have been demonstrated using this technique [151].

In the usual and most-studied cases the pump is in the anomalous dispersion regime and the other copropagating pump acts as a seed for MI leading to an enhancement of nonlinearities and hence wider SC spectra. However, pumping in the normal dispersion regime is known to lead to stabler supercontinua. We now demonstrate numerically dual pumping in the normal dispersion regime and show that this configuration is stable enough to produce frequency combs, which are essentially discrete supercontinua that are periodic in the time domain. Similarly, a signal that is periodic in the time domain always has a comb-like spectrum. The term comb is used loosely in the sense that we are interpreting a single spectral peak as a comb. Such a single-frequency spectrum belongs to a sinusoidal CW, which is obviously periodic.

Frequency combs are useful because they provide a means to measure op-

tical frequencies with electronic components by linking optical frequencies to microwave frequencies [152]. They have many applications in diverse technological areas such as precision metrology [153, 154], optical communications [155], and pulse-train generation [156]. Because any periodic signal is a comb in the frequency domain, a simple example of a frequency comb is given by a laser operating in pulsed mode. However, large separations of comb lines cannot be achieved utilizing only mode locked lasers, as the line separation is the inverse of the repetition rate which in turn is determined by the optical path length of the cavity. Such frequency combs then also lack tunability.

The train of solitons demonstrated by Hasegawa is an example of a time-periodic signal with a comb-like spectrum [146]. By tuning the modulation frequency, the repetition rate and hence the comb spacing could be changed at will. Chernikov et al. used two CW pumps at slightly different wavelengths in the anomalous-dispersion regime of optical fibers and generated a train of solitons with a 114 GHz repetition rate [157]. The same methods can also be employed in ring cavities with pulsed lasers [158] or CW [159], and ring cavities can generate pulse trains with repetition rates exceeding 500 GHz [160]. Microring resonators continue to attract considerable attention as frequency comb generators [161, 162] but other methods continue to be studied to achieve larger comb spacings for certain applications [163, 164, 165].

Though dual pumping in the anomalous regime is beneficial in terms of spectral broadening due to induced MI, the anomalous dispersion regime, the emerging pulses have a tendency to evolve into solitons. Slight deviations

from one soliton to another cause the solitons to have slightly different peak powers and hence different durations, and hence undergo SSFS at different rates [30]. The solitons will then eventually collide with one another in a phase-sensitive manner [120] and small variations devolve into a high degree of temporal incoherence leading to a supercontinuum instead of a frequency comb. This approach still works if the fiber is short enough or the powers low enough so that the periodic structure can be retained until the fiber output. Generation of pulse trains with repetition rates ranging from 1.5 THz to an impressive 3.4 THz have been demonstrated [166].

Solitons cannot exist in the normal dispersion regime in conventional silica fibers in which  $\gamma > 0$ . The spectral broadening in the normal dispersion regime is based on SPM and optical wave breaking [167] instead of noise-sensitive MI and soliton formation but nevertheless supercontinua can be and have been demonstrated in normally dispersive fibers [168, 169]. Optical wave breaking refers to FWM between the pulse's or CWs original frequency components and the components generated through SPM. As we will see, optical wave breaking plays an even more important role for a dual wavelength pump in the normal dispersion regime [170, 4]. Dual pumping with a zero-dispersion wavelength between the two pump frequencies has also been studied [171].

Since most applications of frequency combs do not require them to be a train of solitons in the time domain, anomalous dispersion has no clear advantage over normal dispersion other than possibly broader spectra. The

advantages of normal dispersion, however, are clear: increased robustness due to the absence of Raman shifting solitons and noise-sensitive modulation instability. Normal dispersion has also been shown to lead to better spectral flatness in SC generation [172]. In this section we demonstrate that dual pumping can be used in the normal dispersion regime of a PCF to generate tunable frequency combs with flat spectral properties and large frequency separations between the comb lines. Different values of the relevant parameters are considered through extensive numerical simulations and their effect on the output is determined. Raman effects are included, unlike in most previous studies [170], and we discuss the conditions under which Raman effects are important.

The GNLSE of Eq. (4.15) is solved numerically with a dual-wavelength input. The dispersion is curve shown in Fig. 6.3. Both pumps lie in the normal dispersion regime and the zero dispersion wavelength is 1133 nm.

Losses are ignored by setting  $\alpha = 0$ . The nonlinear parameter is  $\gamma = 15$  W/km and the shock time scale is  $\tau_s = 0.563$  fs, corresponding to  $1/\omega_0$  with  $\lambda_0 = 1060$  nm. The dual-pump input comes from two CW lasers, one at the frequency  $\nu_0 = c/\lambda_0$  with  $\lambda_0 = 1060$  nm, and another at a higher frequency  $\nu_0 + \nu_m$ . The corresponding input field can be written as

$$A(0, T) = \frac{\sqrt{P_0}}{\sqrt{1+x}} [1 + \sqrt{x} \exp(-2i\pi\nu_m T)], \quad (6.1)$$

where  $P_0$  is the total pump power and  $x$  is the ratio of the power at the

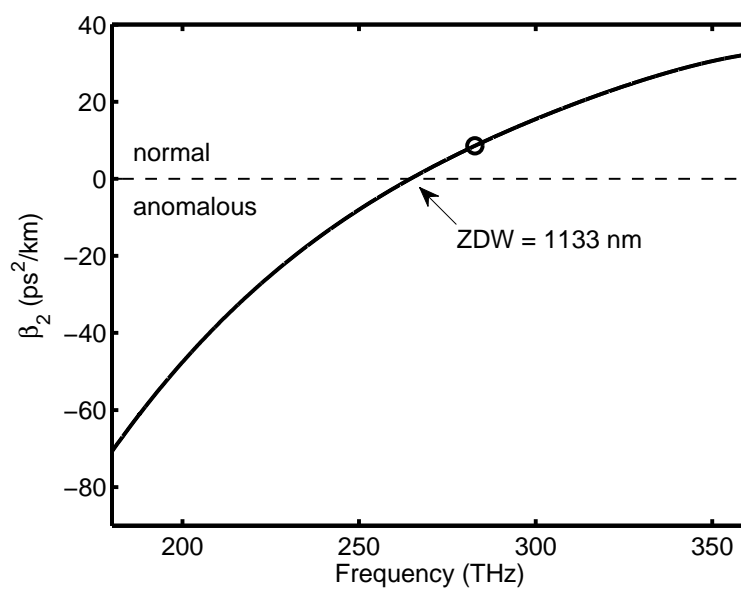


Figure 6.3: Group velocity dispersion  $\beta_2$  as a function of optical frequency. The circle denotes the lower frequency pump at 1060 nm. The zero-dispersion wavelength of the PCF is 1133 nm. After [4].

higher frequency CW pump to that of the lower frequency CW pump. In the simulations  $x$  is varied from 0 to 1,  $P_0$  from 1 W to 300 W, and  $\nu_m$  from 25 GHz to 1 THz. It should be noted that although the simulations have been done for CW initial conditions, the results are applicable to pulses longer than a nanosecond since the numerical time window is 40 ps wide. Experimental verification of the results will require such pulsed lasers to realize peak power levels near 100 W.

We first consider the case of two pumps 100 W each separated by 350 GHz ( $P_0 = 200$  W,  $x = 1$ , and  $\nu_m = 350$  GHz). Figure 6.4 shows the evolution of this dual-pump signal over a 5-meter PCF by showing the optical spectra and temporal profile at certain locations in the fiber chosen to highlight the importance of optical wave breaking (OWB) in the comb-formation process. Initially at  $z = 0$ , the spectrum consists of two spectral lines. In the time domain, we see a sinusoidal pattern resulting from beating of the two CW pumps. From Eq. (6.1), these sinusoidal power variations have the form

$$P(0, T) = |A(0, T)|^2 = P_0 \left[ 1 + \frac{2\sqrt{x}}{1+x} \cos(2\pi\nu_m T) \right]. \quad (6.2)$$

The modulation depth  $d_m = 2\sqrt{x}/(1+x)$  has its maximum value of 1 for  $x = 1$ , the case shown in Figure 6.4. We will see later that reduced values of  $d_m$  for  $x \neq 1$  affect the comb evolution significantly.

The crucial role of OWB in separating two regimes of evolution in the context of single-pulse supercontinuum generation in normally dispersive fiber

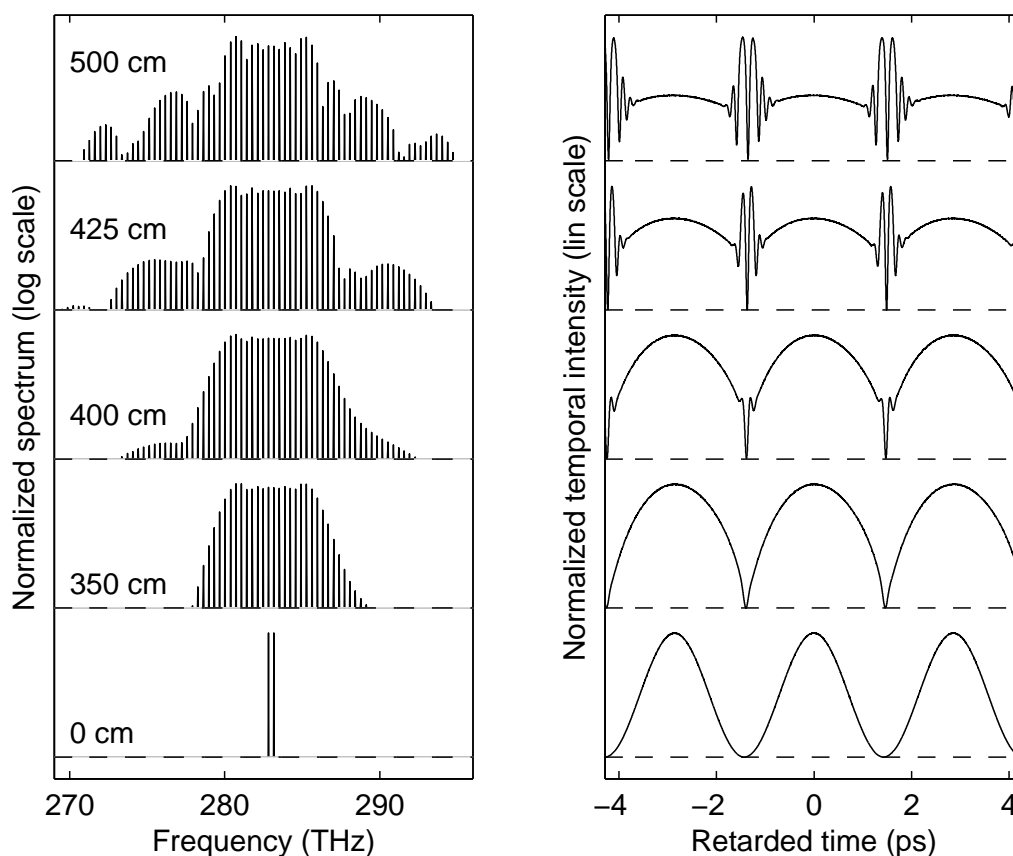


Figure 6.4: Spectral (left) and temporal (right) evolution of a dual-pump signal in the normal dispersion regime over 5 m of PCF. The spectrum scale is logarithmic over a 50-dB range. The dashed horizontal lines show the  $-50$  dB level for the spectra and the zero level for the temporal intensity plotted on a linear scale. Parameter values for the two CW pumps are  $P_0 = 200$  W,  $x = 1$ , and  $\nu_m = 350$  GHz. After [4].

was pointed out by Finot et al. [172]. More recently, Fatome et al. showed that a double shock is formed in the dual-pumping configuration at the initial modulation minima and that optical undular bores can be observed after such a double shock [170]. Similar double-shock formation can be seen in Figure 6.4. At a distance of 3.5 m, a frequency comb has been formed but its width is limited to about 10 THz. The temporal trace shows that the double shock has not yet occurred at 3.5 m but has taken place at a distance of 4 m, as evident by the sharp dips at the location of intensity minima. At a distance of 4.25 m, intense temporal peaks are formed at the shock positions because of the simultaneous presence of multiple frequency components. These components mix nonlinearly to produce new frequency components, and this four-wave mixing then manifests itself as the spectral side lobes that emerge after the double shock formation. As the spectrum before the shock formation is a comb, the emerging side lobes consist of discrete frequencies that contribute to the width of the comb. This can clearly be seen in figure 6.4 at a distance of 5 meters, where the frequency comb has a bandwidth of about 25 THz.

As the double-shock formation takes place at the initial modulation minima of the dual-pump signal, the initial modulation depth  $d_m$  could be expected to have an effect on the shock formation and on the resulting frequency comb. Figure 6.5 shows the evolution under conditions identical to that of Figure 6.4 except for unequal pump powers such that  $x = 0.1$  and  $d_m = 0.575$ . A direct comparison of the two figures shows the drastic impact on the comb

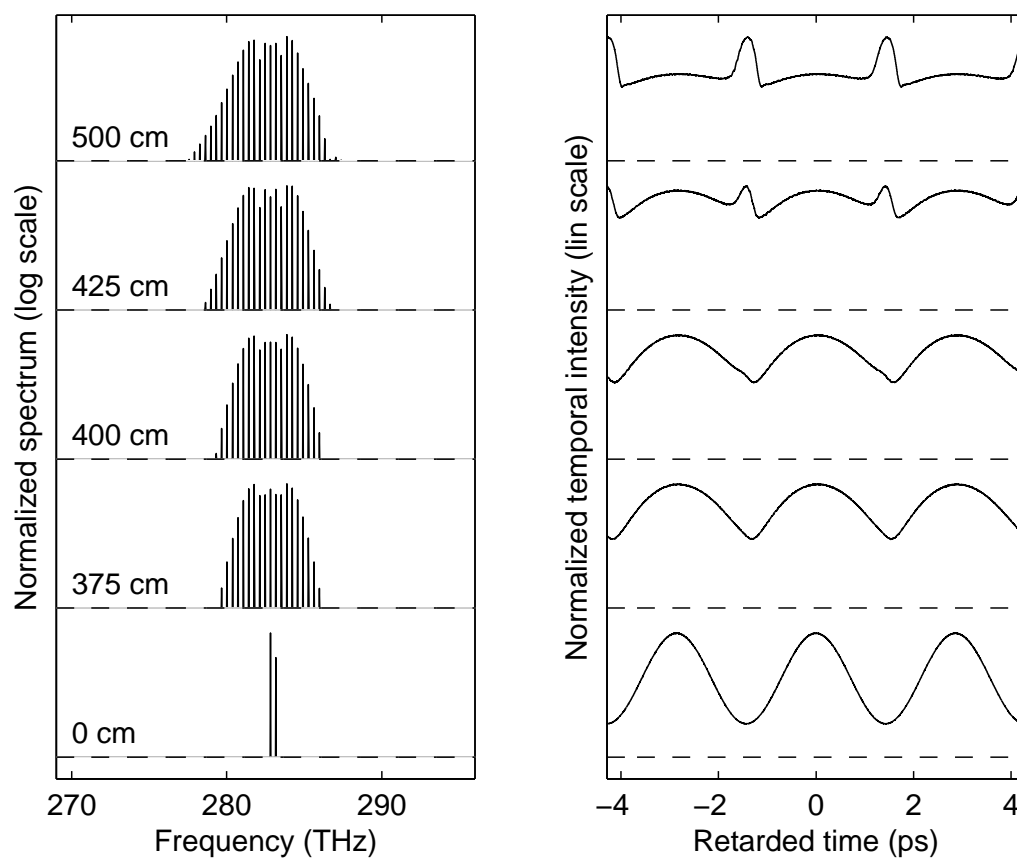


Figure 6.5: Same as figure 6.4 but for unequal pump powers such that  $x = 0.1$ . The total pump power is the same in both cases. After [4].

generation when the modulation depth is decreased even if the modulation remains very significant. A comb is still produced through SPM but its width is smaller by a factor of about 2. At a distance of 3.75 m, modulation depth is somewhat reduced in the time domain. For longer distances, OWB takes place, and the edges of adjacent pulses collide with one another. However, the temporal intensity slope of the colliding edges is smaller, which leads to both suppressed spectral broadening and smaller temporal peak powers for the forming intensity peaks. The resulting frequency comb at a distance of 5 meters is significantly narrower compared to the case of equal-power pumps shown in Figure 6.4. Clearly, deeper initial modulation helps create broader frequency combs.

Figures 6.4 and 6.5 both show more and more spectral broadening with increasing propagation distance. One may ask whether ultrawide frequency combs can be produced by simply increasing the PCF length. The answer is negative for several reasons. First, too long of a propagation distance will be detrimental because of the amplification of noise through four-wave mixing. Second, Raman scattering may begin to impact the quality of frequency combs. Third, fiber losses, although neglected here, could limit the performance for long fibers. To study how the comb width depends on various input parameters, a large number of numerical simulations was carried out. They were used to calculate the comb width defined as the bandwidth containing 99.98% of the total spectral power such that only 0.01% of the total power lies on each side of this frequency band. We also checked that

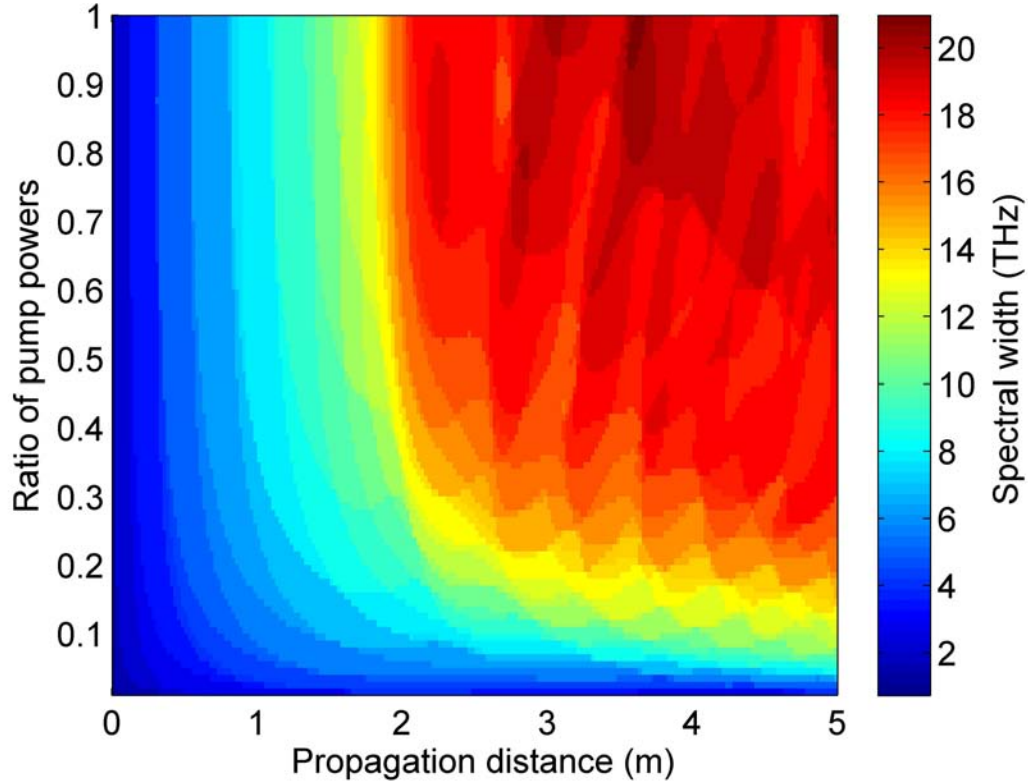


Figure 6.6: Comb bandwidth (color encoded) as a function of the ratio of pump powers and propagation distance. The input parameters are  $P_0 = 200$  W and  $\nu_m = 700$  GHz. After [4].

the spectra can indeed be considered frequency combs and were not ordinary supercontinua by verifying that at least 99.99% of the total spectral power was concentrated at the discrete comb frequencies.

Figure 6.6 shows the numerically calculated comb bandwidth as a function of propagation distance and pump-power ratio  $x$  using  $P_0 = 200$  W and  $\nu_m = 700$  GHz. For a given value of  $x$ , spectral broadening starts immediately and is fairly linear up to a certain distance, after which intense broadening

occurs over a short distance. The initial linear broadening is consistent with SPM-induced spectral broadening [54], and the abrupt sudden broadening can be explained in terms of OWB. The features seen in the figure also bear considerable resemblance to the observations on spectral broadening of a single pulsed pump in Ref. [172] in which abrupt spectral broadening was also explained in terms of OWB. In the case studied here, the ratio of the pump powers plays a role analogous to that of the peak power of the pulse.

The total pump power is known to have a significant effect on supercontinuum generation, where it sets the order of soliton for pulses propagating in the anomalous dispersion regime of an optical fiber. We thus expect the total pump power  $P_0$  to influence frequency comb generation in the normal dispersion regime of the PCF. In the case of a single pulse, it is customary to characterize the relative importance of dispersion and nonlinearity through the use of the dispersion length  $L_D = T_0^2/|\beta_2|$  and the nonlinear length  $L_{NL} = 1/(\gamma P_0)$ , where  $T_0$  is a measure of pulse duration and  $P_0$  is the pulse's peak power. In the dual-pumping configuration here, the total pump power  $P_0$  and the period of sinusoidal modulations,  $T_0 = 1/\nu_m$  play the role of the corresponding two parameters. For the input parameters used in Figures 2–4, the nonlinear length is always smaller than the dispersion length, usually by orders of magnitude. Thus, the nonlinear effects dominate over the dispersive effects, similar to the case of supercontinuum generation. Furthermore, for a dual-pump input signal one might expect dispersion to be less of an issue than for a single pulse, as every frequency component of the

electric field is present in every time slot that has a duration of the input period, and the average power over a period stays almost constant throughout propagation. One might then expect that nonlinear power transfer between different frequencies can continue occurring throughout the evolution of a dual-pump signal. Thus, instead of exploring the evolution dynamics as a function of propagation distance in meters, it is more intuitive to normalize the distance as  $\xi = z/L_{NL}$  using the nonlinear length.

Figure 6.7 shows the comb bandwidth as a function of  $\xi$  and pump power  $P_0$ . The comb width increases quite monotonically with respect to both of these parameters. What is noteworthy is that, although to achieve a specific comb width a certain power level is required, low initial powers cannot be compensated for by making the fiber longer. Furthermore, for low pump powers and longer propagation distances Raman scattering is able to transfer a significant portion of the initial power at the pump frequencies to a continuum at lower frequencies. Since low input powers create narrow combs, higher-order dispersion plays no role in the comb formation, and other than the Raman-induced power transfer, the evolution of a low-power dual-pump signal is very similar to that observed in Ref. [150].

Not all nonlinear power-transfer mechanisms contribute to the formation of a frequency comb. Spontaneous Raman scattering is responsible for transferring power from the pump frequencies to a broader band of lower frequencies [54]. Such a transfer of power is obviously detrimental in the context of frequency comb generation. The emergence of a continuum decreases the

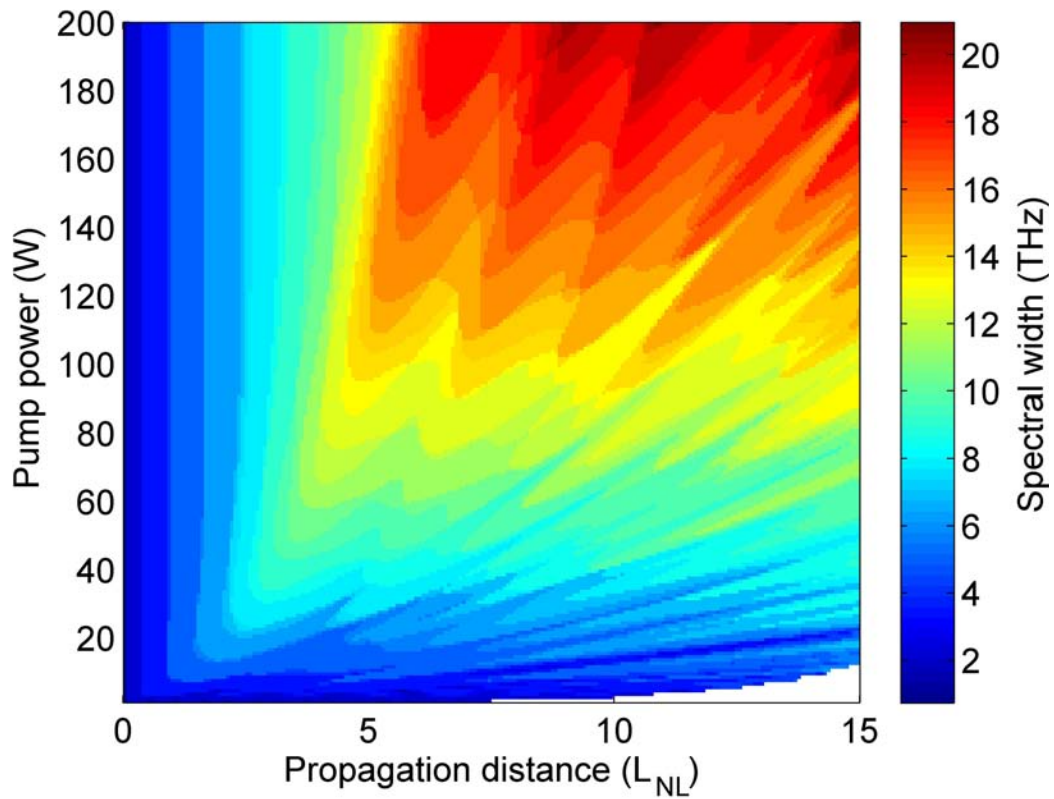


Figure 6.7: Comb bandwidth (color encoded) as a function of total pump power and propagation distance. The input parameters are  $x = 1$  and  $\nu_m = 700$  GHz. Spectra that did not qualify as frequency combs have been left out (lower right corner). After [4].

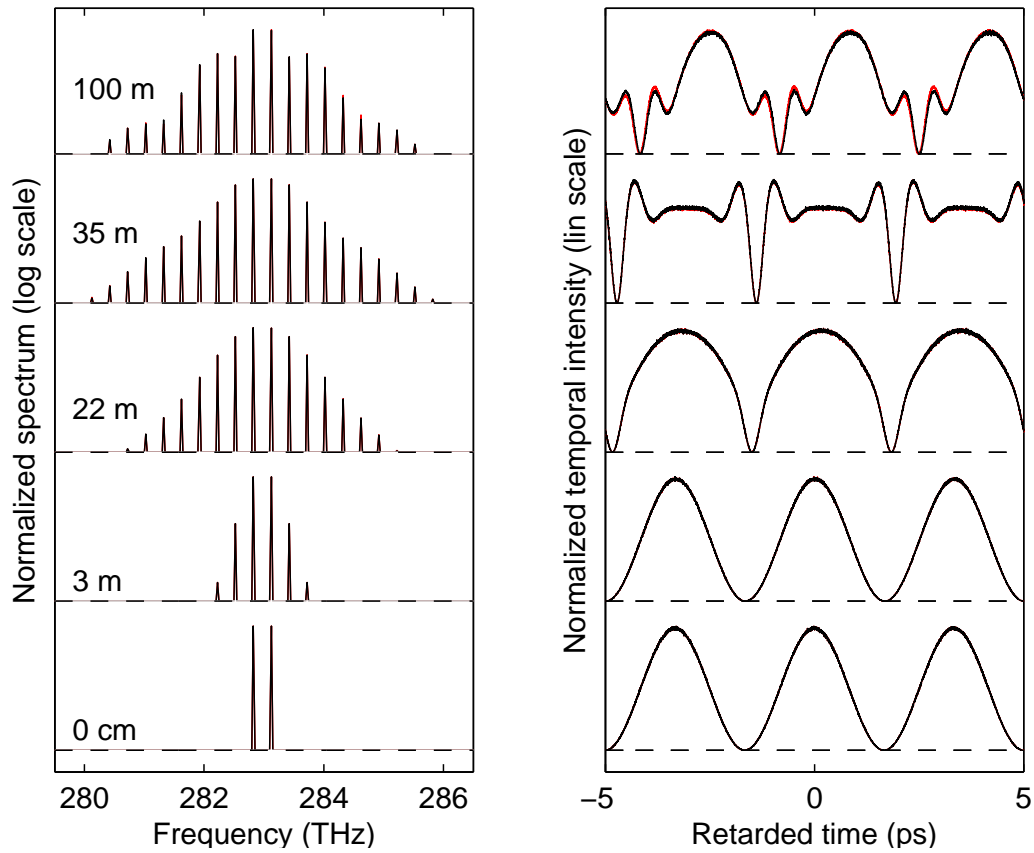


Figure 6.8: Evolution of a dual-pump signal over 100 m meters with (black lines) and without (red lines) including the Raman effect. Pump parameters are  $P_0 = 5$  W,  $x = 1$ , and  $\nu_m = 300$  GHz. The scale for spectra is logarithmic ranging from  $-60$  to  $0$  dB. The effect of Raman scattering is negligible in this case. After [4].

contrast between the comb and the background. Furthermore, because power is being transferred away from the pump frequencies, the strength of beneficial nonlinear effects decreases as well. Thus, Raman scattering could be detrimental even when the comb spectrum is narrow enough such that the peak of the Raman gain lies outside of the comb bandwidth.

To study the effect of Raman scattering on the comb formation, we performed simulations with the Raman contribution turned off by setting  $R(T') = \delta(T')$  in Eq. 4.15. Figure 6.8 shows the evolution of a 5 W dual-pump signal over 100 meters both with (black) and without (red) the Raman effect. It is obvious that the effect of Raman scattering is negligible for this specific set of pump parameters. In numerical simulations, a Raman peak was observed when the Raman effect was included, but its spectral power was below  $-70$  dB at 13.2 THz below the lower pump frequency. Similar behavior was observed for many other pump powers and frequency separations. Only when the total pump power exceeded 200 W, Raman scattering played a slightly more significant role. As an example, Figure 6.9 shows evolution over 5 m of PCF using the parameter values  $P_0 = 200$  W,  $x = 1$ , and  $\nu_m = 700$  GHz.

In this case, the maximum comb width is reached at a propagation distance of 2.5 meters, and before that the effect of Raman scattering on the spectral and temporal evolution is almost completely negligible. For larger propagation distances, the spectra and the temporal intensity profiles start to differ more. In particular, the comb spectrum becomes asymmetric with slightly more power at red-shifted frequencies. This is expected since high-frequency components pump the low-frequency components through stimulated Raman scattering.

The comb spectrum after 5 meters of propagation also appears slightly broader when Raman scattering is included. However, it should be kept in

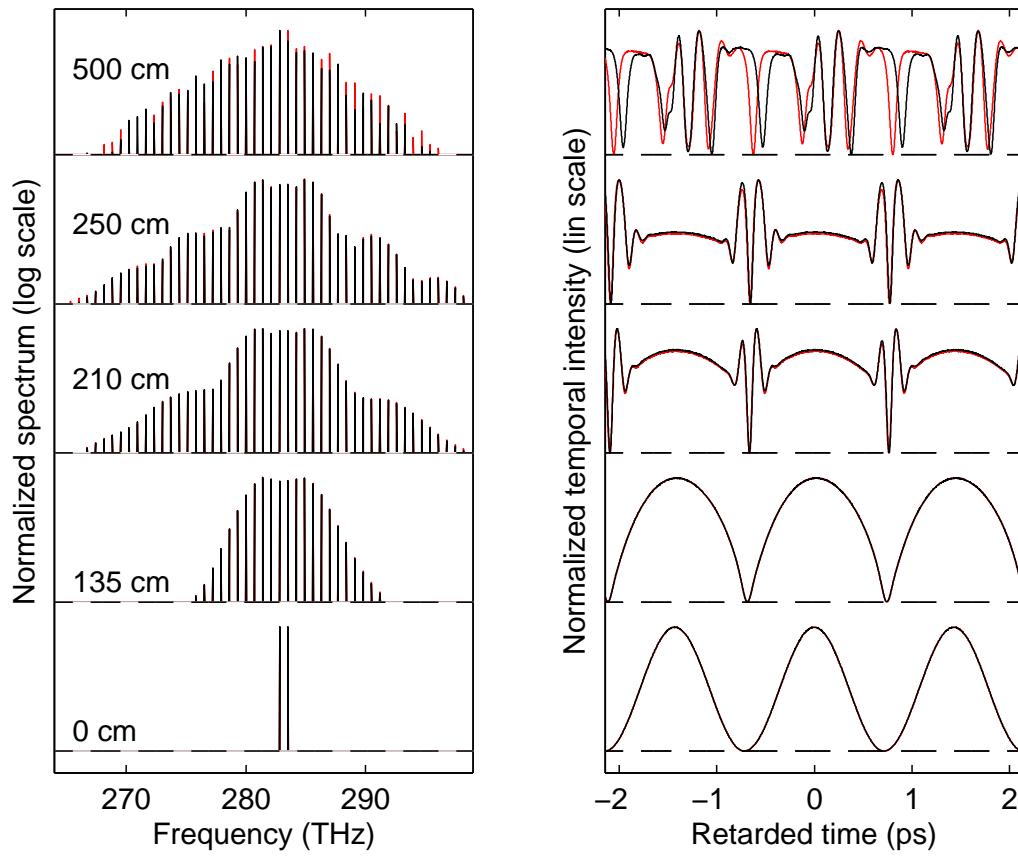


Figure 6.9: Same as figure 6.8 but with  $P_0 = 200$  W,  $x = 1$ , and  $\nu_m = 700$  GHz. After [4].

mind that the spectra are normalized. The apparent broadening is due to a Raman-induced power transfer from the pump frequencies and nearby sidebands to a continuum of frequencies. Even though the Raman-amplified band stays well below the  $-70$  dB level compared to the pump frequencies, this power transfer is enough to lower the central frequency peaks with respect to the peaks at the comb edge thus making the normalized spectrum appear wider. By examining the unnormalized spectra, we found that the spectrum was actually broader when Raman scattering was not included. We thus conclude that in the dual-pumping configuration in the normal dispersion regime of a fiber the effect of Raman scattering is either negligible or slightly detrimental. This is a noteworthy difference between comb generation and supercontinuum generation. In the context of supercontinuum generation in normally dispersive fiber, Raman scattering is an important physical phenomenon that helps extend the continuum towards lower frequencies. In comb generation, however, Raman scattering does not contribute to the comb width even when the Raman gain band overlaps with the comb.

Numerical simulations showed that tunable frequency combs can be generated by launching two CW pumps at slightly different wavelengths into a normally dispersive optical fiber. The dual-pump configuration produces a periodic sinusoidal modulation and allows tuning of the comb spacing from tens of gigahertz into the terahertz regime. The presented results show that the relative powers of the two pumps play a critical role, and widest frequency combs form when the two pumps are launched with the same power. The

reason behind this is related to the phenomenon of optical wave breaking known to occur in the case of normal dispersion.

In order to quantify the usefulness of the proposed scheme, we studied the dependence of the comb bandwidth on several important input parameters such as the total power, relative powers, and frequency separation of the two pumps and the length of the fiber employed. The depth of sinusoidal modulation produced by beating of the two pumps was shown to have a crucial effect on comb width, with deeper modulation enabling broader combs. This was interpreted and explained through the crucial role of optical wave breaking in SPM-induced spectral broadening. Unlike the case of supercontinuum generation, Raman scattering was found to have a negligible or even a slightly detrimental effect on comb generation. This is in sharp contrast to the case of supercontinuum generation where Raman scattering plays an essential role. In addition to explaining the relative importance of different physical phenomena on frequency comb generation, the findings also create a link between work done on the propagation of a single pulse and the evolution of dual-pump signals in the normal dispersion regime of highly nonlinear fibers.

## Chapter 7

# Dual Pumping in Dispersion-Decreasing Fibers

The dispersion of a PCF can be made to change along its length either during the manufacturing process or by tapering it afterwards. SC generation has been studied in both kinds of dispersion-varying fibers [173]. Typically the fiber is pumped in the anomalous-dispersion regime, and the magnitude of the dispersion parameter  $\beta_2$ , defined as  $\beta_2 = d^2\beta/d\omega^2$  where  $\beta(\omega)$  is the modal propagation constant at frequency  $\omega$ , is made to decrease along fiber's length. Such fibers are referred to as dispersion-decreasing fibers (DDFs). The beneficial effect of decreasing  $|\beta_2|$  on the spectral width of an optical pulse is evident in the context of solitons, as decreasing  $|\beta_2|$  causes them to compress temporally, which broadens their spectrum and also causes them to red-shift faster through the Raman effect [30, 54]. In practice, tapering a fiber will also decrease its core size leading to broader SC spectra simply due to enhanced nonlinearities [173, 174].

Noise-seeded modulation instability leads to incoherent supercontinua

[175] but a modulated input in the long pulse regime results in better coherence properties [176]. SC and frequency comb generation using dual-wavelength pumping has been explored in numerous studies [177, 178, 151, 179, 4, 180]. The dual-pump configuration can have significant advantages over single-CW pumping. Demircan et al. [181] considered two pulses on opposite sides of the zero-dispersion wavelength. The solitonic input pulse created a moving temporal refractive-index barrier for the other pulse propagating in the normal dispersion regime. The other pulse then scattered off this barrier and created new spectral components in a quasi-continuous manner, leading to a very broad and relatively flat SC spectrum.

Following [5], in this section we explain the origin of the blue components during SC generation in DDFs. This explains previous experimental results on enhanced blue side spectral broadening [173] as well as our recent observations about longitudinally varying dispersion being beneficial for dual-pump SC generation but detrimental for a single CW pump [182]. The origin of the blue components then brings us to an important result: a connection between dispersive wave emission and the more general phenomenon of temporal reflection [126]. Dual pumping creates an amplitude-modulated input signal, which evolves nonlinearly into a train of fundamental solitons that are then compressed temporally by decreasing  $|\beta_2|$ . While adiabatic soliton compression due to varying dispersion extends the spectrum to the red side, here we show that the blue side of the spectrum is also significantly affected through multiple reflections of the pump remnants at the soliton-induced

index barriers. In previous studies, scattering of DW's off solitons led to spectral broadening only under carefully crafted input conditions [181, 183]. In contrast, the approach presented here allows temporal reflections to occur spontaneously, with little sensitivity to the input conditions. Furthermore, the periodic nature of the emerging soliton train effectively creates temporal waveguides for the blue frequency components, and the waves can keep reflecting and remain partially trapped between two adjacent solitons. This wave-trapping phenomenon continues to be a topic of contemporary research [184].

Again, we use Eq. (4.15) to model the propagation of the dual pump input. For a DDF, in general, all dispersion parameters  $\beta_n$  are functions of  $z$ . Here the higher-order dispersive terms as well as the nonlinearity are kept constant while  $\beta_2$  changes linearly with  $z$ . Equation (4.15) is solved numerically using the split-step Fourier method [54].

The input consists of two CW's of equal power and different frequencies centered around  $\nu_0 = \omega_0/(2\pi) = c_0/\lambda_0$ , where  $c_0$  is the vacuum speed of light and  $\lambda_0 = 1.06 \mu\text{m}$ . Quantum shot-noise is also included by adding one photon with random phase per mode [19]. The frequency separation  $\Delta\nu$  between the two pumps is varied from 25 GHz to 1 THz. The nonlinear parameter is  $\gamma = 91.6 \text{ (W km)}^{-1}$  at the center frequency  $\omega_0$ .  $\beta_2$  at  $\omega_0$  increases linearly from  $-8.56$  to  $5 \text{ ps}^2/\text{km}$  over the 150 m length of the fiber. The dispersion curve at the fiber's input end is shown in Fig. 7.1.

The nonlinear response function,  $R(t) = 0.82\delta(t) + 0.18h_{\text{R}}(t)$ , includes

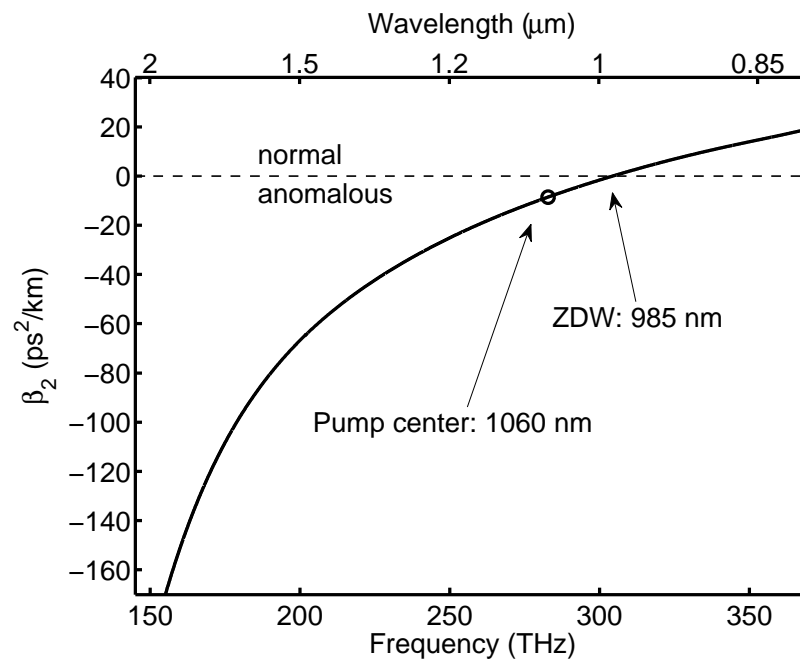


Figure 7.1: Dispersion parameter  $\beta_2$  at the input end of the fiber. The circle denotes  $\nu_0$ . The zero-dispersion wavelength of the PCF is 985 nm. After [5].

both the delayed Raman response  $h_R$  and the instantaneous [54] Kerr-type electronic response. The convolution integral on the right-hand side of Eq. (4.15) is done in the frequency domain where the Raman contribution is modeled through the full experimental Raman spectrum of silica [91]. Self-steepening is governed by the shock time scale  $\tau_s = 0.563$  fs. The fiber lengths considered were 150 meters or less, and since losses for PCF's of such lengths can be less than 0.15 dB [185], they were ignored for simplicity by setting  $\alpha = 0$ .

Figure 7.2 shows the temporal and spectral evolution of a dual-pump input inside a DDF (frequency separation  $\Delta\nu = 400$  GHz). The total input power of 1 W corresponds to a peak power of only 2 W at the location of each temporal peak. The input acts as a train of cosine-shaped pulses with a full width at half-maximum of 1.25 ps. During the first 20 meters, the pulses compress temporally as they undergo self-phase modulation (SPM). The central peak of each individual pulse then starts adjusting to become a fundamental soliton. During these stages the spectrum is still comb-like.

Once solitons are formed, SSFS starts red-shifting them. Moreover, the red-shift is accelerated compared to a fiber with constant dispersion due to a decrease in  $|\beta_2|$  along the fiber length. This is because of soliton compression making the solitons more intense and shorter in time. The rate of SSFS scales inversely with the fourth power of soliton duration [54] and thus the red-shift becomes greatly enhanced. Since the input power is too low for modulation instability to amplify the shot noise to observable levels, the first stages of signal evolution are governed solely by the SPM phenomenon.

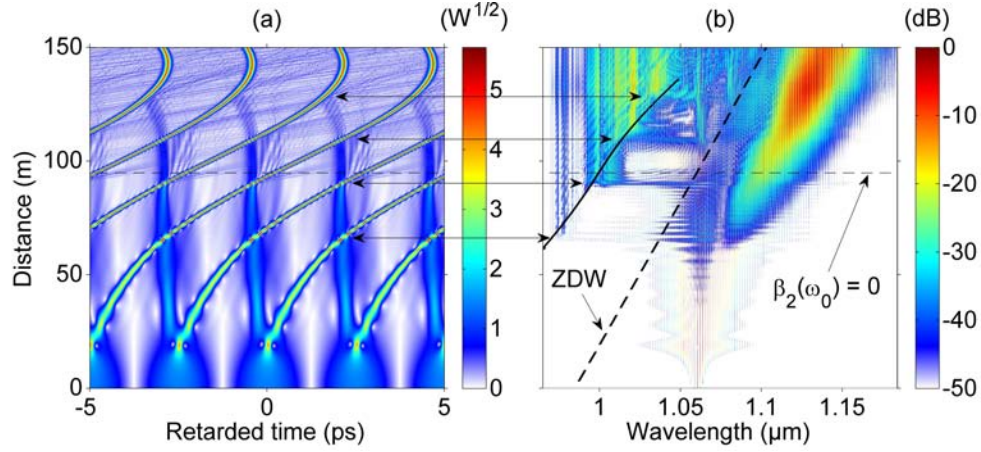


Figure 7.2: Temporal (a) and spectral (b) evolutions of a dual-pump input inside a DDF. (a) shows the square root of the intensity on a linear scale in  $\sqrt{W}$ , and (b) shows the normalized spectral intensity in decibels. The two pumps are separated in frequency by 400 GHz and their total power is 1 W. The dashed black line shows the distance at which  $\beta_2 = 0$  at the pumps' center wavelength. Double arrows mark locations of temporal reflections in (a) together with the corresponding wavelengths in (b). The solid black line in (b) shows the theoretical prediction of the temporal reflection model discussed in the text. The dashed line shows the zero-dispersion wavelength. After [5].

Until each soliton has decelerated enough to temporally overlap with the remnants of the neighboring pulse, each pulse follows single-pulse evolution dynamics. After 65 meters of propagation, the pump remnants of the adjacent pulse see a moving refractive-index barrier caused by solitons, resulting in temporal reflections that create new frequency components between 970 and 980 nm [126]. Most of the pump remnants pass through this index barrier and undergo further temporal reflections creating new spectral components first between 990 nm and 1.02  $\mu\text{m}$ , then 1.02  $\mu\text{m}$  and 1.025  $\mu\text{m}$ , and finally between 1.03  $\mu\text{m}$  and 1.04  $\mu\text{m}$  (after 130 m of propagation).

In a recent study by Plansinis et al. [126] temporal reflections, occurring because of an abrupt temporal change in the refractive index, were studied and the spectral shift of the reflected light was predicted analytically using the conservation of photon momentum during the reflection process. In their theory, the frequency  $\omega$  of reflected light is obtained from

$$\Delta\beta_1(\omega - \omega_0) + \sum_{n \geq 2} \frac{\beta^n}{n!} (\omega - \omega_0)^n = 0, \quad (7.1)$$

where the Taylor expansion has been done around the incident frequency  $\omega_0$  and  $\Delta\beta_1 = \beta_1(\omega_0) - 1/V_B$ ,  $V_B$  being the velocity of the moving refractive index barrier. The trivial solution  $\omega = \omega_0$  corresponds to the incident wave, and the other solution, if it exists, provides the frequency of the reflected wave.

In the case studied here, the intense narrow solitons act as the moving

refractive-index barriers. Therefore, the barrier velocity  $V_B$  is the inverse of the first-order dispersion coefficient  $\beta_1(\omega_s)$ , where  $\omega_s$  is the soliton's center frequency. By virtue of the retarded time coordinate used,  $\beta_1(\omega_0) = 0$ , and the difference  $\Delta\beta_1$  in Eq. (7.1) reduces to  $\Delta\beta_1 = -\beta_1(\omega_s)$ . To determine the value of  $\beta_1(\omega_s)$ , the curved trajectory of a soliton in Fig. 7.2(a) was traced and a polynomial spline was fitted to it, expressing the location  $T_p$  of the soliton peak as a function of  $z$ . The derivative  $dT_p/dz$  then yields  $\beta_1(\omega_s)$ . Knowing  $\beta_1(\omega_s)$ ,  $\omega_s$  was calculated and checked that it agreed with the spectral peak of the solitons. The calculated  $\beta_1(\omega_s)$  was then used to determine the wavelength of the reflected wave when the pump remnants centered around  $1.06 \mu\text{m}$  reflect off the solitonic index barrier. The solid black line in Fig. 7.2(b) shows the predictions for the reflected wavelength based on Eq. (7.1). As seen in this figure, the theoretical predictions agree quite well with the numerical results.

By looking at Fig. 7.2(b) we note that the input spectrum has broadened considerably at a distance of 65 m (just before the first reflection), forming a frequency comb spanning from  $1.02 \mu\text{m}$  to  $1.12 \mu\text{m}$  through dual-pump enhanced SPM [4]. Since there is a band of (discrete) frequencies that can reflect off the solitonic index barriers, the reflected frequencies also form bands around the theoretically predicted curve (solid black line). The width and position of these bands depend on the width of the incident band, the dispersion, and the central wavelength of the solitons [through  $\beta_1(\omega_s)$ ], as evident from Eq. (7.1). Furthermore, the theory of Ref. [126] does not account

for nonlinearities, which affect the propagation constants of both the incident and reflected waves (owing to the Kerr effect). In addition, the nonlinear effects are expected to be different in magnitude for the incident and reflected waves, as the latter is much weaker than the former one.

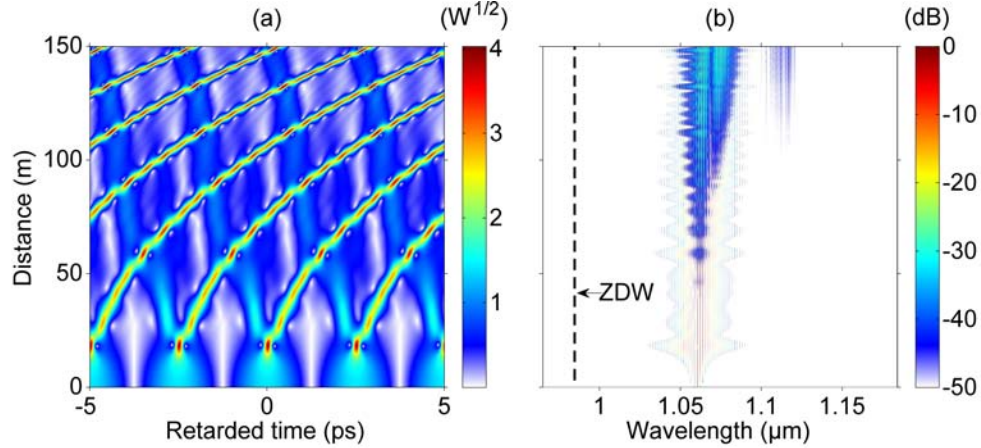


Figure 7.3: Temporal (a) and spectral (b) evolutions of a dual-pump input under conditions identical to those in Fig. 7.2 except that the dispersion is kept constant along the PCF length. After [5].

To clarify the drastic effects of temporal reflections on the blue side of the output spectra, simulations were also performed in constant dispersion fibers with the same dispersion curve shown in Fig. 7.1 for all  $z$ . Figure 7.3 shows the temporal and spectral evolutions of the same input signal in this case and should be compared with Fig. 7.2 where dispersion varies along the fiber length. It is remarkable how narrow the output spectrum is in Fig. 7.3(b) when compared to that in Fig. 7.2(b). The additional spectral broadening in Fig. 7.2(b) has two sources: On the red side, it is due to soliton compression and enhanced SSFS of the narrower solitons. In contrast, on the

blue side, spectral broadening is due to the formation of blue-shifted spectral bands resulting from temporal reflections. Note that there is no visible DW emission in either case, and all the blue-shifted components that are present in Fig. 7.2(b) but not in Fig. 7.3(b) are solely due to temporal reflections of the pump remnants off the solitons.

The absence of a DW in Fig. 7.3 is, at first, somewhat puzzling since such waves are often generated when solitons form. On further investigation, it becomes evident that the reason behind the lack of temporal reflections in Fig. 7.3(b) is related to the shape of the dispersion curve, which causes Eq. (7.1) to have only one solution  $\omega = \omega_0$ , such that no solution exists for a reflected wave. Since no temporal reflections can occur, all pump remnants incident on a solitonic index barrier simply pass through it (temporal refraction), without a significant change in their frequencies [126]. This behavior is due to the presence of dispersion terms beyond the third order in the simulations.

To clarify this issue further, additional numerical simulations were carried out. Figure 7.4 shows the temporal and spectral evolutions under conditions identical to those in Fig. 7.3, except that the value of  $\beta_2$  at the pump's center wavelength was  $-2.684 \text{ ps}^2/\text{km}$  rather than  $-8.56 \text{ ps}^2/\text{km}$  like in Fig. 7.3. This value of  $\beta_2$  corresponds to its value in Fig. 7.2 at a distance of 65 m, which is the location of the first temporal reflection. As in Fig. 7.3, the input beating signal reshapes to form a periodic train of solitons, but unlike in Fig. 7.3, now each soliton emits a DW soon after its formation at a distance of

30 m.

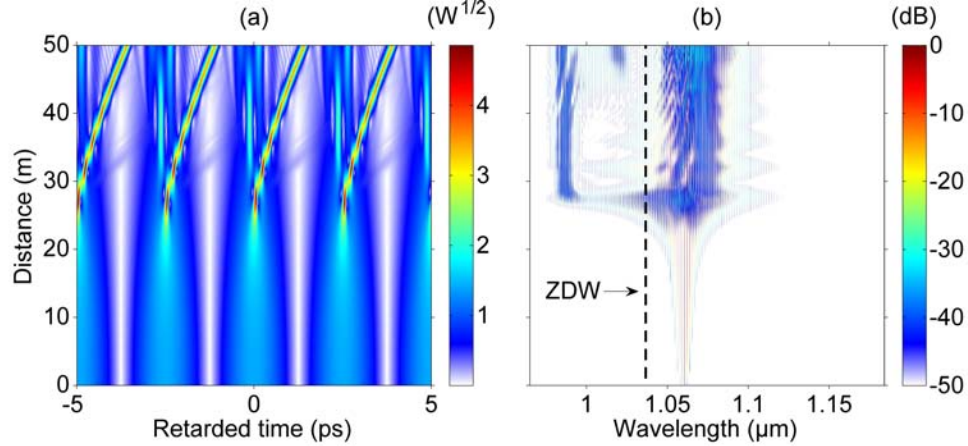


Figure 7.4: Temporal (a) and spectral (b) evolutions under conditions identical to those in Fig. 7.3 except that the value of  $\beta_2$  at the pump-center wavelength was changed to  $-2.684$  ps<sup>2</sup>/km. After [5].

The wavelength of a DW can be calculated from the phase-matching condition [54]:

$$\sum_{n \geq 2} \frac{\beta^n}{n!} (\omega - \omega_0)^n - (\omega - \omega_0)/v_g - \gamma P_0 = 0, \quad (7.2)$$

where  $P_0$  is the soliton's peak power and  $v_g$  its group velocity. In practice, the nonlinear term is often small compared to the others and can be neglected to yield the linear phase-matching condition. When  $\gamma P_0 = 0$ , equation (7.2) is exactly identical to the temporal reflection equation (7.1) when  $V_B = v_g$  because  $\Delta\beta_1 = -1/v_g$  in that situation. When the moving refractive-index boundary is caused by solitons of group velocity  $v_g$ , the condition  $V_B = v_g$  is automatically satisfied, and Eq. (7.1) becomes Eq. (7.2) with  $\gamma P_0 = 0$ . This

indicates that DW emission is a special case of a temporal reflection process. Thus, DW emission in Fig. 7.4 and the formation of blue-shifted components in Fig. 7.2 through a temporal reflection are the same phenomenon. The difference can be understood as follows. In Fig. 7.2 the pump remnants meet and interact with the solitons after they have left the original pulse and slowed down considerably through the SSFS. In contrast, in Fig. 7.4 the pump remnants on the trailing side of each soliton reflect off that soliton itself as it slows down. In other words, DW generation is a kind of “temporal self-reflection”, where the temporal refractive-index boundary is caused by the formation of a soliton in a pulse’s central region, and the trailing parts of the same input pulse reflect off this soliton, changing their frequency as required by the process of temporal reflection. Small differences in the wavelengths of the blue components in Figures 7.2(b) and 7.4(b) can be attributed to slight differences in the solitons’ group velocities and peak powers in the two cases.

Interpreting DW emission as a special case of temporal reflection also explains the lack of DW’s in Fig. 7.3. As mentioned earlier, the shape of the dispersion curve in the case of Fig. 7.3 is such that Eq. (7.1) admits only one solution ( $\omega = \omega_0$ ), and hence no temporal reflections can occur. As the same equation in the form of Eq. (7.2) governs DW emission, no such waves are generated either. All pump remnants initially present during soliton formation at a distance of 20 m simply pass through the solitons without reflecting off them.

It was shown how temporal reflections are a key spectral broadening pro-

cess when two or more closely spaced pulses are transmitted through an optical fiber. Spectral broadening was enhanced considerably in the case of a DDF and attributed the broadening on the blue side to temporal reflections from a moving refractive-index boundary created by the solitons. The recently developed theory of Ref. [126] was able predict the reflected frequency bands in the numerical simulations. Importantly, DW generation can be interpreted as a special case of temporal reflection, in which the spectral components that reflect off the temporal index boundary have the same or nearly the same frequency as the soliton that produces the temporal boundary, hence connecting temporal reflections to a wider range of physical systems.

## 7.1 Higher-Order Dispersive Effects

As seen above, DW emission requires the inclusion of dispersive terms beyond the second order. These dispersive terms also act as perturbations to solitons, as do optical shock effects and Raman scattering. The dispersion parameters  $\beta_n$  in Eq. (4.15) can be easily tailored through proper design of the refractive index profile, which in the case of photonic crystal fibers means appropriately choosing the size and spacing of the air holes surrounding the core. The only limitations regarding the structure of silica-based photonic crystal fibers are associated with manufacturing precision. In general, different photonic crystal fiber structures would also lead to different nonlinear

coefficients for the fibers. However, since it is the relative strength of dispersion and nonlinearity that determines the propagation of light, it is assumed here that the nonlinear parameter is constant while  $\beta_2$  changes linearly along the fiber. It should also be noted that ultra-flat highly anomalous dispersion profiles can be achieved over a wide wavelength range with novel designs [186]. The TOD and other higher-order dispersion terms play a relatively minor role for such fibers.

Higher-order dispersive terms were present in the simulations discussed above and it is not easy to pinpoint their effects by looking at the simulations alone. Following Ref. [6], we can gain a better understanding of their effects in a DDF by turning them off altogether and simulating a fiber with only  $\beta_2$ . Figure 7.5 shows the evolution of a dual-pump signal when  $\beta_2$  increases linearly from  $-10$  to  $0$  ps<sup>2</sup>/km over 100 m. The nonlinear parameter is  $\gamma = 0.0916$  (Wm)<sup>-1</sup>. The power of both pumps is 1 W, they are separated by 800 GHz and centered around 1060 nm. The two traces on top show changes in the pulse width and peak powers over the 100 m length of the fiber. The initial sinusoidal pattern gradually reshapes into a train of solitons whose width decreases and peak power increases continuously until the pulse becomes less than 3 optical cycles long and the numerical model itself starts to break down. The spectrum of the resulting pulse train is in the form of a frequency comb whose bandwidth is inversely proportional to the width of the solitons and exceeds 100 THz.

The compression dynamics in Fig. 7.5 have interesting features. The

initial sinusoidal pattern with a period of 1.25 ps evolves into a pulse train within the first 10 m such that individual pulses are about 200 fs wide (full width at half maximum, FWHM). These soliton-like pulses then broaden with further propagation before being compressed a second time. This process repeats a few times but the pulse duration keeps a downward trend while exhibiting transient oscillations. During the first 50 m or so the beat input displays a form of Fermi-Pasta-Ulam-Tsingou recurrence perturbed by the changing dispersion and evolves essentially like a breather before the intensity peaks become solitons. The simulation shown in Fig. 7.5 does not include third-order dispersion but breathers are sensitive to all kinds of asymmetric perturbations, such as Raman scattering, which can [187] and will [188] turn the breather into a train of solitons. The subsequent evolution of the solitons is affected by two mechanisms. First, varying fiber dispersion forces them to compress. Second, at the same time, their speed is reduced as their spectrum red shifts because of SSFS (leading to bending of the trajectories in Figure 7.5). The individual solitons grow in intensity because of the increasing  $\beta_2$ , but also because they feed off the darker regions (energy in the low-intensity parts) when they shift in time and overlap temporally with them. This mode of energy transfer to the solitons is evident in Fig. 7.5, where the regions between the neighboring solitons become darker as the solitons slow down and pass through these regions. This energy transfer perturbs the solitons, causing their widths and peak powers to oscillate around their respective trends (decreasing duration, increasing peak power). One way to look at the

evolution of the beating input signal is to interpret the duration and peak power oscillations as a manifestation of the gradually disappearing breather nature whereas the general trend of decreasing duration and increasing power can be considered to represent soliton compression.

The GNLSE model given in Eq. (4.15) accurately describes pulse propagation down to the single-cycle regime [90, 19], and here the three-cycle point is used as the cutoff for the validity of the GNLSE model. The distance at which the solitons in Fig. 7.5 have compressed to three optical cycles in duration (about 10 fs) is approximately 98 meters, and this has been indicated by the vertical dashed lines in Fig. 7.5. The important takeaway from Fig. 7.5 is that the initial beating intensity pattern with a period of 1.25 ps (corresponding to 800 GHz) could ideally be reshaped into a train of solitons that are only three optical cycles long. The input FWHM of the cosine-shaped pulses is 625 fs, implying that the compression factor is larger than 50.

The power of both pumps in Fig. 7.5 was 1 W, but other average powers yield similar results as long as the energy contained within each beat period is comparable to the energy of a soliton of similar or shorter duration than the beat period. The energy within each period is 1.25 pJ for a 800 GHz repetition rate signal with an average power of 1 W. A soliton with such energy would have a duration (FWHM) of 308 fs given the parameters at the fiber input [nonlinear parameter of  $\gamma = 0.0916 \text{ (Wm)}^{-1}$  and the initial GVD of  $\beta_2 = -10 \text{ ps}^2/\text{km}$ ], which means that each beat period has enough energy to reshape into one soliton by compressing slightly. Decreasing the input

power weakens the nonlinear effects and thus the formation of temporally separated solitons takes longer. Their formation is also affected by how the GVD parameter  $\beta_2$  changes since  $\beta_2$  determines the relation between the solitons' duration and energy. Lower input powers could be at least partially compensated for by changing the input end value of  $\beta_2$ .

When the average power is increased, two solitons can form within each period and two soliton trains with different group velocities are formed. The more intense soliton train red shifts faster and feeds off the weaker train through Raman-induced power transfer every time the trains overlap temporally. The weaker soliton train eventually disappears after all the power has been transferred to the other train. The result is a more intense train of solitons that are also shorter in duration as dictated by the soliton condition. The solitons in the remaining train are not uniform and differ slightly in peak power and duration due to them having undergone noise- and phase-sensitive soliton interactions [120]. Some solitons in the train then move faster than others and the pulse train loses its periodicity. Even higher average powers lead to more solitons per period, as each beat pulse breaks into multiple solitons. The dynamics become more and more chaotic with increasing power, and periodicity is lost faster. A similar loss of periodicity can be observed for very high repetition rates (input pump separations), such as 2 THz. The input power should be increased approximately quadratically with the input pump separation to maintain the required amount of energy for a soliton within each beat period, which makes the forming short solitons susceptible

to slight differences in their durations and peak powers due to noise. Again these differences eventually break the periodicity of the pulse train. The spectra of these THz-range repetition rate pulse trains could be Raman shifted by nearly an octave in the simulations but their periodicity and quality deteriorated significantly. There are general trade-offs between repetition rate, output wavelength, pulse duration, and the quality of the generated pulse train. The simulations indicate that the limitations are fundamental as the pulse train quality degradation was caused by shot-noise.

The simulation shown in Fig. 7.5 includes all the relevant effects that would be present in reality, with the exception of higher-order dispersion and losses. The fiber was assumed to be lossless and to have perfectly flat dispersion (constant  $\beta_2$ ) over all wavelengths at any given point of the fiber. Therefore, Fig. 7.5 represents the best case scenario in terms of how short the solitons can become: Under ideal conditions pulse durations of three optical cycles or less could be achieved. Several different effects might prevent such drastic compression shown in Fig. 7.5 in practice, but the extent of compression is not limited by GVD, intrapulse Raman scattering, or optical shock effects. Losses would cause the peak power  $P_0$  of the forming solitons to be smaller, which in turn would lead to larger soliton durations  $T_0$  such that the soliton condition of  $\gamma P_0 T_0^2 / \beta_2(z) = 1$  continues to be satisfied. However, at the end of the fiber GVD is zero ( $\beta_2 = 0$ ), and the soliton condition can only be satisfied for infinitely narrow solitons no matter what the peak power might be. Compensation for losses through decreasing dispersion (increasing

$\beta_2$ ) to keep the soliton duration unchanged upon propagation in lossy fibers has been demonstrated in the past [189]. Decreasing dispersion even faster than in Fig. 1 would be required to compensate for any possible fiber losses. However, TOD could be expected to change the compression dynamics more drastically than losses because it affects solitons in at least three different ways: it leads to dispersive-wave emission, it asymmetrically distorts the shape of a soliton, and it makes  $\beta_2$  frequency-dependent.

The first thing to note is that the sign of TOD plays an important role in the evolution of a short solitons undergoing intrapulse Raman scattering. The SSFS causes the soliton spectrum to red shift, and it is the sign of  $\beta_3$  that then determines whether the soliton will experience a larger or smaller  $\beta_2$  as a consequence. Since soliton compression is based on increasing  $\beta_2$  from an initially negative value through dispersion engineering, any TOD-induced change to  $\beta_2$  will affect the compression of solitons. The presence of TOD also introduces a spectral region of normal dispersion in which solitons cannot exist but also guarantees the existence of a spectral region of anomalous dispersion even when  $\beta_2 > 0$  at the pump frequency. The signs of  $\beta_2$  and  $\beta_3$  determine whether the normal dispersion regime is on the red or the blue side of the soliton. The frequency at which GVD changes sign is given by  $\omega_{\text{ZDW}} = \omega_0 - \beta_2/\beta_3$  where  $\beta_2$  and  $\beta_3$  are evaluated at the central frequency  $\omega_0$ . The wavelength corresponding to  $\omega_{\text{ZDW}}$  is the ZDW. When  $\beta_2$  is a linear

function of distance  $z$  we have

$$\beta_2(\omega_0) = \beta_2^{\text{in}} + (\beta_2^{\text{out}} - \beta_2^{\text{in}}) \frac{z}{L} \quad (7.3)$$

where  $L$  is the length of the fiber and  $\beta_2^{\text{in}}$  and  $\beta_2^{\text{out}}$  are the input and output values of  $\beta_2$  at  $\omega_0$ , respectively. Consequently the ZDW becomes a function of  $z$  through

$$\omega_{\text{ZDW}} = \omega_0 - \frac{\beta_2^{\text{in}}}{\beta_3} - (\beta_2^{\text{out}} - \beta_2^{\text{in}}) \frac{z}{\beta_3 L}. \quad (7.4)$$

To illustrate the effects of TOD in a DDF, Fig. 7.6 shows the evolution in a fiber where  $\beta_2$  changes from  $-10 \text{ ps}^2/\text{km}$  to  $5 \text{ ps}^2/\text{km}$  over 150 meters and where  $\beta_3 = -0.03 \text{ ps}^3/\text{km}$ . Note that the rate of change of  $\beta_2$  with  $z$  is the same as for the fiber in Fig. 7.5 and the ZDW coincides with the pump center wavelength at exactly 100 meters just like in Fig. 7.5.

The evolution of the dual-pump shown in Fig. 7.6 differs from that of Fig. 7.5. The most noticeable difference between the two cases is that the pulses do not become infinitely narrow when  $\beta_3 \neq 0$  and the minimum pulse duration in Fig. 7.6 is approximately 180 fs. The formation of few-cycle pulses would require a very broad pulse spectrum and since the pulses are solitons this spectrum would have to lie in the anomalous dispersion regime. When  $\beta_3 \neq 0$  and the ZDW approaches the soliton spectrum, the tail of the pulse spectrum will eventually end up in the normal dispersion regime thus limiting the spectral extent and consequently the pulse duration of the solitons. The first effects can be observed after 80 m of propagation when the ZDW starts

to touch the tail of the soliton spectrum and power is transferred from the solitons to a dispersive wave on the red side of the ZDW. The moving ZDW gradually puts more and more energy to the normal dispersion regime and the soliton peak powers start to decrease. The ZDW crosses the center of the soliton spectrum around 110 m and after this the solitons cease to exist and disperse into a chaotic-looking yet nearly-periodic pattern of interfering waves in the normal dispersion regime. After this point it is no longer meaningful to talk about soliton peak powers or durations or consider the intensity profile a train of pulses.

In the example shown in Fig. 7.6 the frequency slope of  $\beta_2$  was negative ( $\beta_3 < 0$ ) and hence the normal dispersion regime was on the red side of the pump. Solitons have a tendency to try to stay away from the ZDW and remain in the anomalous regime, which can be seen in the spectrum of Fig. 7.6 where the spectral trajectory of the soliton bends slightly downwards between 90 m and 110 m and the solitons blue shift. The blue shift is always accompanied by significant transfer of energy to the red side of the ZDW to conserve total energy. Normally solitons, especially short ones, have a tendency to red shift upon propagation because of intrapulse Raman scattering. This raises the question whether having the ZDW approach the soliton spectrum from the blue side instead would help the solitons remain in the anomalous regime for longer distances. Figure 7.7 shows the evolution of a 800 GHz dual-pump in a fiber with  $\beta_3 = 0.03 \text{ ps}^3/\text{km}$ . Other than the fiber length and the TOD, the fiber is similar to the ones in Figs. 7.5 and 7.6 and

again the ZDW is at the pump center at 100 m. Note that the temporal trace in Fig. 7.7 is now in the reference frame of the solitons instead of moving at the group velocity at the pump frequency.

The evolution of the soliton power and duration is similar to that of Fig. 7.6 but the solitons last longer and the spectral evolution looks very different. The ZDW is now on the blue side of the solitons and the ZDW approaching the soliton spectrum greatly enhances the natural SSFS pushing the soliton spectrum all the way to 1.25  $\mu\text{m}$  from the initial 1.06  $\mu\text{m}$ . Still, the moving ZDW eventually overtakes the soliton spectrum and in the end the pulses end up in the normal dispersion regime and disperse. The minimum soliton duration is 125 fs around 185 m.

To understand quantitatively the impact of  $\beta_3$ , a large number of numerical simulations was carried out for different DDF designs. Figure 7.8 shows the color-coded duration of solitons (range 0–250 fs) for  $\beta_3$  values varying from  $-0.1$  to  $0.1$   $\text{ps}^3/\text{km}$  along the  $x$  axis and different values of  $\beta_2(L)$  at the end of a 200-m-long fiber with  $\beta_2(0) = -10$   $\text{ps}^2/\text{km}$ . In each case,  $\beta_3$  is kept constant along the fiber. The four plots shows the soliton widths at distances of (a) 80, (b) 120, (c) 160, and (d) 200 m.

If the solitons forming from the beating input signal are able to keep up with the gradually changing GVD parameter  $\beta_2$ , then larger final values of  $\beta_2$  leads to shorter solitons. The general trend in Fig. 7.8 is that increasing the final value of  $\beta_2$  makes the output pulses shorter, which means that solitons are mostly able to keep up with the longitudinally changing GVD,

even when GVD becomes normal near the fiber end. This is also corroborated by Figs. 7.5 where pulse duration has a downward linear trend approaching zero with decaying transient oscillations. The transient oscillations die out by the end of a 200-meter-long fiber when the final value of  $\beta_2$  is larger than  $-5 \text{ ps}^2/\text{km}$ , as seen in Fig. 7.8. The temporal compression continues even after the oscillations disappear.

The effects of TOD are clearly visible in Fig. 7.8. Larger values of  $|\beta_3|$  hinder pulse compression, whereas smaller values lead to shorter pulses at shorter distances. The explanation for this lies in how  $\beta_3$  affects the  $\beta_2$  that the soliton experiences and in the Raman effect that causes the soliton spectrum to red shift through SSFS with propagation. The TOD parameter is given by  $\beta_3 = d\beta_2(\omega)/d\omega$  evaluated at the central frequency  $\omega_0$ . Negative values of  $\beta_3$  thus mean that  $\beta_2$  decreases with optical frequency and hence increases with wavelength. SSFS then causes the solitons to experience a larger GVD parameter  $\beta_2$  (i.e. smaller  $|\beta_2|$  since  $\beta_2$  stays negative) compared to the initial pump center frequency. Negative values of  $\beta_3$  together with SSFS imply that  $\beta_2$  at the solitons' central frequency increases (from negative values towards zero) even faster than  $\beta_2$  at the pump center frequency, thus causing the solitons to compress rapidly. The opposite occurs for positive values of  $\beta_3$ . As seen in Fig. 7.5, solitons could be compressed down the three optical cycles in the absence of TOD, but in practice pulse compression is limited by it. We note that fibers with  $\beta_3 = 0$  can also be manufactured (so-called dispersion-flattened fibers); pulse compression would be limited by fourth-

order dispersion. There is no way to make the group-velocity dispersion completely flat across the whole soliton spectrum and pulse compression will always be limited by higher-order dispersion.

It is evident from Fig. 7.8 that soliton trains with pulse widths  $< 100$  fs can be achieved with many different parameter combinations. Even a 100-meter fiber can be long enough to produce such an ultrashort pulse train if  $\beta_2$  of the DDF increases rapidly enough with distance [see Fig. 7.8(b)]. Both negative and positive values of  $\beta_3$  work, and two different sets of fiber parameters can lead to very similar-looking pulse trains. Figure 7.9 shows portions of two pulse trains generated using two different fibers with the same input. Both fibers have the same GVD at the input end but their lengths and final values of  $\beta_2$  are different. Their TOD parameters are equal in magnitude but opposite in sign. The solitons generated in each fiber are nearly identical: their energies and pulse durations are within 2% of one another. The only notable difference is that the pulses in the fiber with  $\beta_3 > 0$  (Fiber A) exhibit a small bump near the trailing end. The differences between the pulse trains are subtle in the time domain but become quite evident in the spectral domain to which we turn in the next section.

Before moving on to the spectral domain, it should be reiterated that dispersion orders higher than three were neglected altogether. Whereas accurately modeling the dispersion of a real fiber over a large spectral range would require the inclusion of fourth- (4OD) and higher-order dispersion, the key point here is not the actual shape of the dispersion profile but that that a

non-solitonic normal dispersion spectral region that changes along the length of the fiber will limit the spectral extent and hence the duration of the forming solitons and also push them towards longer or shorter wavelengths. The existence of such a region of normal dispersion is always guaranteed when the highest order of dispersion is odd, but a positive 4OD parameter  $\beta_4$  would also guarantee a normally dispersive regime that would repel solitons. On the other hand, a negative  $\beta_4$  would just perturb the shape of the solitons symmetrically [190]. It is worth mentioning, however, that the inclusion of 4OD and/or higher-order dispersion makes it possible to have two ZDWs approach the soliton spectrum from both the red and the blue side, and such a narrowing of the anomalous spectral regime might be useful in controlling the soliton shape or trapping the solitons more robustly within a narrow part of the spectrum. Furthermore, it was demonstrated that flat dispersion leads to the shortest pulses, and 4OD and higher-order dispersion can make the dispersion locally flat for certain wavelengths even in the presence of TOD, which might have practical implications for few-cycle soliton train generation using a dual-pump input.

## **7.2 The Central Wavelength of the Frequency Comb**

The output spectrum of any periodic ultrashort pulse train generated through dual-pumping is in the form of a frequency comb whose comb lines are sepa-

rated by the initial spacing between the frequencies of the two input pumps. Figure 7.10 shows the spectra corresponding to the two identical-looking pulse trains shown in Fig. 7.9. The spectra resemble mirror images of one another because of the opposite signs of the TOD parameter  $\beta_3$ . The soliton part of the spectrum (dominant peak) of fiber A is centered at 1086.1 nm, while that of fiber B is at 1067.5 nm, a difference of 18.6 nm (4.81 THz). As a reminder, the input center wavelength of the two pumps is at 1060 nm.

The central frequency at each point in the fiber is determined by several processes. The first one is SSFS which causes the solitons to red shift. The second one is the tendency of solitons to stay away from the ZDW in the spectral domain [191], and a moving ZDW can manifest as an effective push for the soliton spectrum. Depending on whether this push comes from the red side or the blue side, it can respectively hinder or enhance the red shift (See Figs. 7.6 and 7.7, respectively). For  $\beta_3 > 0$  we have  $\omega_{\text{ZDW}} > \omega_0$ , and  $\omega_{\text{ZDW}}$  approaches  $\omega_0$  from the blue side, enhancing the red shift and pushing the solitons further into the red. When  $\beta_3 < 0$ ,  $\omega_{\text{ZDW}}$  approaches  $\omega_0$  from the red side and SSFS is thus hindered. This is the reason the spectrum out of fiber A in Fig. 7.10 is more red shifted than that of fiber B.

If  $\beta_2^{\text{out}} > 0$ ,  $\omega_{\text{ZDW}}$  always surpasses  $\omega_0$  no matter how fast or slow its rate of change. The rate of change is proportional to  $1/\beta_3$  as seen in Eq. (7.4), which means that when  $\beta_3$  is close to zero,  $\omega_{\text{ZDW}}$  changes rapidly with distance  $z$ . Based on this argument, it seems likely that solitons could be pushed towards even longer wavelengths by making  $\beta_3$  smaller while keeping it pos-

itive. Figure 7.11 shows the central wavelength of the pulse trains generated through dual-pumping at distances of 80 m, 120 m, 160 m, and 200 m under conditions identical to those of Fig. 7.8 as a function of  $\beta_2^{\text{out}}$  and  $\beta_3$ . The initially forming solitons are wide at first and, as a result, red shifts of  $< 5$  nm occur up to a distance of 50 m. Much larger shifts occur at distances beyond 100 m, especially for large values of  $\beta_2^{\text{out}}$  for which adiabatic soliton compression kicks in and makes the solitons shorter thus enhancing their SSFS. The largest red shifts occur in the regime where  $\beta_2^{\text{out}} > 0$  and  $\beta_3$  is small but positive. The soliton central frequency can be red shifted by more than 25% to 1.35 nm before  $\omega_{\text{ZDW}}$  moves beyond the soliton central frequency and disperses the solitons.

These results demonstrate that the technique of dual-wavelength pumping can be used to generate soliton pulse trains at ultrahigh-repetition rates (up to 1 THz or more) and that the solitons could be compressed temporally inside a dispersion-decreasing fiber down to the few-cycle regime (pulse widths as short as 10 fs at wavelengths near 1  $\mu\text{m}$ ). The repetition rate used here was 800 GHz, but since it is set by the frequency separation of two CW pumps, it can be tuned over a wide range by choosing the input pump wavelengths suitably. It was further pointed out that the soliton compression is limited by higher-order dispersion with small values of the GVD slope  $\beta_3 = d\beta_2/d\omega$  leading to shortest pulses. It was also shown that third-order dispersion is crucial in determining the output wavelength of the pulses. Small positive values of the GVD slope lead to the largest red shifts and the

longest output wavelengths. Sub-100 fs solitonic pulses with a wavelength anywhere between 1060 nm and 1350 nm could be achieved in the simulations, making dual-wavelength pumped optical fibers a versatile platform for generating femtosecond pulses at high-repetition rates that have a variety of applications ranging from biomedical imaging to the manipulation of motion of individual molecules.

The spectral features of the generated pulse trains are also remarkable. The results clearly show that the dual-pumping scheme is capable of generating frequency combs that extend over 50 THz and whose center frequency is tunable over 60 THz in the vicinity of 1150 nm. Moreover, the comb spacing in itself can be tuned over a wide range ( $\sim 0.1$  to  $\sim 1$  THz or even higher at the expense of the quality of the comb) by choosing the pump wavelengths suitably. As a final remark, the same technique should work for generating optical frequency combs from the visible to mid-infrared region using different fiber designs and materials.

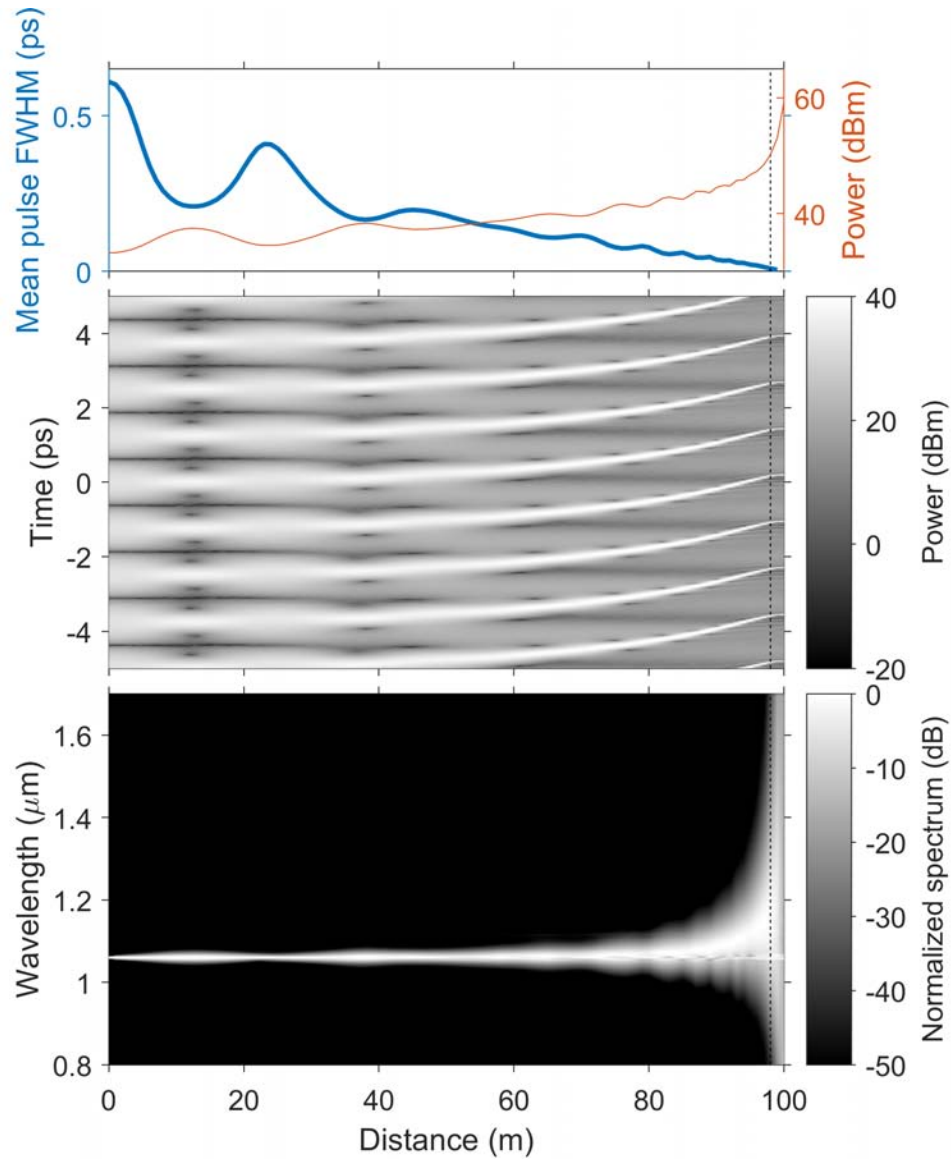


Figure 7.5: The temporal (middle) and spectral (bottom) evolution of a dual-pump signal over 100 meters of a DDF with  $\beta_2$  increasing from  $-10 \text{ ps}^2/\text{km}$  to  $0 \text{ ps}^2/\text{km}$ . The gray intensity scales are logarithmic. The top two traces show the duration (thick blue) and peak power (thin red) of the forming pulses as a function of distance. The vertical black dashed lines indicate the distance at which the soliton width has been reduced to three optical cycles. After [6].

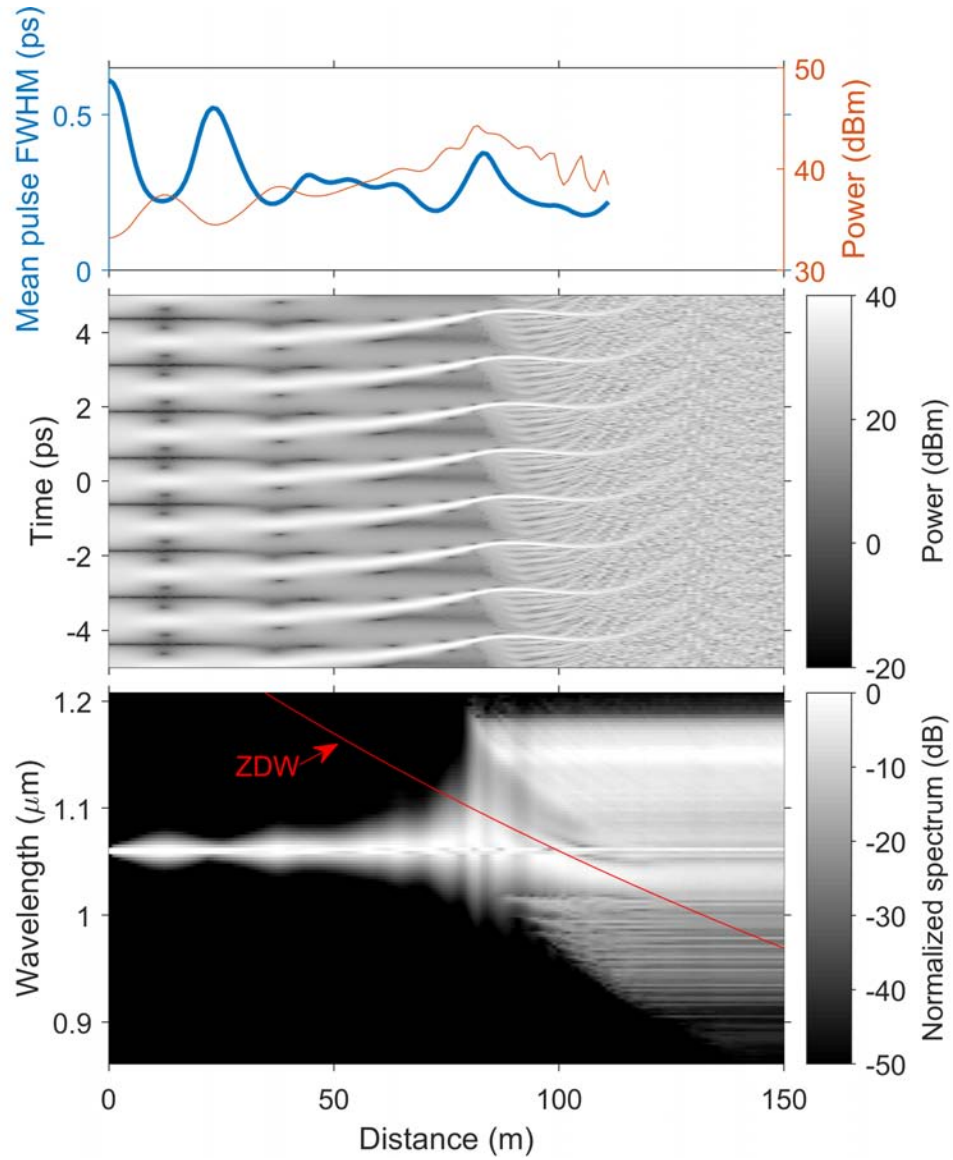


Figure 7.6: The evolution of a 800 GHz dual-pump signal in a fiber in which  $\beta_2$  grows from  $-10 \text{ ps}^2/\text{km}$  to  $5 \text{ ps}^2/\text{km}$  along its 150 m length. Third-order dispersion is  $\beta_3 = -0.03 \text{ ps}^2/\text{km}$ . After [6].

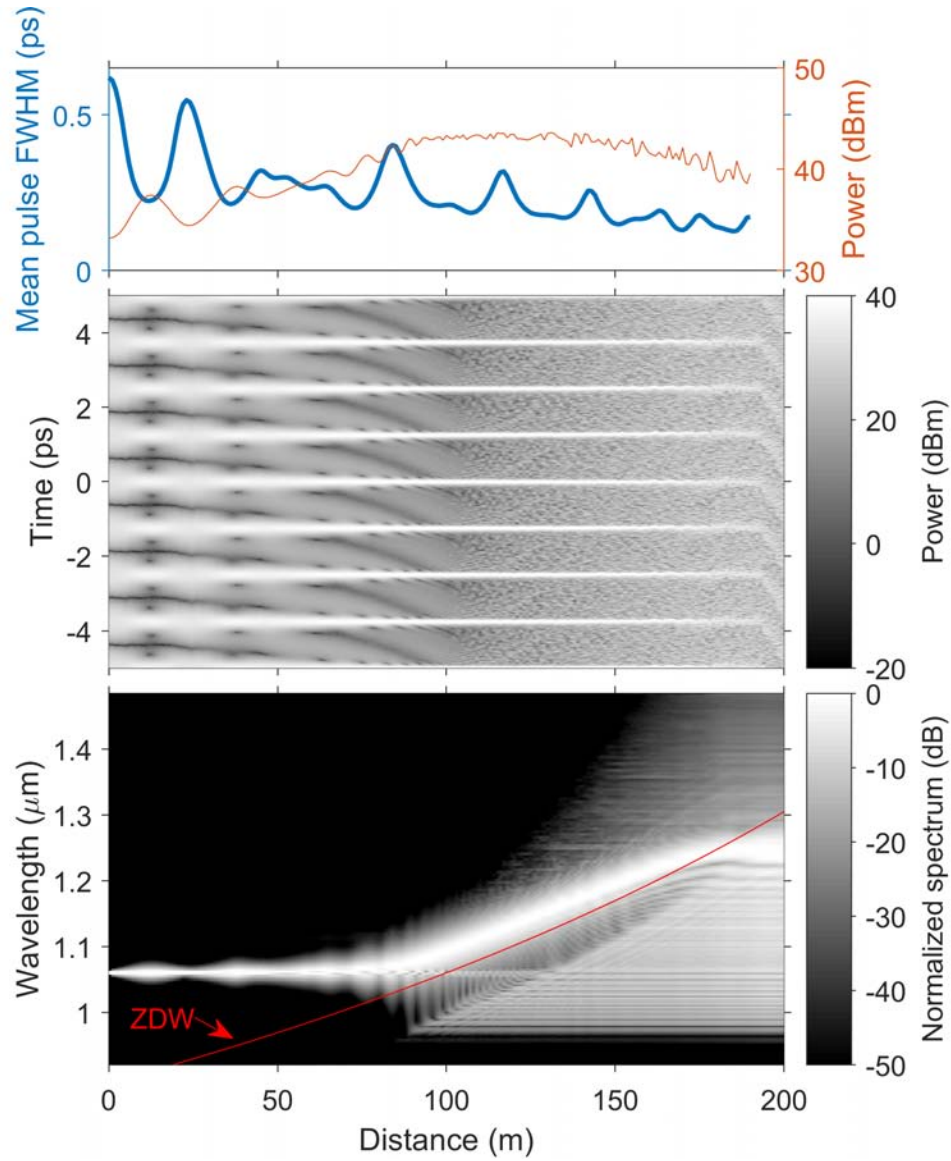


Figure 7.7: The evolution of a 800 GHz dual-pump signal in a fiber in which  $\beta_2$  grows from  $-10 \text{ ps}^2/\text{km}$  to  $10 \text{ ps}^2/\text{km}$  along its 200 m length. Third-order dispersion is  $\beta_3 = 0.03 \text{ ps}^3/\text{km}$ . Unlike in Figs. 7.5 and 7.6, the temporal frame of reference is now with respect to the solitons, as their trajectories would look heavily curved in the pump frame of reference. After [6].

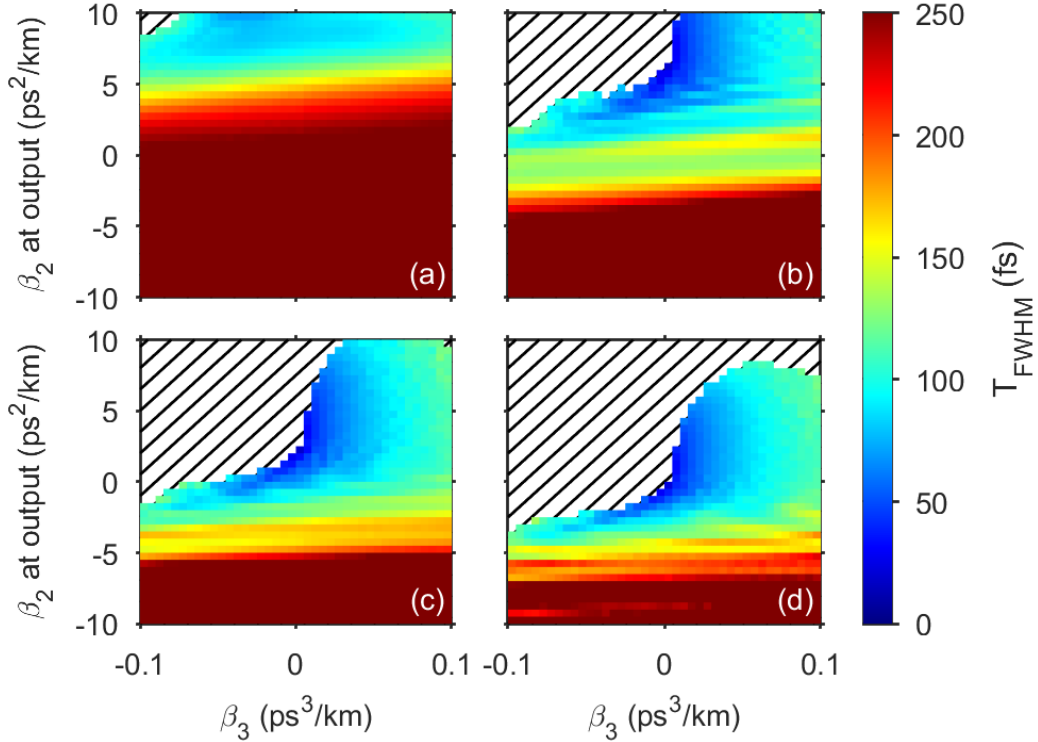


Figure 7.8: The mean duration (FWHM, color coded) of the forming solitons after a) 80 m, b) 120 m, c) 160 m, and d) 200 m of propagation as a function of  $\beta_3$  and the final value of  $\beta_2$ . The initial value of  $\beta_2$  at the input end of 200-meter-long fiber is  $-10 \text{ ps}^2/\text{km}$ . The striped areas in the upper left corners are regions where the pulses have lost their solitonic nature by virtue of having transferred energy to the normal dispersion regime. After [6].

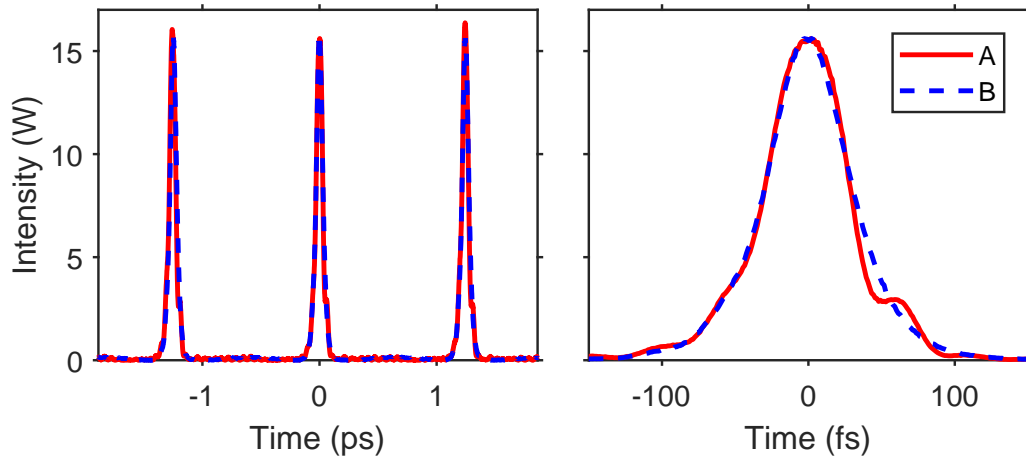


Figure 7.9: Comparison of pulse trains generated with the same dual-pump input in two different fibers. Fiber A is 100 m long and its GVD increases linearly from  $-10 \text{ ps}^2/\text{km}$  to 0 over this length with  $\beta_3 = 0.05 \text{ ps}^3/\text{km}$ . Fiber B is 97 m long but its GVD increases from  $-10$  to  $-2.725 \text{ ps}^2/\text{km}$  with  $\beta_3 = -0.05 \text{ ps}^3/\text{km}$ . The total input power is 2 W and initial pump separation is 800 GHz. The two traces on the right show the pulse around  $T = 0$  showing how closely their shapes match. After [6].

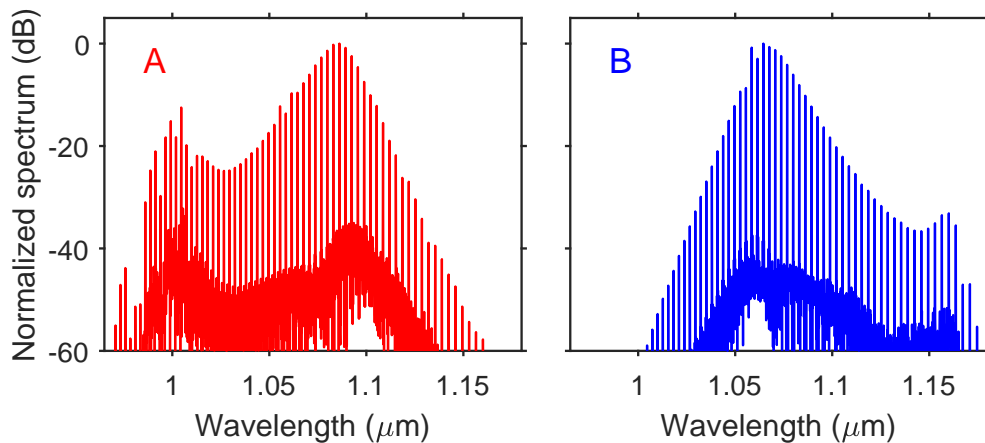


Figure 7.10: Spectra of the two pulse trains shown in Fig. 7.9 at the output of fibers A and B. After [6].

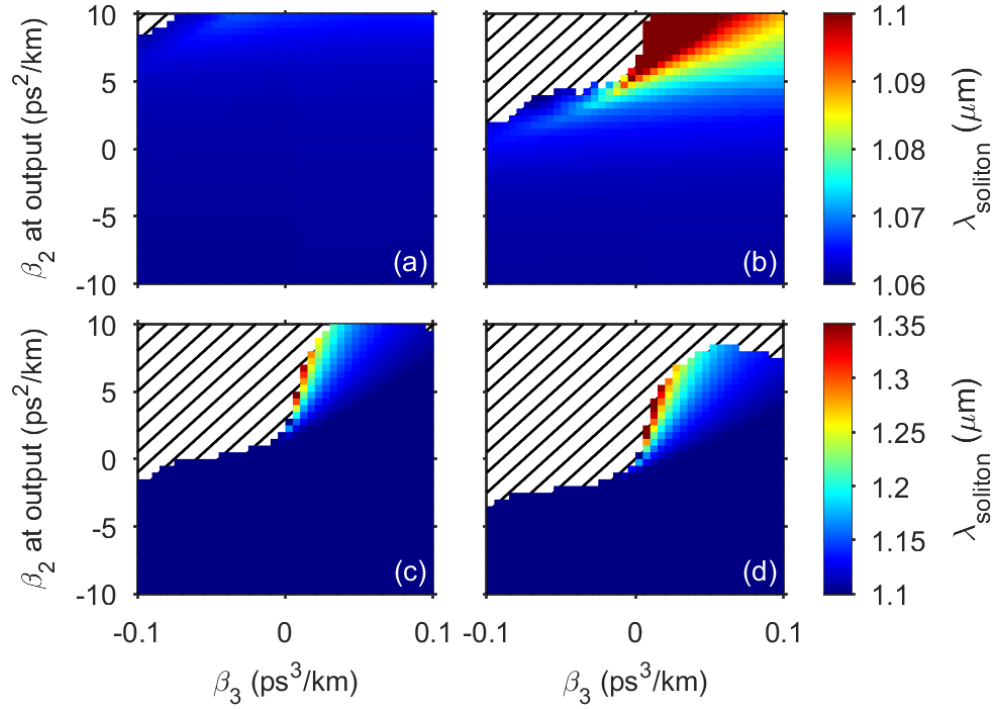


Figure 7.11: The central wavelengths  $\lambda_{\text{soliton}}$  of the forming solitons for the parameters used in Fig. 7.8 after a) 80 m, b) 120 m, c) 160 m, and d) 200 m of propagation. The striped regions indicate that the pulses have lost their solitonic nature and have dispersed. The upper colorbar is for the top row and the lower one for the bottom row; note the different scales. After [6].

## Bibliography

- [1] Bahaa E. A. Saleh and Malvin C. Teich. *Fundamentals of Photonics*. Wiley, 2007.
- [2] Fredrik Jonsson. *Lecture Notes on Nonlinear Optics*. Royal Institute of Technology, 2003.
- [3] F. R. Arteaga-Sierra, A. Antikainen, and Govind P. Agrawal. Dynamics of soliton cascades in fiber amplifiers. *Optics Letters*, 41:5198–5201, 2016.
- [4] Aku Antikainen and Govind P. Agrawal. Dual-pump frequency comb generation in normally dispersive optical fibers. *Journal of the Optical Society of America B*, 32:1705–1711, 2015.
- [5] A. Antikainen, F. R. Arteaga-Sierra, and G. P. Agrawal. Temporal reflection as a spectral-broadening mechanism in dual-pumped dispersion-decreasing fibers and its connection to dispersive waves. *Physical Review A*, 95:033813, 2017.
- [6] A. Antikainen and Govind P. Agrawal. Femtosecond pulse trains through dual pumping of optical fibers: role of third-order dispersion. *Journal of the Optical Society of America B*, 35:1733–1740, 2018.
- [7] Eugene Hecht. *Optics, Third Edition*. Addison Wesley Longman, 1998.
- [8] Robert W. Boyd. *Nonlinear Optics, Third Edition*. Academic Press, 2008.
- [9] Orazio Svelto. *Principles of Lasers, fourth edition*. Springer, 1998.

- 
- [10] R. R. Alfano and S. L. Shapiro. Emission in the region 4000 to 7000 Å via four-photon coupling in glass. *Phys. Rev. Lett.*, 24:584–587, 1970.
- [11] R. R. Alfano and S. L. Shapiro. Observation of self-phase modulation and small-scale filaments in crystals and glasses. *Phys. Rev. Lett.*, 24:592–594, 1970.
- [12] R. R. Alfano and S. L. Shapiro. Direct distortion of electronic clouds of rare-gas atoms in intense electric fields. *Phys. Rev. Lett.*, 24:1217–1220, 1970.
- [13] Chinlon Lin and R. H. Stolen. New nanosecond continuum for excited-state spectroscopy. *Appl. Phys. Lett.*, 28:216–218, 1976.
- [14] Robert R. Alfano. *The Supercontinuum Laser Source, 2nd edition*. Springer, 2006.
- [15] T. Morioka, K. Mori, and M. Saruwatari. More than 100-wavelength-channel picosecond optical pulse generation from single laser source using supercontinuum in optical fibres. *Electronics Letters*, 29:862–864, 1993.
- [16] T. Morioka, H. Takara, S. Kawanishi, O. Kamatani, K. Takigushi, K. Uchiyama, M. Sarawatari, H. Takahashi, M. Yamada, T. Kanamori, and H. Ono. 1 tbit/s (100gbit/s x 10 channel) otdm/wdm transmission using a single supercontinuum wdm source. *Electron. Lett.*, 32:906 – 907, 1996.
- [17] J. C. Knight, T. A. Birks, P. S. J. Russell, and D. M. Atkin. All-silica single-mode optical fiber with photonic crystal cladding. *Optics Letters*, 21:1547–1549, 1996.
- [18] Jinendra K. Ranka, Robert S. Windeler, and Andrew J. Stentz. Visible continuum generation in air-silica microstructure optical fibers with anomalous dispersion at 800 nm. *Optics Letters*, 25:25–27, 2000.
- [19] J. M. Dudley, G. Genty, and S. Coen. Supercontinuum generation in photonic crystal fiber. *Reviews of Modern Physics*, 78:1135–1176, 2006.

- 
- [20] R. Holzwarth, T. Udem, T. W. Hänsch, J. C. Knight, W. J. Wadsworth, and P. S. J. Russell. Optical frequency synthesizer for precision spectroscopy. *Phys. Rev. Lett.*, 85:2264–2267, 2000.
- [21] I. Hartl, X. D. Li, C. Chudoba, R. K. Ghanta, T. H. Ko, J. G. Fujimoto, J. K. Ranka, and R. S. Windeler. Ultrahigh-resolution optical coherence tomography using continuum generation in an air-silica microstructure optical fiber. *Optics Letters*, 26:608–610, 2001.
- [22] E. P. Ippen, C. V. Shank, and T. K. Gustafson. Self-phase modulation of picosecond pulses in optical fibers. *Appl. Phys. Lett.*, 24:190–192, 1974.
- [23] R. H. Stolen and Chinlon Lin. Self-phase-modulation in silica optical fibers. *Phys. Rev. A*, 17:1448–1453, 1978.
- [24] R. H. Stolen, J. E. Bjorkholm, and A. Ashkin. Phase-matched three-wave mixing in silica fiber optical waveguides. *Appl. Phys. Lett.*, 24:308–310, 1974.
- [25] R. H. Stolen. Phase-matched-stimulated four-photon mixing in silica-fiber waveguides. *IEEE Journal of Quantum Electronics*, 11:100–103, 1975.
- [26] V. V. Grigoryants, B. L. Davydov, M. E. Zhabotinski, V. F. Zolin, G. A. Ivanov, V. I. Smirnov, and Yu. K. Chamorovski. Spectra of stimulated raman scattering in silica-fibre waveguides. *Optical and Quantum Electronics*, 9:351–352, 1977.
- [27] John AuYeung and A. Yariv. Spontaneous and stimulated raman scattering in long low loss fibers. *IEEE Journal of Quantum Electronics*, 14:347–352, 1978.
- [28] Y. R. Shen and N. Bloembergen. Theory of stimulated brillouin and raman scattering. *Phys. Rev.*, 137:1787–1805, 1964.
- [29] V. V. Grigoryants, V. I. Smirnov, and Yu K. Chamorovskii. Generation of wide-band optical continuum in fiber waveguides. *Sov. J. Quant. Elect.*, 12:841–847, 1982.

- 
- [30] F. M. Mitschke and L. F. Mollenauer. Discovery of the soliton self-frequency shift. *Optics Letters*, 11:659–661, 1986.
- [31] Akira Hasegawa and Frederick Tappert. Transmission of stationary nonlinear optical pulses in dispersive dielectric fibers. i. anomalous dispersion. *Appl. Phys. Lett.*, 23:142–144, 1973.
- [32] L. F. Mollenauer, R. H. Stolen, and J. P. Gordon. Experimental observation of picosecond pulse narrowing and solitons in optical fibers. *Phys. Rev. Lett.*, 45:1095–1098, 1980.
- [33] Barry Gross and Jamal T. Manassah. Supercontinuum in the anomalous group-velocity dispersion region. *JOSA B*, 9:1813–1818, 1992.
- [34] Sir Isaac Newton. *Opticks*. 1704.
- [35] René Descartes. *La Dioptrique*. 1637.
- [36] Robert Hooke. *Micrographia*. 1665.
- [37] Christiaan Huygens. *Traité de la lumière*. 1690.
- [38] Thomas Young. Experimental demonstration of the general law of the interference of light. In *Philosophical Transactions of the Royal Society of London*, volume 94, 1804.
- [39] Andrzej Wróblewski. de mora luminis: A spectacle in two acts with a prologue and an epilogue. *Am. J. Phys.*, 53 (7):620–630, 1985.
- [40] W. Heisenberg and H. Euler. Folgerungen aus der diracschen theorie des positrons. *Zeitschrift für Physik A: Hadrons and Nuclei*, 98:714–732, 1936.
- [41] Michael Mansfield and Colm O’Sullivan. *Understanding Physics*. Wiley, 1999.
- [42] John A. Wheeler Charles W. Misner, Kip S. Thorne. *Gravitation*. Freeman, 1973.
- [43] Chris Doran and Anthony Lasenby. *Geometric Algebra for Physicists*. Cambridge University Press, 2003.

- 
- [44] Stephen Gasiorowicz. *Quantum Physics, 3rd edition*. Wi, 2003.
- [45] A. Sommerfeld and G. Wentzel.  $\tilde{\text{A}}\text{I}\tilde{\text{J}}$ ber regul $\tilde{\text{A}}\text{r}$ e und irregul $\tilde{\text{A}}\text{r}$ e dubletts. *Zeitschrift f $\tilde{\text{A}}\text{i}\tilde{\text{J}}$ r Physik A: Hadrons and Nuclei*, 7:86–92, 1921.
- [46] W. Heisenberg. Zur quantentheorie der linienstruktur und der anomalen zeemaneffekte. *Zeitschrift f $\tilde{\text{A}}\text{i}\tilde{\text{J}}$ r*, 8:273–297, 1922.
- [47] N. Bohr.  $\tilde{\text{A}}\text{I}\tilde{\text{J}}$ ber die anwendung der quantentheorie auf den atombau i. die grundpostulate der quantentheorie. *Zeitschrift f $\tilde{\text{A}}\text{i}\tilde{\text{J}}$ r Physik A: Hadrons and Nuclei*, 13:117–165, 1923.
- [48] L. de Broglie. *Recherches sur la th $\tilde{\text{A}}\text{l}$ orie des quanta*. PhD thesis, Sorbonne University, 1924.
- [49] M. Born and P. Jordan. Zur quantenmechanik. *Zeitschrift f $\tilde{\text{A}}\text{i}\tilde{\text{J}}$ r Physik A: Hadrons and Nuclei*, 34:858–888, 1925.
- [50] P. A. M. Dirac. The fundamental equations of quantum mechanics. *Proc. R. Soc. Lond. A*, 109:642–653, 1925.
- [51] E. Schrödinger. Quantisierung als eigenwertproblem. *Annalen der Physik*, 385:437–490, 1926.
- [52] Wolfgang Pauli.  $\tilde{\text{A}}\text{I}\tilde{\text{J}}$ ber das wasserstoffspektrum vom standpunkt der neuen quantenmechanik. *Zeitschrift f $\tilde{\text{A}}\text{i}\tilde{\text{J}}$ r Physik A: Hadrons and Nuclei*, 36:336–363, 1926.
- [53] John A. Buck. *Fundamentals of Optical Fibers*. Wiley, 2004.
- [54] Govind P. Agrawal. *Fiber-Optic Communication Systems, fourth edition*. Wiley, 2010.
- [55] Govind P. Agrawal. *Nonlinear Fiber Optics, third edition*. Academic Press, 2001.
- [56] Luther Pfahler Eisenhart. Separable systems of st $\tilde{\text{A}}\text{c}$ kel. *Annals of Mathematics*, 35:284–305, 1934.
- [57] Nail Akhmediev and Adrian Ankiewicz. *Solitons, Nonlinear Pulses and Beams*. Chapman & Hall, 1997.

- 
- [58] Lin Zhang, Qiang Lin, Yang Yue, Yan Yan, Raymond G. Beausoleil, and Alan E. Willner. Silicon waveguide with four zero-dispersion wavelengths and its application in on-chip octave-spanning supercontinuum generation. *Optics Express*, 20:1685–1690, 2012.
- [59] W. H. Reeves, J. C. Knight, P. S. J. Russell, and P. J. Roberts. Demonstration of ultra-flattened dispersion in photonic crystal fibers. *Optics Express*, 10:609–613, 2002.
- [60] L. G. Cohen, C. Lin, and W. G. French. Tailoring zero chromatic dispersion into the 1.5 - 1.6  $\mu\text{m}$  low-loss spectral region of single-mode fibers. *Electron. Lett.*, 15:334–335, 1979.
- [61] C. T. Chang. Minimum dispersion at 1.55  $\mu\text{m}$  for single-mode step-index fibres. *Electron. Lett.*, 15:765–767, 1979.
- [62] C. T. Chang. Minimum dispersion in a single-mode step-index optical fiber. *Applied Optics*, 18:2516–1522, 1979.
- [63] I. P. Kaminow. Polarization in optical fibers. *IEEE J. Quantum Electron.*, QE-17:15–22, 1981.
- [64] G. J. Foschini and C. D. Poole. Statistical theory of polarization dispersion in single mode fibers. *Journal of Lightwave Technology*, 9:1439–1456, 1991.
- [65] C. R. Menyuk. Application of multiple length-scale methods to the study of optical fiber transmission. *Journal of Engineering Mathematics*, 36:113–136, 1999.
- [66] N. Kalyanasundaram and P. Muthuchidambaranathan. Nonlinear pulse propagation in a weakly birefringent optical fiber part 1: Derivation of coupled nonlinear schrodinger equations (cnlse). *Progress In Electromagnetics Research B*, 19:205–231, 2010.
- [67] E. Lichtman. Performance limitations imposed on all-optical ultralong lightwave systems at the zero-dispersion wavelength. *Journal of Lightwave Technology*, 13:898–905, 1995.
- [68] Ezra Ip and Joseph M. Kahn. Digital equalization of chromatic dispersion and polarization mode dispersion. *Journal of Lightwave Technology*, 25:2033–2043, 2007.

- 
- [69] M. González-Herráez, S. Martín-López, P. Corredera, M. L. Hernanz, and P. R. Horche. Supercontinuum generation using a continuous-wave raman fiber laser. *Optics Communications*, 226:323–328, 2003.
- [70] V. Ramaswamy and W. G. French. Influence of noncircular core on the polarisation performance of single mode fibres. *Electron. Lett.*, 14:143–144, 1978.
- [71] S. C. Rashleigh. Origins and control of polarization effects in single-mode fibers. *Journal of Li*, 1:312–331, 1983.
- [72] M. Lehtonen, G. Genty, H. Ludvigsen, and M. Kaivola. Supercontinuum generation in a highly birefringent microstructured fiber. *Appl. Phys. Lett.*, 82:2197–2199, 2003.
- [73] Antoine Proulx, Jean-Michel Ménard, Nicolas Hô, Jacques M. Laniel, and Réal Vallée. Intensity and polarization dependences of the supercontinuum generation in birefringent and highly nonlinear microstructured fibers. *Optics Express*, 11:3338–3345, 2003.
- [74] Joel A. Greenberg and Daniel J. Gauthier. High-order optical nonlinearity at low light levels. *Europhysics Letters*, 98:24001, 2012.
- [75] Michael Hofmann, Janne Hytti, Simon Birkholz, Martin Bock, Susanta K. Das, Rüdiger Grunwald, Mathias Hoffmann, Tamas Nagy, Ayhan Demircan, Marco Jupé, Detlev Ristau, Uwe Morgner, Carsten Brée, Michael Woerner, Thomas Elsaesser, and GÃijnter Steinmeyer. Noninstantaneous polarization dynamics in dielectric media. *Optica*, 2:151–157, 2015.
- [76] R. W. Terhune, P. D. Maker, and C. M. Savage. Optical harmonic generation in calcite. *Physical Review Letters*, 8:404–406, 1962.
- [77] Anatoly Efimov, Antoinette Taylor, Fiorenzo Omenetto, Jonathan Knight, William Wadsworth, and Philip Russell. Phase-matched third harmonic generation in microstructured fibers. *Optics Express*, 11:2567–2576, 2003.
- [78] K. J. Blow and D. Wood. Theoretical description of transient stimulated raman scattering in optical fibers. *IEEE J. Quantum Electron.*, 25:2665–2673, 1989.

- 
- [79] David Milam. Review and assessment of measured values of the nonlinear refractive-index coefficient of fused silica. *Applied Optics*, 37:546–550, 1998.
- [80] J. M. Dudley and S. Coen. Coherence properties of supercontinuum spectra generated in photonic crystal and tapered optical fibers. *Optics Letters*, 27:1180–1182, 2002.
- [81] C. V. Shank, R. L. Fork, R. Yen, R. H. Stolen, and W. J. Tomlinson. Compression of femtosecond optical pulses. *Appl. Phys. Lett.*, 40:761–763, 1982.
- [82] W. H. Knox, R. L. Fork, M. C. Downer, R. H. Stolen, C. V. Shank, , and J. A. Valdmanis. Optical pulse compression to 8 fs at a 5-khz repetition rate. *Appl. Phys. Lett.*, 46:1120–1121, 1985.
- [83] Akhelesh K. Abeeluck and Clifford Headley. Continuous-wave pumping in the anomalous- and normal-dispersion regimes of nonlinear fibers for supercontinuum generation. *Optics Letters*, 30:61–63, 2005.
- [84] Ben Howard Chapman, Sergei V. Popov, and Roy Taylor. Continuous wave supercontinuum generation through pumping in the normal dispersion region for spectral flatness. *IEEE Photonics Technology Letters*, 24:1325–1327, 2012.
- [85] J. M. Dudley and J. R. Taylor. *Supercontinuum Generation in Optical Fibers*. Cambridge University Press, 2010.
- [86] J. Hansryd, P.A. Andrekson, M. Westlund, L. Jie, and P. Hedekvist. Fiber-based optical parametric amplifiers and their applications. *IEEE Sel. Topics Quantum Electron.*, 8:506–520, 2002.
- [87] F. Forghieri, R. W. Tkach, and A. R. Chraplyvy. *Optical Fiber Telecommunications, Vol 3A*. Academic Press, 1997.
- [88] C. V. Raman. A new radiation. *Indian J. Phys.*, 2:387–398, 1928.
- [89] R. W. Hellwarth. Theory of stimulated raman scattering. *Phys. Rev. Lett.*, 130:1850–1852, 1963.
- [90] Thomas Brabec and Ferenc Krausz. Nonlinear optical pulse propagation in the single-cycle regime. *Physical Review Letters*, 78:3282, 1997.

- 
- [91] R. H. Stolen, J. P. Gordon, W. J. Tomlinson, and H. A. Haus. Raman response function of silica-core fibers. *JOSA B*, 6:1159–1166, 1989.
- [92] Miro Erkintalo, Goëry Genty, Benjamin Wetzel, and John M. Dudley. Limitations of the linear raman gain approximation in modeling broadband nonlinear propagation in optical fibers. *Optics Express*, 18:25449–25460, 2010.
- [93] G. H. Weiss and A. A. Maradudin. The baker-hausdorff formula and a problem in crystal physics. *J. Math. Phys.*, 3:771–777, 1962.
- [94] Matteo Frigo and Steven G. Johnson. *The Fastest Fourier Transform in the West*.
- [95] V. E. Zakharov and A. B. Shabat. Exact theory of two-dimensional self-focusing and one-dimensional self-modulation of waves in nonlinear media. *Soviet Physics JETP*, 34:62–69, 1972.
- [96] Ryogo Hirota and Junkichi Satsuma. A variety of nonlinear network equations generated from the bÄcklund transformation for the toda lattice. *Progress of Theoretical Physics Supplements*, 59:64–100, 1976.
- [97] John Weiss, M. Tabor, and George Carnevale. The painlevÄ property for partial differential equations. *J. Math. Phys.*, 24:522–526, 1983.
- [98] W. Malfliet. Solitary wave solutions of nonlinear wave equations. *American Journal of Physics*, 60:650–654, 1992.
- [99] Zhenya Yan. Generalized method and its application in the higher-order nonlinear schrodinger equation in nonlinear optical fibres. *Chaos, Solitons & Fractals*, 16:759–766, 2003.
- [100] Curtis Menyuk. Soliton robustness in optical fibers. *Journal of the Optical Society of America B*, 10:1585–1591, 1993.
- [101] E. A. Kuznetsov. Solitons in a parametrically unstable plasma. *Soviet Physics Doklady*, 22:507–508, 1977.
- [102] N. Akhmediev and V. I. Korneev. Modulation instability and periodic solutions of the nonlinear schrÄdinger equation. *Theor. Math. Phys.*, 69:1089–1093, 1986.

- 
- [103] D. H. Peregrine. Water waves, nonlinear schrödinger equations and their solutions. *The Journal of the Australian Mathematical Society. Series B. Applied Mathematics*, 25:16–43, 1983.
- [104] D. Krökel, N. J. Halas, G. Giuliani, and D. Grischkowsky. Dark-pulse propagation in optical fibers. *Physical Review Letters*, 60:29, 1988.
- [105] J. M. Dudley, G. Genty, F. Dias, B. Kibler, and N. Akhmediev. Modulation instability, akhmediev breathers and continuous wave supercontinuum generation. *Optics Express*, 17:21497–21508, 2009.
- [106] B. Kibler, J. Fatome, C. Finot, G. Millot, F. Dias, G. Genty, N. Akhmediev, and J. M. Dudley. The peregrine soliton in nonlinear fibre optics. *Nature Physics*, 6:790–795, 2010.
- [107] B. Kibler, J. Fatome, C. Finot, G. Millot, G. Genty, B. Wetzel, N. Akhmediev, F. Dias, and J. M. Dudley. Observation of kuznetsovma soliton dynamics in optical fibre. *Scientific Reports*, 2:463, 2012.
- [108] John Scott Russell. Report on waves. Report of the 14th Meeting of the British Association for Advancement of Science, York, September, 1844.
- [109] A. Chabchoub, N. P. Hoffmann, and N. Akhmediev. Rogue wave observation in a water wave tank. *Physical Review Letters*, 106:204502, 2011.
- [110] Akira Hasegawa and Yuji Kodama. Signal transmission by optical solitons in monomode fiber. *Proceedings of the IEEE*, 69:1145–1150, 1981.
- [111] Nail Akhmediev and Magnus Karlsson. Cherenkov radiation emitted by solitons in optical fibers. *Physical Review A*, 51:2602, 1995.
- [112] R. J. Mears, L. Reekie, S. B. Poole, and D. N. Payne. Low-threshold tunable cw and q-switched fibre laser operating at 1.55  $\mu\text{m}$ . *Electronics Letters*, 22:159–160, 1986.
- [113] E. Desurvire, J. R. Simpson, and P. C. Becker. High-gain erbium-doped traveling-wave fiber amplifier. *Optics Letters*, 12:888–890, 1987.

- 
- [114] M. Nakazawa, K. Kurokawa, H. Kubota, K. Suzuki, and Y. Kimura. Femtosecond erbium-doped optical fiber amplifier. *Applied Physics Letters*, 57:653, 1990.
- [115] M. Nakazawa, Y. Kimura, and K. Suzuki. Ultralong dispersion-shifted erbium-doped fiber amplifier and its application to soliton transmission. *IEEE Journal of Quantum Electronics*, 26:2103–2108, 1990.
- [116] G. P. Agrawal. Amplification of ultrashort solitons in erbium-doped fiber amplifiers. *IEEE Photonics Technology Letters*, 2:875–877, 1990.
- [117] I. V. MelâĖnikov, R. F. Nabiev, and A. V. Nazarkin. Coherent amplification of ultrashort solitons in doped fibers. *Optics L*, 15:1348–1350, 1990.
- [118] G. P. Agrawal. Effect of gain dispersion and stimulated raman scattering on soliton amplification in fiber amplifiers. *Optics Letters*, 16:226–228, 1991.
- [119] G. P. Agrawal. Optical pulse propagation in doped fiber amplifiers. *Physical Review A*, 44:7493–7501, 1991.
- [120] A. Antikainen, M. Erkintalo, G. Genty, and J. M. Dudley. On the phase-dependent manifestation of optical rogue waves. *Nonlinearity*, 25:R73–R83, 2012.
- [121] R. Driben and I. Babushkin. Accelerated rogue waves generated by soliton fusion at the advanced stage of supercontinuum formation in photonic-crystal fibers. *Optics Letters*, 37:5157–5159, 2012.
- [122] J. M. Dudley, F. Dias, M. Erkintalo, and G. Genty. Instabilities, breathers and rogue waves in optics. *Nature Photonics*, 8:755–764, 2014.
- [123] R. Driben, B. A. Malomed, A. V. Yulin, and D. V. Skryabin. NewtonâĖs cradles in optics: from n-soliton fission to soliton chains. *Physical Review A*, 87:063808, 2013.
- [124] R. Driben, A. V. Yulin, A. Efimov, and B. A. Malomed. Trapping of light in solitonic cavities and its role in the supercontinuum generation. *Optics E*, 21:19091–19096, 2013.

- [125] Andrey V. Gorbach and Dmitry V. Skryabin. Theory of radiation trapping by the accelerating solitons in optical fibers. *Phys. Rev. A*, 76:053803, 2007.
- [126] B. W. Plansinis, W. R. Donaldson, and G. P. Agrawal. What is the temporal analog of reflection and refraction of optical beams? *Physical Review Letters*, 115:183901, 2015.
- [127] P. Cimalla, J. Walther, M. Mehner, M. Cuevas, and E. Koch. Simultaneous dual-band optical coherence tomography in the spectral domain for high resolution in vivo imaging. *Optics Express*, 17:19486–19500, 2009.
- [128] E. Lareau, F. Lesage, P. Pouliot, D. Nguyen, J. Le Lan, and M. Sawan. Multichannel wearable system dedicated for simultaneous electroencephalography/near-infrared spectroscopy real-time data acquisitions. *Journal of Biomedical Optics*, 16:096014, 2011.
- [129] Q. Cao, N. G. Zhegalova, S. T. Wang, W. J. Akers, and M. Y. Berezin. Multispectral imaging in the extended near-infrared window based on endogenous chromophores. *Journal of Biomedical Optics*, 18:101318, 2013.
- [130] R. H. Stolen, C. Lee, and R. K. Jain. Development of the stimulated raman spectrum in single-mode silica fibers. *Journal of the Optical Society of America B*, 1:652–657, 1984.
- [131] P. L. Baldeck and R. R. Alfano. Intensity effects on the stimulated four photon spectra generated by picosecond pulses in optical fibers. *Journal of Lightwave Technology*, LT-5:1712–1715, 1987.
- [132] I. Ilev, H. Kumagai, K. Toyoda, and I. Koprinkov. Highly efficient wide-band continuum generation in a single-mode optical fiber by powerful broadband laser pumping. *Applied Optics*, 35:2548–2553, 1996.
- [133] P. Beaud, W. Hodel, B. Zysset, and H. P. Weber. Ultrashort pulse propagation, pulse breakup, and fundamental soliton formation in a single-mode optical fiber. *IEEE Journal of Quantum Electronics*, QE-23:1938–1946, 1987.

- 
- [134] A. S. Gouveia-Neto, M. E. Faldon, and J. R. Taylor. Solitons in the region of the minimum group-velocity dispersion of single-mode optical fibers. *Optics Letters*, 13:770–772, 1988.
- [135] J. Schütz, W. Hodel, and H. P. Weber. Nonlinear pulse distortion at the zero dispersion wavelength of an optical fibre. *Optics Communications*, 95:357–365, 1993.
- [136] Y. Kodama and A. Hasegawa. Nonlinear pulse propagation in a monomode dielectric guide. *IEEE Journal of Quantum Electronics*, QE-23:510–524, 1987.
- [137] M. N. Islam, G. Sucha, I. Bar-Joseph, M. Wegener, J. P. Gordon, and D. S. Chemla. Broad bandwidths from frequency-shifting solitons in fibers. *Optics Letters*, 14:370–372, 1989.
- [138] M. N. Islam, G. Sucha, I. Bar-Joseph, M. Wegener, J. P. Gordon, and D. S. Chemla. Femtosecond distributed soliton spectrum in fibers. *Journal of the Optical Society of America B*, 6:1149–1158, 1989.
- [139] K. Mori, T. Morioka, and M. Saruwatari. Group-velocity dispersion measurement using supercontinuum picosecond pulses generated in an optical-fiber. *Electronics Letters*, 29:987–989, 1993.
- [140] H. Takara, S. Kawanishi, T. Morioka, K. Mori, and M. Saruwatari. 100gbit/s optical wave-form measurement with 0.6ps resolution optical-sampling using subpicosecond supercontinuum pulses. *Electronics*, 30:1152–1153, 1994.
- [141] M. N. Islam, C. D. Poole, and J. P. Gordon. Soliton trapping in birefringent optical fibers. *Optics Letters*, 14:1011–1013, 1989.
- [142] D. V. Skryabin and A. V. Yulin. Theory of generation of new frequencies by mixing of solitons and dispersive waves in optical fibers. *Phys. Rev. E*, 72:016619, 2005.
- [143] A.V. Gorbach, D.V. Skryabin, J.M. Stone, and J.C. Knight. Four-wave mixing of solitons with radiation and quasi-nondispersive wave packets at the short-wavelength edge of a supercontinuum. *Optics Express*, 14:9854–9863, 2006.

- 
- [144] J. C. Travers and J. R. Taylor. Soliton trapping of dispersive waves in tapered optical fibers. *Optics Letters*, 34:115–117, 2009.
- [145] Edmund J. R. Kelleher, John C. Travers, Sergei V. Popov, and James R. Taylor. Role of pump coherence in the evolution of continuous-wave supercontinuum generation initiated by modulation instability. *Journal of the Optical Society of America B*, 29:502–512, 2012.
- [146] A. Hasegawa. Generation of a train of soliton pulses by induced modulational instability in optical fibers. *Optics Letters*, 9:288–290, 1984.
- [147] K. Liu, C. R. Ye, S. Khan, and V. J. Sorger. Review and perspective on ultrafast wavelength-size electro-optic modulators. *Laser & Photonics Reviews*, 9:172–194, 2015.
- [148] Wei Cao, David Hagan, David J. Thomson, Milos Nedeljkovic, Callum G. Littlejohns, Andy Knights, Shaif-Ul Alam, Junjia Wang, Frederic Gardes, Weiwei Zhang, Shenghao Liu, Ke Li, Mohamed Said Rouifed, Guo Xin, Wanjun Wang, Hong Wang, Graham T. Reed, , and Goran Z. Mashanovich. High-speed silicon modulators for the 2- $\mu\text{m}$  wavelength band. *Optica*, 5:1055–1062, 2018.
- [149] Govind P. Agrawal, P. L. Baldeck, and R. R. Alfano. Modulation instability induced by cross-phase modulation in optical fibers. *Physical Review A*, 39:3406, 1989.
- [150] S. Trillo, S. Wabnitz, and T. A. B. Kennedy. Nonlinear dynamics of dual-frequency-pumped multiwave mixing in optical fibers. *Physical Review A*, 50:1732, 1994.
- [151] Chunle Xiong, Zilun Chen, and William J. Wadsworth. Dual-wavelength-pumped supercontinuum generation in an all-fiber device. *Journal of Lightwave*, 27:1638–1643, 2009.
- [152] S. A. Diddams, D. J. Jones, J. Ye, S. T. Cundiff, J. L. Hall, J. K. Ranka, R. S. Windeler, R. Holzwarth, T. Udem, and T. W. Hänsch. Direct link between microwave and optical frequencies with a 300 thz femtosecond laser comb. *Physical Review Letters*, 84:5102–5105, 2000.

- [153] T. Udem, R. Holzwarth, and T. W. Hänsch. Optical frequency metrology. *Nature*, 416:233–237, 2002.
- [154] B. Bernhardt, A. Ozawa, P. Jacquet, M. Jacquy, Y. Kobayashi, T. Udem, R. Holzwarth, G. Guelachvili, T. W. Hänsch, and N. Picqué. Cavity-enhanced dual-comb spectroscopy. *Nature Photonics*, 4:55–57, 2010.
- [155] J. Pfeifle, V. Brasch, M. Lauermaun, Y. Yu, D. Wegner, T. Herr, K. Hartinger, P. Schindler, J. Li, D. Hillerkuss, R. Schmogrow, C. Weimann, R. Holzwarth, W. Freude, J. Leuthold, T. J. Kippenberg, and C. Koos. Coherent terabit communications with microresonator kerr frequency combs. *Nature Photonics*, 8:375–380, 2014.
- [156] C.-B. Huang, Z. Jiang, D. E. Leaird, and A. M. Weiner. High-rate femtosecond pulse generation via line-by-line processing of phase-modulated cw laser frequency comb. *Electronics*, 42:1114–1115, 2006.
- [157] S. V. Chernikov, E. M. Dianov, D. J. Richardson, R. I. Laming, and D. N. Payne. 114 gbit/s soliton train generation through raman self-scattering of a dual frequency beat-signal in dispersion decreasing optical fibre. *Applied Physics Letters*, 63:293–295, 1993.
- [158] M. Nakazawa, K. Suzuki, and H. Haus. Modulation instability oscillation in nonlinear dispersive ring cavity. *Physical Review A*, 38:5193–5196, 1988.
- [159] S. Coen and M. Haeltermann. Continuous-wave ultrahigh-repetition-rate pulse-train generation through modulational instability in a passive fiber cavity. *Optics Letters*, 26:39–41, 2001.
- [160] A. Zadok, J. Sendowski, and A. Yariv. Birefringence-induced trains of high-rate pulses in a mode-locked fiber laser. *IEEE Photonics Journal*, 1:128–134, 2009.
- [161] Y. Okawachi, K. Saha, J. S. Levy, Y. Henry Wen, M. Lipson, and A. L. Gaeta. Octave-spanning frequency comb generation in a silicon nitride chip. *Optics Letters*, 36:3398–3400, 2011.

- 
- [162] A. R. Johnson, Y. Okawachi, J. S. Levy, J. Cardenas, K. Saha, M. Lipson, and A. L. Gaeta. Chip-based frequency combs with sub-100 ghz repetition rates. *Optics Letters*, 37:875–877, 2012.
- [163] A. M. Weiner, D. E. Leaird, G. P. Wiederrecht, and K. A. Nelson. Femtosecond pulse sequences used for optical manipulation of molecular motion. *Science*, 247:1317–1319, 1990.
- [164] D. Umstadter, E. Esarey, and J. Kim. Nonlinear plasma waves resonantly driven by optimized laser pulse trains. *Physical Review Letters*, 72:1224–1227, 1994.
- [165] Y. Liu, S.-G. Park, and A. M. Weiner. Enhancement of narrow-band terahertz radiation from photoconducting antennas by optical pulse shaping. *Optics Letters*, 21:1762–1764, 1996.
- [166] J. Fatome, S. Pitois, C. Fortier, B. Kibler, C. Finot, G. Millot, C. Courde, M. Lintz, and E. Samain. Multiple four-wave mixing in optical fibers: 1.5–3.4-thz femtosecond pulse sources and real-time monitoring of a 20-ghz picosecond source. *Optics Communications*, 283:2425–2429, 2010.
- [167] W. J. Tomlinson, R. H. Stolen, and A. M. Johnson. Optical wave breaking of pulses in nonlinear optical fibers. *Optics Letters*, 10:457–459, 1985.
- [168] H. Sotobayashi and K. Kitayama. 325 nm bandwidth supercontinuum generation at 10 gbit/s using dispersion-flattened and non-decreasing normal dispersion fibre with pulse compression technique. *Electronics Letters*, 34:1336–1337, 2006.
- [169] A. Hartung, A. M. Heidt, and H. Bartelt. Design of all-normal dispersion microstructured optical fibers for pulse-preserving supercontinuum generation. *Optics Express*, 19:7742–7749, 2011.
- [170] J. Fatome, C. Finot, G. Millot, A. Armaroli, and S. Trillo. Observation of optical undular bores in multiple four-wave mixing. *Physical Review X*, 4:021022, 2014.

- 
- [171] P.-A. Champert, V. Couderc, P. Leproux, S. Février, V. Tombelaine, L. Labonté, P. Roy, C. Froehly, and P. Nérin. White-light supercontinuum generation in normally dispersive optical fiber using original multi-wavelength pumping system. *Optics Express*, 12:4366–4371, 2004.
- [172] C. Finot, B. Kibler, L. Provost, and S. Wabnitz. Beneficial impact of wave-breaking for coherent continuum formation in normally dispersive nonlinear fibers. *Journal of the Optical Society of America B*, 25:1938–1948, 2008.
- [173] A. Kudlinski, A. K. George, J. C. Knight, J. C. Travers, A. B. Rulko, S. V. Popov, and J. R. Taylor. Zero-dispersion wavelength decreasing photonic crystal fibers for ultraviolet-extended supercontinuum generation. *Optics Express*, 14:5715–5722, 2006.
- [174] S. P. Stark, A. Podlipensky, N. Y. Joly, and P. S. J. Russell. Ultraviolet-enhanced supercontinuum generation in tapered photonic crystal fiber. *Journal of the Optical Society of America B*, 27:592–598, 2010.
- [175] D. Solli, C. Ropers, P. Koonath, and B. Jalali. Optical rogue waves. *Nature*, 450:1054–1057, 2007.
- [176] G. Genty and J. M. Dudley. Route to coherent supercontinuum generation in the long pulse regime. *IEEE Journal of Quantum Electronics*, 45:1331–1335, 2009.
- [177] T. Schreiber, T. V. Andersen, D. Schimpf, J. Limpert, and A. Tünnermann. Supercontinuum generation by femtosecond single and dual wavelength pumping in photonic crystal fibers with two zero dispersion wavelengths. *Optics Express*, 13:9556–9569, 2005.
- [178] E. Rääkkönen, G. Genty, O. Kimmelma, M. Kaivola, K. P. Hansen, and S. C. Buchter. Supercontinuum generation by nanosecond dual-wavelength pumping in microstructured optical fibers. *Optics Express*, 14:7914–7923, 2006.
- [179] Y. Wang, C. Xiong, J. Hou, J. Cao, Y. Li, R. Song, and Q. Lu. Continuous wave, dual-wavelength-pumped supercontinuum generation in an all-fiber device. *Applied Optics*, 50:2752–2758, 2011.

- 
- [180] N. Jia, H. T. Yan, and M. Li. Dual-pulse pump for enhancing supercontinuum generation. *IEEE Photonics Journal*, 8:7100207, 2016.
- [181] A. Demircan, S. Amiranashvili, C. Brée, and G. Steinmeyer. Compressible octave spanning supercontinuum generation by two-pulse collisions. *Physical Review Letters*, 110:233901, 2013.
- [182] A. Antikainen, F. R. Arteaga-Sierra, and G. P. Agrawal. Supercontinuum generation in photonic crystal fibers with longitudinally varying dispersion using dual-wavelength pumping. In *Frontiers in Optics 2016, OSA Technical Digest (online) (Optical Society of America, 2016)*, paper FTu1I.6, 2016.
- [183] A. Demircan, S. Amiranashvili, C. Brée, U. Morgner, and G. Steinmeyer. Supercontinuum generation by multiple scatterings at a group velocity horizon. *Optics Express*, 22:3866–3879, 2014.
- [184] Z. Deng, X. Fu, J. Liu, C. Zhao, and S. Wen. Trapping and controlling the dispersive wave within a solitonic well. *Optics Express*, 24:10302–10312, 2016.
- [185] K. Kurokawa, K. Nakajima, K. Tsujikawa, T. Yamamoto, and K. Tajima. Ultra-wideband transmission over low loss pcf. *Journal of Lightwave Technology*, 27:1653–1662, 2009.
- [186] M. A. Islam and M. S. Alam. Design optimization of equiangular spiral photonic crystal fiber for large negative flat dispersion and high birefringence. *Journal of Lightwave Technology*, 30:3545–3551, 2012.
- [187] P. V. Mamyshev, S. V. Chernikov, E. M. Dianov, and A. M. Prokhorov. Generation of a high-repetition-rate train of practically noninteracting solitons by using the induced modulational instability and raman self-scattering effects. *Optics Letters*, 15:1365–1367, 1990.
- [188] C. Mahnke and F. Mitschke. Possibility of an akhmediev breather decaying into solitons. *Physical Review A*, 85:033808, 2012.
- [189] D. J. Richardson, R. P. Chamberlain, L. Dong, and D. N. Payne. High quality soliton loss-compensation in 38 km dispersion-decreasing fibre. *Electronics Letters*, 31:1681–1682, 1995.

- 
- [190] M. Karlsson and A. Höök. Soliton-like pulses governed by fourth order dispersion in optical fibers. *Optics*, 104:303–307, 1994.
- [191] D. V. Skryabin, F. Luan, J. C. Knight, and P. S. J. Russell. Soliton self-frequency shift cancellation in photonic crystal fibers. *Science*, 301:1705–1708, 2003.